

STOICHIOMETRY CONTROL MECHANISMS OF BIAS SPUTTERED
ZINC OXIDE FILMS

by

MICHAEL JULIAN BRETT

B.Sc., Queen's University, 1979
M.Sc., University of British Columbia, 1981

A THESIS SUBMITTED IN PARTIAL FULFILMENT OF
THE REQUIREMENTS FOR THE DEGREE OF
DOCTOR OF PHILOSOPHY

in

THE FACULTY OF GRADUATE STUDIES

Physics Department

We accept this thesis as conforming
to the required standard

THE UNIVERSITY OF BRITISH COLUMBIA

June 1985

© Michael Julian Brett, 1985

22

In presenting this thesis in partial fulfilment of the requirements for an advanced degree at the University of British Columbia, I agree that the Library shall make it freely available for reference and study. I further agree that permission for extensive copying of this thesis for scholarly purposes may be granted by the head of my department or by his or her representatives. It is understood that copying or publication of this thesis for financial gain shall not be allowed without my written permission.

Department of Physics

The University of British Columbia
1956 Main Mall
Vancouver, Canada
V6T 1Y3

Date June 20, 1985

ABSTRACT

This thesis reports the first detailed study of the stoichiometry control mechanisms and physical properties of ZnO films deposited by dc planar magnetron sputtering of a Zn target in a reactive Ar/O₂ atmosphere. Control of film stoichiometry was achieved using a subsidiary rf discharge at the substrate and a reactive gas baffle surrounding the target. The reactive gas baffle was shown to enhance film oxidation by decreasing the metal flux to the substrate and increasing the oxygen partial pressure near the substrate. Rutherford backscattering analysis of film stoichiometry demonstrated that the effect of the rf discharge was to increase the O/Zn composition ratio. This oxidation was shown to occur through preferential resputtering and preferential evaporation of excess Zn and by activation and ion plating of oxygen species. Resputtering and evaporation rates were found to be enhanced above that expected for bulk Zn, due to the weak bonding of surface adatoms during film growth.

Conducting ZnO films produced at various values of the rf-induced substrate bias voltage were characterized for electrical, optical and structural properties using Hall probe, X-ray diffraction, electron microscope, and visible and infrared spectroscopy techniques. Films deposited at low substrate bias (0 to -50V) were found to have a large Zn excess (15%) resulting in low electron mobilities (1 cm²/Vs), high resistivities (10⁻² Ωcm) and were strongly absorbing in the visible. Films deposited at high substrate bias were

nearly stoichiometric, optically transparent and had high electron mobilities ($15 \text{ cm}^2/\text{Vs}$) resulting in low resistivity ($10^{-3} \text{ } \Omega\text{cm}$). The optical properties of transparent conducting films for wavelengths 0.4 to $20 \text{ } \mu\text{m}$ were modelled by the Drude theory of free electrons using measured electrical transport properties.

The original goal of this work, to develop a heat mirror coating suitable for manufacture, was achieved by bias sputter deposition of ZnO onto uncooled polyester sheet at deposition rates approaching 75 nm/min . The best heat mirror films had a transmission to solar energy of 75% and an 85% reflection of 300 K blackbody radiation.

TABLE OF CONTENTS

	<u>Page</u>
ABSTRACT	ii
TABLE OF CONTENTS	iv
LIST OF TABLES	vi
LIST OF FIGURES	vii
ACKNOWLEDGEMENTS	ix
CHAPTER 1 - INTRODUCTION	
1.1 Motivation for This Work	1
1.2 Heat Mirrors	2
1.3 Drude Theory of Free Electrons	5
1.4 Choice of ZnO	8
1.5 Properties of ZnO	11
1.6 Deposition Processes	13
CHAPTER 2 - HEAT MIRROR DEPOSITION	
2.1 Apparatus and Experimental Method	18
2.2 Operating Characteristics	24
2.3 ZnO Heat Mirrors	30
2.4 ITO Heat Mirrors	34
2.5 Summary	36
CHAPTER 3 - THE REACTIVE GAS BAFFLE	
	37

CHAPTER 4 - THE SUBSTRATE RF DISCHARGE

4.1 Properties of an rf Glow Discharge	42
4.2 Effects of an rf Discharge	47
4.3 Film Stoichiometry	50
4.4 Material Re-emission	54
4.5 Zinc Re-emission by Evaporation	57
4.6 Zinc Re-emission by Sputtering	64
4.7 Oxygen Activation and Plating	68
4.8 Summary and Discussion	72

CHAPTER 5 - ZnO FILM CHARACTERIZATION

5.1 Film Degradation	77
5.2 Film Structure	80
5.3 Electrical Properties	91
5.4 Optical Properties	95

CHAPTER 6 - SUMMARY112

CHAPTER 7 - APPENDIX

7.1 Optical Constants of Transparent Films	115
7.2 Optical Constants of Absorbing Films	117

REFERENCES120

LIST OF TABLES

<u>Table</u>	<u>Page</u>
1.1 Typical properties of oxide heat mirrors	9
4.1 Mass measurement of bias sputtered Zn films ...	57
4.2 Comparison of re-emission rate from ZnO with bulk Zn evaporation rate	63
4.3 Resputter of ZnO films after deposition	67
4.4 Resputter yields of Zn and ZnO films	68
4.5 Thicknesses of bias sputtered TiO ₂ films	75
5.1 Grain size of bias sputtered ZnO films	86
5.2 Electrical properties of bias sputtered ZnO films	92
5.3 Electrical properties of ZnO films produced by other workers	92

LIST OF FIGURES

<u>Figure</u>		<u>Page</u>
1.1	Reflectivity of a free electron plasma	7
1.2	ZnO energy level diagram	12
2.1	Schematic of sputtering chamber	19
2.2	The reactive gas baffle	20
2.3	Substrate holder for plastic sheet	22
2.4	Variations of cathode voltage and $pp(O_2)$ with $f(O_2)$	26
2.5	Cathode current/voltage characteristic	28
2.6	Resistivity and ir reflectivity for bias sputtered ZnO	31
2.7	Heat mirror characteristics of ZnO films	32
2.8	Heat mirror characteristics of ITO films	35
3.1	$pp(O_2)$ enhancement by the reactive gas baffle .	38
3.2	Substrate and target discharge interaction	40
4.1	Energy distribution of ions at the substrate ..	46
4.2	Rutherford Backscatter spectrum for ZnO	51
4.3	Stoichiometry of bias sputtered ZnO	53
4.4	Variation of material re-emission with substrate bias and $f(O_2)$	55
4.5	Substrate temperature and rf power measurement .	59
4.6	Material re-emission from ZnO by evaporation ..	62
4.7	Material re-emission from Zn by sputtering	65
4.8	Material re-emission from ZnO by sputtering ...	66

4.9	Effects of oxygen activation	70
5.1	Degradation of resistivity for heated ZnO	78
5.2	Degradation of ir reflectivity for heated ZnO .	79
5.3	X-ray diffraction spectra for films deposited at various $f(O_2)$	82
5.4	X-ray diffraction spectra for bias sputtered Zn.	84
5.5	X-ray diffraction spectra for bias sputtered ZnO	85
5.6	Effects of annealing of ZnO	88
5.7	Scanning electron photomicrograph of columnar structure in ZnO	89
5.8	Scanning electron photomicrograph showing the effect of bias on surface roughness	90
5.9	Geometry of films for Hall probe measurements .	92
5.10	Depiction of Manifacier's technique for deducing optical constants	98
5.11	Optical constants of bias sputtered ZnO films .	99
5.12	Ir reflectivity of bias sputtered ZnO films ...	101
5.13	Drude prediction of ir reflectivity for ZnO-5 .	103
5.14	Drude prediction of optical constants for ZnO-5.	104
5.15	Drude prediction of optical constants and ir reflectivity for ZnO-1	106
5.16	Transmission electron photomicrographs of bias sputtered ZnO	108
5.17	Maxwell-Garnett prediction of ir reflectvity for ZnO-1	111
7.1	Cross section of ZnO on quartz structure	116

ACKNOWLEDGEMENTS

I am especially grateful to my supervisor, Dr. R. Parsons, for the support, advice and assistance that he has provided throughout my years of study as a graduate student.

I feel fortunate to have had a rich and rewarding association with many other people in the semiconductor lab, and would like to extend thanks to John Affinito, Normand Fortier, Richard McMahon, Brian Sullivan, Juan Rostworowski, and Kevin Betts for their friendship and assistance.

I greatly appreciate the financial assistance that was provided by the Natural Sciences and Engineering Research Council, and by the University of British Columbia.

CHAPTER ONE: INTRODUCTION

1.1 MOTIVATION FOR THIS WORK

Radiative heat lost through single or double glazed windows in Canadian homes during the winter season may constitute up to 50% of the total heat loss in the building [1]. However, the thermal resistance or 'R-value' of a window may be dramatically improved by the application of a heat mirror coating to the inner glazing surfaces. Such a heat mirror, ideal for cold climates, is a thin film material that is transparent to solar energy (0.30 to 2.0 μm wavelength) but reflects room temperature blackbody radiation (5 to 40 μm wavelength). My thesis work was initially motivated by a desire to develop a heat mirror material and a corresponding high rate thin film deposition technique suitable for large scale manufacturing.

These goals were fulfilled by the successful production of a new heat mirror coating, ZnO, by bias sputtering onto plastic sheet at a deposition rate of 75 nm/min. In order to obtain a deeper understanding of the deposition process, research was then expanded to identify and analyze the mechanisms through which the bias sputter technique enabled control of the oxidation of sputtered zinc and subsequent optimization of heat mirror films. To complete this study, the electrical, optical and structural properties of films were fully characterized in relation to film stoichiometry and the deposition process.

Organization of this thesis follows the chronological order of research. A review of heat mirror technologies is provided in Chapter 1, along with reasons for the choice of film material and deposition process. The apparatus and techniques used to produce ZnO heat mirrors, and a preliminary evaluation of these heat mirrors, are described in Chapter 2. Chapters 3 and 4 are devoted to an in-depth study of the bias sputter process and Chapter 5 reports a full characterization of ZnO films of varied degrees of oxidation.

1.2 HEAT MIRRORS

Two general classes of heat mirror are presently recognized; heterostructure thin film stacks and single layer semiconductor coatings. A heterostructure heat mirror is a metal film sandwiched between dielectric coatings. A very thin (10 to 20 nm) metal film, such as gold or silver, provides infrared reflectivity and is partly transparent in the visible. This transparency is enhanced by antireflection coatings of a transparent and protective dielectric such as TiO_2 . A wide variety of metals and dielectrics have been used in heterostructure fabrication and include 18nm TiO_2 /18nm Ag/18nm TiO_2 [2], 45nm Bi_2O_3 /13nm Au/45nm Bi_2O_3 [3], and 15nm ZnO/14nm Ag/15nm ZnO [4]. Some of these films were originally developed as energy saving incandescent light bulb coatings. The Southwall Corporation [10] has already overcome the severe technological difficulties of thickness and composition control for heterostructure coatings manufactured in large

quantities on rolls of plastic sheet.

Typical optical characteristics for heterostructures are a maximum transmission of 85% at wavelength 500 nm and a reflection exceeding 80% for wavelengths greater than 3 μm . By increasing the metallic layer thickness, heterostructures may be configured as 'cooling load' heat mirrors for hot climates. Lower transmission of solar energy and reflection of atmospheric blackbody radiation would reduce the air-conditioning load of a large office building. Lampert [5] gives a review of the deposition techniques and performance of heterostructure heat mirrors.

Single layer heat mirror films are a subset of a larger class of materials known as transparent conductors. Applications of transparent conductors are not limited to radiative insulation, but include thin film devices such as heating elements for windshields, antistatic coatings, gas sensors, and electrodes for electrochromic or liquid crystal displays.

The most common transparent conductors are the semiconducting oxides SnO_2 , In_2O_3 , and Cd_2SnO_4 . A review of research on these materials prior to 1975 is given by Vossen [6], and the flourish of recent activity in preparation and characterization of transparent conductors has been reviewed by Chopra et al. [7], Jarzebski [8], and Lampert [5]. An incomplete list of some less common transparent conductors includes ZnO , CdS , Cu_2S , NiO and WO_3 .

All these single layer materials are visually transparent

due to an optical bandgap exceeding 2.8 eV. Conduction electrons are generated by dopants (such as Sn in In_2O_3) or through deviations from stoichiometric composition (such as oxygen vacancies in SnO_2). To achieve infrared reflection necessary for a heat mirror, exceptionally low resistivities, $\rho < 3 \times 10^{-3} \Omega\text{cm}$, are required. As carrier mobilities in transparent thin films are typically about $20 \text{ cm}^2/\text{Vs}$, large carrier densities greater than 10^{20} cm^{-3} are necessary. For films of thicknesses greater than 400 nm, strong infrared reflection at wavelengths greater than about $4 \mu\text{m}$ is created by the plasma of conduction electrons, as predicted by the Drude model of free electrons [9].

I decided to study single layer heat mirror films due in part to the challenging problem of precise stoichiometry control during deposition and to the lack of existing high rate manufacture of such films. Single layer heat mirrors have previously been fabricated in research deposition systems using only SnO_2 , In_2O_3 , and Cd_2SnO_4 [5]. As a result of my thesis research, good transparency and strong infrared reflectivity have been obtained in ZnO [11,12] and it is now a recognised heat mirror material. Also, I have fully characterized a high rate planar magnetron sputtering technique suitable for deposition of ZnO onto low temperature glass or plastic substrates [13]. These developments have occurred simultaneously with reports by other workers of heat mirror quality ZnO ($\rho < 3 \times 10^{-3} \Omega\text{cm}$) produced by spray pyrolysis [7], reactive evaporation [14], and rf sputtering [15,16].

1.3 DRUDE THEORY OF FREE ELECTRONS

The infrared reflection properties of a semiconductor heat mirror may be modelled by the theory of free electrons as developed by Drude, Zener and Kronig [9]. Conduction electrons are free to move throughout the lattice, with the effects of scattering modelled simply by a damping γ equal to the reciprocal mean free time between scattering events. The derivation of optical constants is easily illustrated in one dimension, where the equation of motion for an electron in an oscillatory field is;

$$m^* \frac{d^2 y}{dt^2} + m^* \gamma \frac{dy}{dt} = -e E_0 \exp(i\omega t) \quad (1.1)$$

where m^* is the electron effective mass. The complex conductivity σ is calculated from the current density;

$$J = -Ne \frac{dy}{dt} = \sigma E_0 \exp(i\omega t) \quad (1.2)$$

where N is the density of electrons. The complex dielectric constant follows immediately from the conductivity;

$$\epsilon = \epsilon_1 + i\epsilon_2 = \epsilon_\infty + i\sigma/\epsilon_0\omega \quad (1.3)$$

where ϵ_∞ is the high frequency lattice contribution to the dielectric constant. The optical constants n and k for the doped semiconductor are then given by;

$$\begin{aligned} \epsilon_1 &= n^2 - k^2 = \epsilon_\infty - \frac{Ne^2}{\epsilon_0 m^*} \frac{1}{(\omega^2 + \gamma^2)} \\ \epsilon_2 &= 2nk = \frac{Ne^2}{\epsilon_0 m^*} \frac{\gamma}{\omega(\omega^2 + \gamma^2)} \end{aligned} \quad (1.4)$$

The damping γ is interpreted as $\gamma = e/m^* \mu$, where μ is the electron mobility. For strongly absorbing films in the IR, the total reflection is simply the reflection at the air-film

interface and is calculated from;

$$r = \frac{(n-1)^2 + k^2}{(n+1)^2 + k^2} \quad (1.5)$$

This calculation of reflectivity requires that films have a thickness that is large compared to the skin depth for infrared photons and is satisfied by thicknesses greater than $0.3 \mu\text{m}$ for typical transparent conductors.

The plasma frequency, ω_p , characterizes the optical properties of the electron plasma by separating the reflective low frequency behaviour from the transparent high frequency behaviour. ω_p is defined when $n^2 - k^2 = 0$ and is given by;

$$\omega_p^2 = \frac{Ne^2}{\epsilon_\infty \epsilon_0 m^*} - \gamma^2 \quad (1.6)$$

Groth and Kauer [18] have rewritten equation (1.4) using only ω_p , γ and ϵ_∞ [18]. Figure 1.1 shows the behaviour of reflection with wavelength for $\epsilon_\infty = 4$ (typical for a semiconducting oxide) and at various values of the ratio ω_p/γ . The position of the reflection edge is determined primarily by the number of carriers, N , whereas the steepness of the edge is controlled by the ratio ω_p/γ . To ensure reflection of room temperature IR radiation (6 to $25 \mu\text{m}$ wavelength), a reflection edge near $\lambda = 3 \mu\text{m}$ is desirable, and corresponds to a carrier density of approximately $3 \times 10^{20} \text{ cm}^{-3}$ in indium tin oxide. A steep reflection edge is also necessary, requiring a small value of γ or a large electron mobility. For the example of indium tin oxide, a value of $\mu = 20 \text{ cm}^2/\text{Vs}$ gives $\omega_p/\gamma = 2$.

In summary, the characteristics of an optically transparent semiconductor film for heat mirror applications

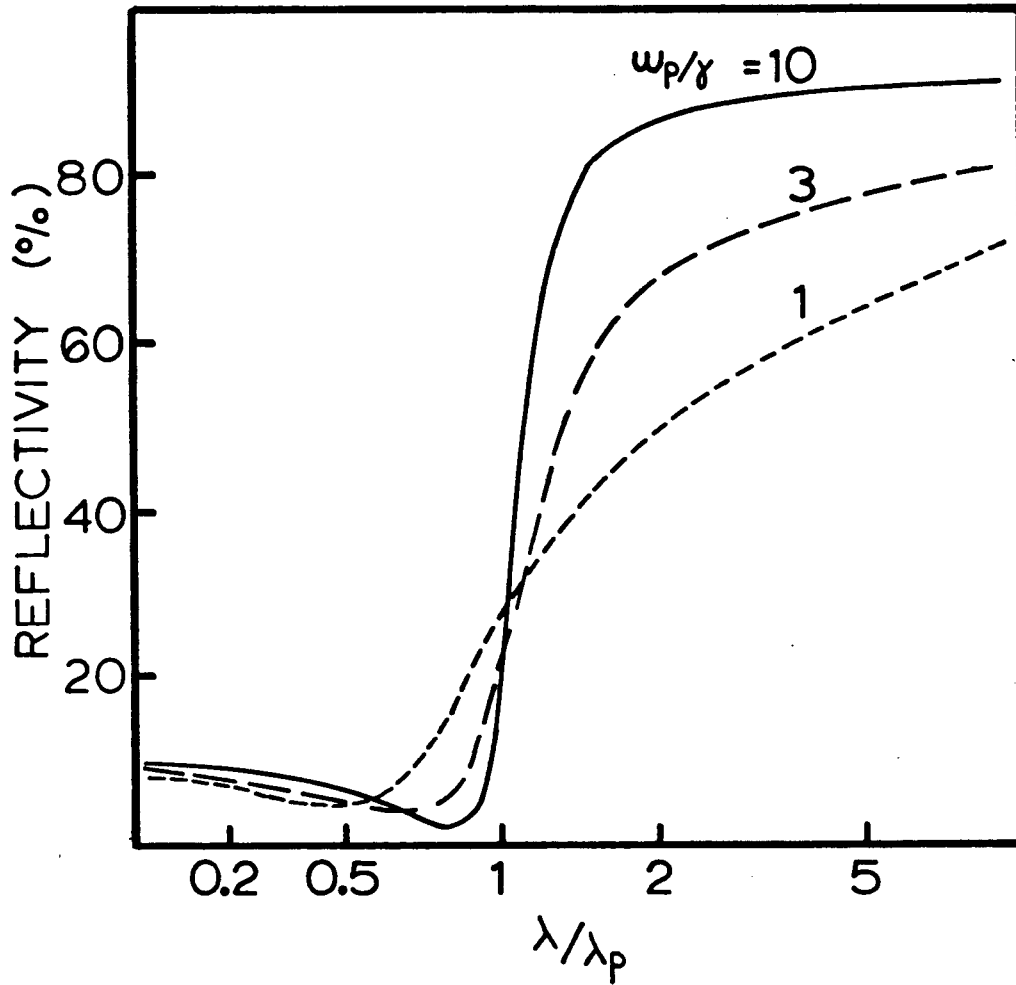


Figure 1.1

The reflectivity of a free electron plasma for various ratios of plasma frequency ω to electron damping γ .

must be; 1) a film thickness exceeding 300 nm, 2) a carrier density near 10^{20} cm^{-3} and 3) a mobility exceeding $10 \text{ cm}^2/\text{Vs}$. Often only the resistivity, $\rho=1/Ne\mu$ (typically $10^{-3} \Omega\text{cm}$) is quoted as a figure of merit for a transparent conductor or heat mirror.

1.4 CHOICE OF ZnO

An ideal single layer heat mirror film for cold climates should possess the following characteristics. Starting materials should be inexpensive, and the film should display no degradation of optical properties with weathering. The film should be optically transparent, which implies a bandgap greater than 3 eV, and this transparency should extend to near $2 \mu\text{m}$ wavelength to reap full benefits from the solar energy spectrum. For commercial applications, it is advantageous to deposit heat mirrors on rolls of plastic sheet, requiring a deposition technique that does not rely on high temperature substrates. An examination of the state of the art of heat mirror materials and technology available in 1981 (at the start of my thesis research) provides motivation and some justification for pursuing zinc oxide as a heat mirror candidate.

In_2O_3 is the most common material for semiconductor heat mirrors. Conductivity is achieved through non-stoichiometry (oxygen deficiency), or by doping with about 5 atomic % F or Sn. ITO is a common abbreviation for indium tin oxide ($\text{In}_2\text{O}_3:\text{Sn}$). High conductivity films have been produced by

sputtering [29,30,31], reactive evaporation [26,27], chemical vapour deposition (CVD) [32] and spray pyrolysis [17,28,33].

Table 1.1 shows the typical characteristics of ITO and other

Table 1.1 Typical properties of oxide heat mirrors.

Material	Resistivity (Ωcm)	Bandgap (eV)	IR Reflection (% at $10\mu\text{m}$)
ITO	4×10^{-4}	3.6	85
SnO_2	7×10^{-4}	>3.5	80
CTO	4×10^{-4}	2.9	84

oxide heat mirrors. These figures are only representative of the characteristics of the best conducting films, since film properties vary greatly with deposition technique. It is seen that ITO is an excellent heat mirror. The only disadvantage ITO may have is the high cost of bulk indium, approximately \$10/ounce for 99.99% purity in 1985 [19], which may limit the cost effectiveness of ITO compared with other coatings.

Conducting SnO_2 has been doped through oxygen deficiency, but the films with lowest resistivities ($<10^{-3} \Omega\text{cm}$) are doped with F or Sb and have been deposited only by CVD or spray pyrolysis [5], techniques requiring substrate temperatures in excess of 600 K. These high deposition temperatures may be necessary for substitutional incorporation of dopant atoms at electrically active Sn sites [8]. Films of $\text{SnO}_2\text{:F}$ have been shown to exhibit good thermal stability of electrical properties after subjection to temperatures exceeding 500 K [20].

Cd_2SnO_4 (CTO) films of resistivity $4 \times 10^{-4} \Omega\text{cm}$ have been prepared by diode sputtering [21,22] and planar magnetron sputtering [23] without heated substrates. Electrical conduction is n-type, created by oxygen vacancies. CTO is known to have good durability and chemical resistance [24]. The bandgap is estimated at 2.1 eV, but the Moss-Burstein effect of bandgap expansion due to conduction band filling can increase the bandgap up to 2.9 eV [25], or a wavelength of 430 nm. However, the transmission in the wavelength region 350 to 450 nm remains significantly lower than that of ITO and SnO_2 heat mirrors.

It is seen from the previous discussion that ITO, CTO and SnO_2 all have some characteristic that renders them unsuitable as an "ideal" heat mirror. ZnO was of interest as a new potential heat mirror material because it is inexpensive, has an optical bandgap near 3.2 eV, and, prior to the start of my research in 1981, had been deposited by reactive evaporation [34] and spray pyrolysis [35] at resistivities between 10^{-3} and $10^{-2} \Omega\text{cm}$. Later, in 1981, Webb and Williams [15] showed that low resistivity ZnO ($2 \times 10^{-3} \Omega\text{cm}$) could be produced by rf sputtering. These developments were motivated by the application of ZnO to transparent window electrodes for solar cells and, as such, were not concerned with optimization of infrared reflection properties.

1.5 PROPERTIES OF ZnO

The characteristics of single crystal and sintered ZnO were the subject of intensive study in the 1950's due to its varied use as a phosphor, enamel pigment and catalyst. These developments were reviewed by Heiland et al. in 1959 [36], and have formed a strong groundwork for understanding the optical, electrical and mechanical properties of ZnO thin films. ZnO is a direct bandgap, n-type semiconductor that crystallizes in the hexagonal wurtzite lattice. Figure 1.2 shows the electronic energy levels of important native imperfections in ZnO, as estimated by Kroger [37]. The first donor levels of oxygen vacancies and zinc interstitials are located about 0.05 eV below the conduction band edge. Previously, Zn interstitials were believed to be active in providing conduction electrons, as evidenced primarily by experiments of Zn diffusion into ZnO single crystals [36]. But the chemical nature of the shallow donor in ZnO is presently controversial due to ESR detection of donors from oxygen vacancies [38]. Dopants of Ga and In form electrically active shallow donors that reside substitutionally at Zn sites [39,40]. The electron effective mass has been measured by Baer [41] using Faraday rotation and is found to be $0.24m_0$.

Recently there has been great interest in stoichiometric thin films of ZnO for use in acoustic wave devices [42,43] and thin film pressure transducers [44]. ZnO is piezoelectric and possesses a high electromechanical coupling coefficient. Whereas conducting films require doping through Zn excess,

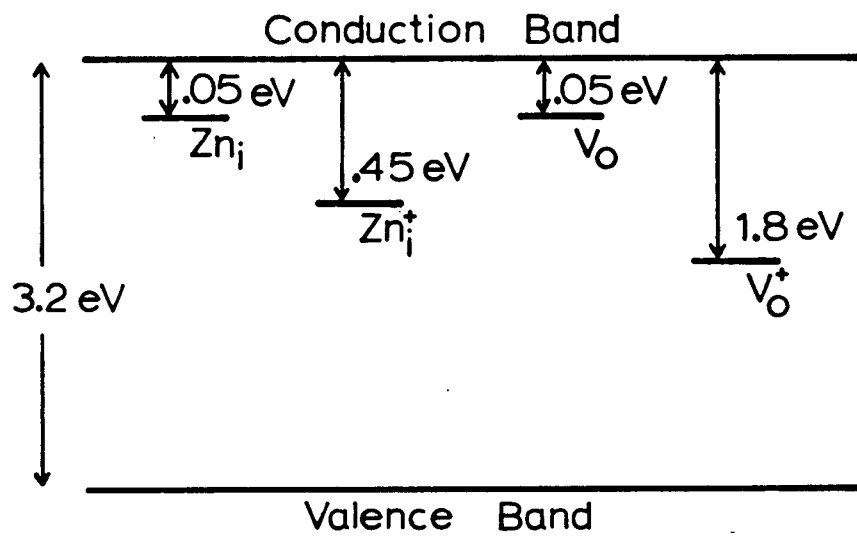


Figure 1.2

Electronic energy levels of native imperfections in ZnO at temperature 300 K.

films for acoustic wave devices are ideally defect-free and have a preferred orientation of polycrystals.

1.6 DEPOSITION PROCESSES

A deposition process ideal for commercial manufacture of heat mirrors should be high rate with the ability to coat plastic substrates, should have good control of film composition and uniformity throughout the coating, and should utilize inexpensive target materials. A brief survey of standard deposition techniques is given below, followed by comparison to, and description of, planar magnetron sputtering.

In chemical vapour deposition (CVD), gases are introduced to a chamber at a constant flow rate where they react and form a coating on a heated substrate. Roth and Williams [45] have deposited ZnO by reacting gases of diethyl zinc and oxygen on substrates with temperatures in the range 560 to 760 K. Deposition rates approached 40 nm/min, which is considered slow for CVD [46].

Fundamentally similar to CVD is spray pyrolysis, where chemicals are sprayed onto a heated substrate in aerosol form. A high consumption of chemical occurs due to vapourization of many aerosol droplets before they react on the substrate. Aranovich et al. [35] have sprayed an aqueous solution of ZnCl_2 onto substrates of temperature 620 to 760 K. Coatings of ZnO were formed and a waste product of HCl gas liberated. Typical deposition rates were 60 nm/min.

Morgan and Brodie [14] have recently described a reactive evaporation process capable of depositing high conductivity ZnO. Zn metal was evaporated through a low pressure oxygen discharge onto unheated glass substrates at deposition rates of about 20 nm/min. The oxygen pressure, power of the discharge, and Zn evaporation rate were controlled independently to optimize the oxidation of zinc.

It is seen that the fundamental limitation of CVD and spray pyrolysis is the requirement of heated substrates to activate the deposition process, rendering them unsuitable for coating of plastic sheet. The reactive evaporation technique shows excellent promise if the difficulties of composition and thickness control over large areas can be overcome, and if the deposition rate may be increased.

Alternatives to the above-mentioned deposition processes are the wide variety of sputtering configurations and techniques, reviewed in detail by the standard texts of Vossen and Kern [47] and Bunshah [48]. Of these, magnetron sputtering (planar or cylindrical geometry) is the recognised high rate sputter process and will be described in some detail. A glow discharge plasma (usually of Ar) is created in front of a cathode (the target material) by rf or dc excitation. Electrons flowing from the cathode cross the positive space charge sheath or darkspace surrounding the cathode and then ionize Ar atoms in the glow region by electron impact ionization. These Ar⁺ ions bombard the cathode, and by momentum transfer target atoms are sputtered

from the surface and may subsequently deposit on a substrate situated beyond the glow discharge plasma. The plasma is self-sustaining through the emission of secondary electrons from the target due to Ar^+ ion bombardment.

Magnets behind the target generate a magnetic field above the target (hence 'magnetron') that constrains electrons to movement near the target surface, thus increasing the efficiency of Ar ionization and subsequently the ejection rate of target material. A further advantage of a magnetron source is that the substrate is not heated by stray electrons from the cathode. Dc sputtering is restricted to conducting targets, such as Zn metal, whereas rf sputtering must be used for non-conducting pressed oxide targets such as ZnO. Reactive sputtering involves the addition of gas(es) that react at the target and/or the substrate to form a desired compound.

Webb and Williams [15] have used rf reactive magnetron sputtering from a ZnO target to deposit conducting ZnO films at deposition rates near 6 nm/min. A serious disadvantage of sputtering from an oxide target is the low sputter yield (atoms ejected per bombarding Ar^+ ion) compared to that of metal targets. Zinc has one of the highest sputter yields of any element, approximately 4.6 at 300 V [137], whereas ZnO has a yield of 1.1 [85]. Also, oxide targets tend to be more expensive and more difficult to machine than metal targets.

Reactive magnetron sputtering from a metal target in an Ar/O_2 atmosphere was the deposition technique used for my

thesis work. It has deposition rates of typically 20 to 100 nm/min and does not necessarily require heating of the substrate to activate film deposition. The geometry of a planar magnetron system may be easily scaled up to provide deposition and control over large areas [49]. Zinc targets are relatively inexpensive and easy to machine to specifications. The major difficulty of this technique lies in maintaining a metal target surface to ensure high rate sputtering, while fully oxidizing the sputtered zinc that arrives at the substrate.

During magnetron sputtering of ITO and SnO_2 , Howson et al. [50] promoted film oxidation by developing a subsidiary rf glow discharge at the substrate. This technique, known as ion plating or bias sputtering, has been used for many years to improve the mechanical properties of films and the tribological properties of machine tools and bearings. The rf power is usually monitored by the negative dc self-bias voltage that occurs at the substrate (hence 'bias sputtering'). A full review of the ion plating process is given in Chapter 4, where it is more timely. It suffices to say here that the major mechanism of ion plating was believed by Howson to be generation of ionized oxygen species and acceleration of these species towards the negatively biased film. Of less importance, the bombarding species were believed to add surface energy to the film and consequently enhance crystal growth [51].

In tandem with an rf discharge at the substrate, Maniv et

al. [23] utilized a reactive gas baffle at the target, which assisted in keeping the metal target surface free from oxidation in the Ar/O₂ sputtering gas mixture. A metal box with a series of slot shaped apertures was built surrounding the planar magnetron target. This geometry decreased the oxygen flux to the target by providing a getter surface for oxygen near the target.

In summary, it was decided to investigate the potential of transparent, conducting ZnO as a heat mirror, deposited by reactive planar magnetron sputtering. Metal targets are inexpensive and ZnO is known to have a suitable bandgap of 3.2 eV. Zn would be sputtered from a metal target surface to enable high rate deposition, with a reactive gas baffle protecting the target surface from oxidation. Substrates would be unheated and oxidation of sputtered Zn would be assisted by the application of a subsidiary rf discharge at the substrate.

CHAPTER TWO: HEAT MIRROR DEPOSITION

2.1 APPARATUS AND EXPERIMENTAL METHOD

Figure 2.1 shows a schematic cross section of the planar magnetron sputtering chamber. The chamber was pumped by an oil diffusion pump and a freon cold trap. Regulation of pumping speed during sputter experiments was accomplished with a variable orifice. A 15 cm diameter Zn target of purity better than 99.99% was firmly clamped to a water cooled backing plate containing the magnetron assembly. The electromagnet was used to confine the glow discharge plasma in the shape of a torus directly in front of the target, creating sputtering erosion of the target in a ring pattern. The total area of the erosion region was 40 cm².

A circular reactive gas baffle was attached to the ground shield that was positioned concentrically around the target. The baffle is shown in more detail in Figure 2.2. It was fabricated from aluminum, with a series of 0.64 cm diameter holes drilled in a concentric pattern through the front surface, so that the ratio of open area to total area of the baffle was about 36%. The separation of the baffle from the target surface was 4.5 cm, chosen so that the baffle would not directly interfere with the glow region of the discharge. When in place, the grounded baffle also served as the anode, in lieu of the water cooled anode ring shown in Figure 2.1.

The discharge was powered by a 5 kW, full wave rectified, constant current dc power supply (Plasma-Therm 5000D,

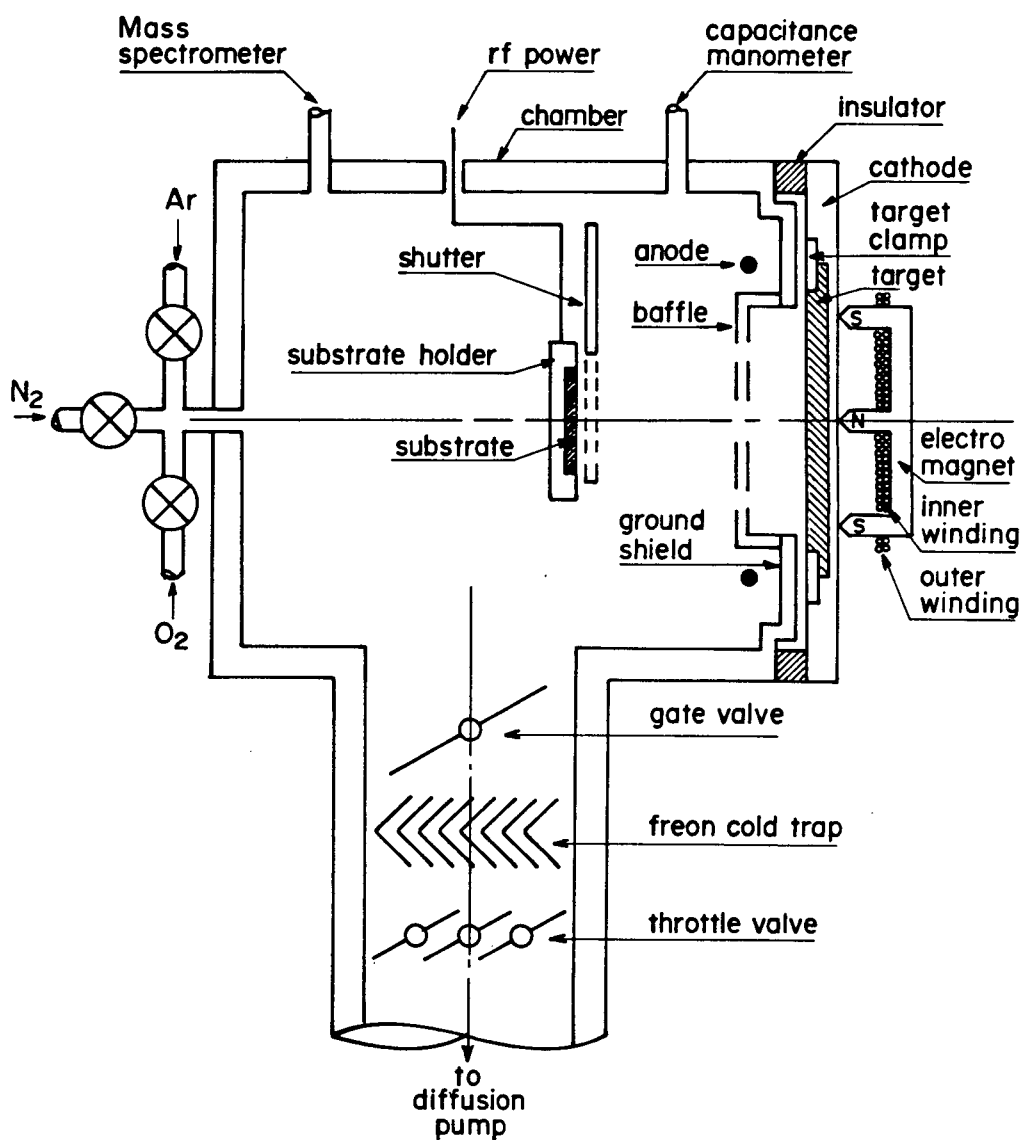


Figure 2.1

A schematic cross section of the sputtering chamber.

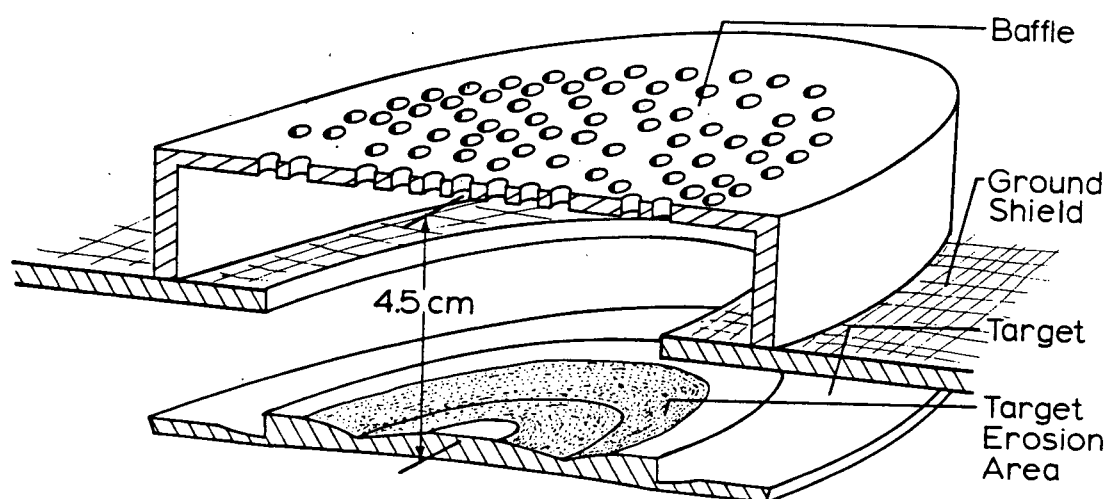


Figure 2.2

The reactive gas baffle. About 36% of the top baffle surface is open.

0-1000V). Pressures during sputtering were measured with an MKS Barytron capacitance manometer, which had a minimum resolution of 0.004 Pa. A UTI-100C quadrupole mass spectrometer was mounted in a side arm near the substrate holder. Flows of high purity Ar and O₂ into the chamber were controlled to $\pm 1\%$ by independent leak valves (Granville Phillips #203) and measured by independent flow meters (Hastings #All-5 or All-10).

The substrate holder and shutter assembly were electrically isolated from the chamber and accommodated six 1x2 inch substrates of Corning 7059 glass or commercial grade quartz. Another substrate holder shown in Figure 2.3 was designed to demonstrate low temperature deposition of films onto 2 inch wide rolls of plastic sheet. The plastic was wound onto a collector spool from a friction-resistive feeder spool, thereby stretching the sheet over an aluminum block positioned in front of the target. Plastics used in this roller system included 6-foot lengths of 13, 25, 50, or 125 μm thick polyester and 150 μm thick polyethylene.

A secondary discharge at the substrate was created by an rf generator (ERatron HFS-8005A at 13.56 MHz) coupled to the substrate holder through a matching network. This discharge was monitored by the negative dc self-bias voltage occurring at the substrate and by the net forward power.

A microcomputer system was used to control and/or for datalogging of all aspects of the sputtering and deposition processes including gas flow rates, total pressure, substrate

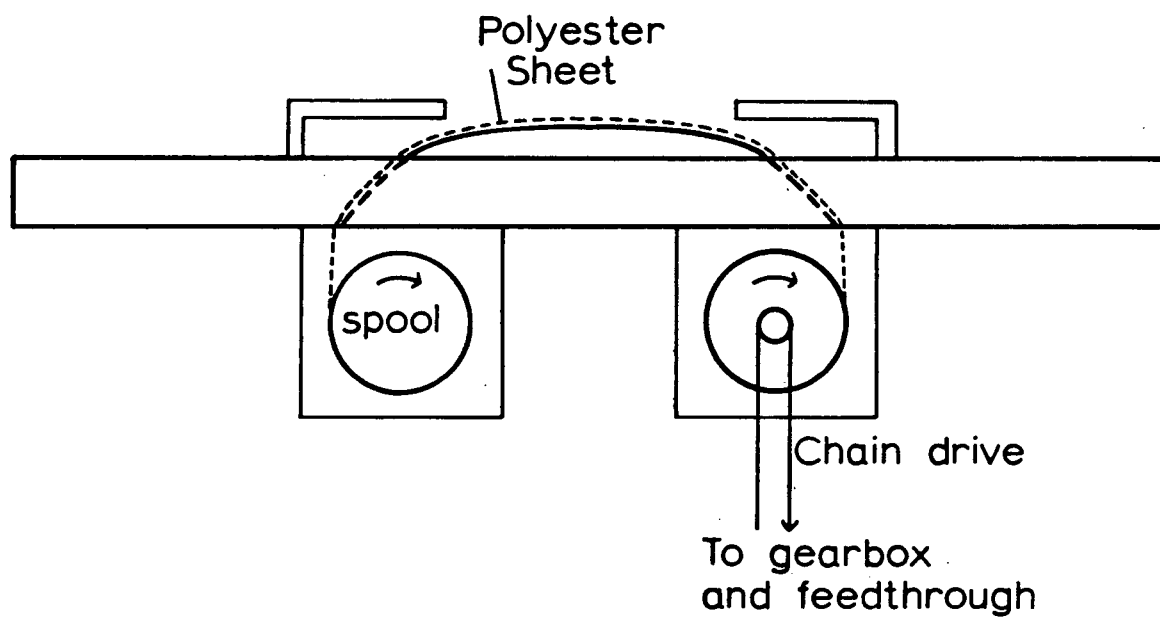


Figure 2.3

A schematic of the substrate holder used for film deposition onto rolls of plastic sheet.

bias, and cathode voltage, current and power. This control enabled a maintenance of precise operating conditions throughout film deposition.

Before deposition, glass or quartz substrates were washed in trichlorethylene and isopropanol [52]. Plastic substrates were mounted as-is without any cleaning. After loading the substrates, the sputtering chamber was baked overnight (about 70°C) and pumped to a base pressure of 4×10^{-5} Pa. The diffusion pump was throttled and Ar admitted at 3.0 sccm (cm^3/min at standard temperature and pressure) to a typical operating pressure of 1.0 Pa. To erase the effects of target history [53] and ensure repeatable starting conditions, the target was sputtered at 150 W in a pure Ar discharge for one hour. The desired flow of oxygen was admitted and again the discharge was left to equilibrate for one hour before film deposition. High partial pressures of oxygen, $pp(\text{O}_2) > 0.05$ Pa, were measured with the capacitance manometer by subtracting the known Ar partial pressure from the total pressure. The mass spectrometer, calibrated at high $pp(\text{O}_2)$ with the capacitance manometer, was used to measure small oxygen partial pressures, $pp(\text{O}_2) < 0.05$ Pa. A typical experiment involved depositing films at various values of substrate bias, with all other parameters held constant. Deposition times were nominally 20 minutes per film, giving film thicknesses of the order of 800 nm. After sputtering, the chamber was baked and backfilled with dry nitrogen gas to atmospheric pressure to avoid condensation on the chamber walls.

Film thickness measurements were made primarily with a Talysurf 4 mechanical stylus instrument using sharp steps created in the film by masking during deposition. Some thickness measurements were supplemented by measurements using optical interference techniques, photography of cross-sections using a scanning electron microscope, and measurement of the mass of the deposited film. These measurements generally agreed to within 10%. Film resistivity measurements were made with a 4 point probe. Infrared reflection measurements for the wavelength range 2.5 to 20 μm were made with a Perkin-Elmer 598 Infrared Spectrometer. Reflection and transmission spectra for wavelengths 350 to 2500 nm were taken by a Beckman UV5270 spectrophotometer with an integrating sphere attachment. The optical spectra had absolute errors of $\pm 2\%$ for infrared measurements and $\pm 1.5\%$ for measurements with the Beckman spectrophotometer. Film morphology and structure were studied with the use of an X-ray diffractometer, a scanning electron microscope, and a transmission electron microscope.

2.2 OPERATING CHARACTERISTICS

In order to control film stoichiometry during growth, the relative arrival rates of Zn atoms and O_2 molecules at the substrate must be regulated. Such control would be achieved if one could smoothly and monotonically vary the partial pressure of O_2 when reactively sputtering Zn from a metal target. However, Figure 2.4 shows that abrupt transitions and

pronounced hysteresis of O_2 partial pressure and cathode voltage occur as a function of the flow of oxygen, $f(O_2)$, admitted to the chamber. A target power of 150 W, an Ar flow rate of 3.0 sccm and an Ar partial pressure of 1.0 Pa were kept constant throughout this experiment. These hysteresis effects during reactive sputtering are well known [54,55] and are explained below.

The partial pressure of oxygen in the chamber $pp(O_2)$, is determined by the flow of oxygen $f(O_2)$, the pumping rate of O_2 by the diffusion pump, and the gettering action of sputtered Zn. Gettering is the chemical combination of Zn deposits with oxygen and has a rate determined by the sputter rate of the target which, in turn, is highly sensitive to the oxidation state at the target surface. It is known that an oxide layer can form on the target surface through two mechanisms [56]; chemisorption of neutral oxygen and ion plating of O_2^+ and O^+ species accelerated towards the surface. At low values of flow $f(O_2)$, $pp(O_2)$ is kept small mainly because of getter pumping of oxygen by sputtered Zn, and the target surface remains metallic. As $f(O_2)$ and consequently $pp(O_2)$ are increased, an oxide layer begins to form on parts of the target surface where sputter erosion is weakest. Since oxides have a much lower sputter yield than metals, the sputter rate is reduced and creates a corresponding reduction in gettering, thus permitting further target oxidation. This positive feedback cycle ultimately produces runaway oxidation of the target surface. A sudden increase of $pp(O_2)$ is seen in Figure

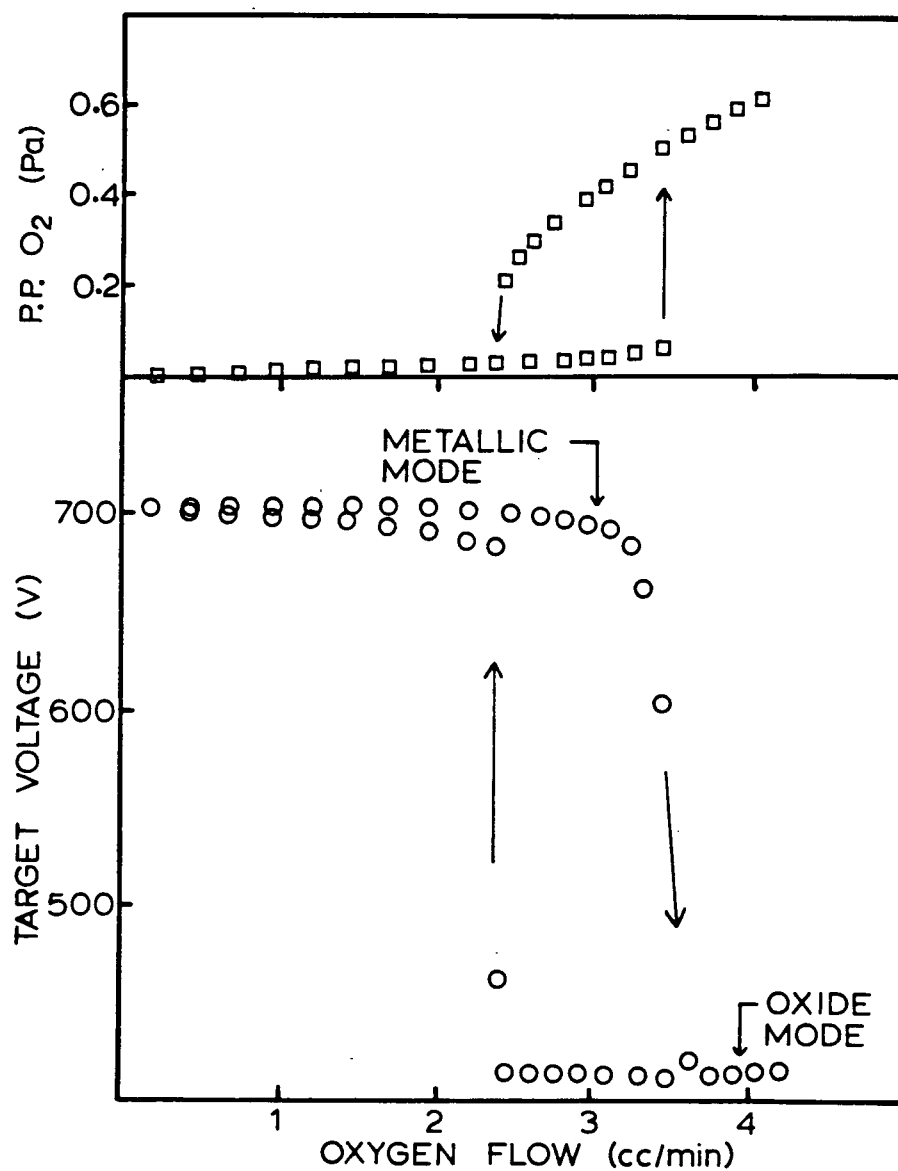


Figure 2.4

Hysteresis in the target voltage and oxygen partial pressure as a function of increasing and decreasing oxygen flow rate. The target power was kept constant at 150 W.

2.4, coincident with a sudden decrease of cathode voltage while operating at constant power. The latter effect is due to both the increased secondary electron coefficient of zinc oxide on the target and the higher total sputtering pressure creating an increase in the cathode current density. In the reverse direction of decreasing $f(O_2)$, the opposite transition occurs with marked hysteresis. It is unfortunate that stable operating points do not exist in the transition regions, because these regions are precisely those of interest in producing oxygen deficient films.

Figure 2.5 shows the corresponding abrupt transition in current I versus cathode voltage V at constant $f(O_2)=2.0$ sccm. At voltages before the abrupt current decrease the target surface is oxidized, while at large voltages the surface is metallic. Affinito and Parsons [56] have shown that for reactive gases that do not chemisorb on the metal target, target coverage is controlled by only the ion plating mechanism. Consequently (due to the slower response of target coverage to ion plating fluctuations), stable operating points can be maintained in the transition region. They were able to deposit films of stoichiometry AlN_x for any value of $x \leq 1$ by precisely controlling the nitride coverage of the aluminum target. Since oxygen chemisorbs onto Zn (as well as for heat mirror materials In, Sn and Cd), control of film stoichiometry for ZnO cannot be accomplished by varying the target surface composition, but must occur through control of oxidation of the growing film at the substrate.

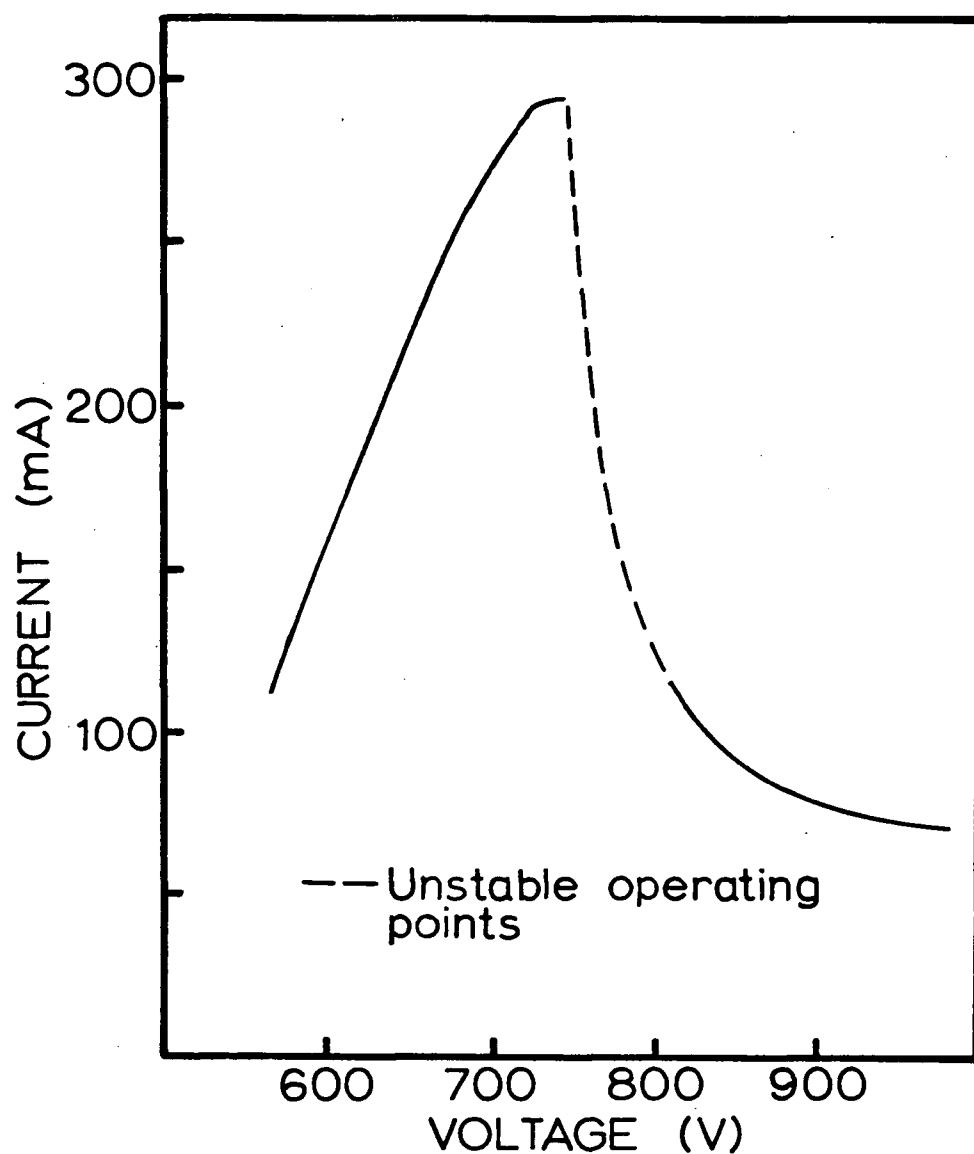


Figure 2.5

The current-voltage characteristic of a Zn target operated in an Ar/O₂ discharge. Total pressure was 1.0 Pa with $f(\text{Ar})=3.0$ sccm and $f(\text{O}_2)=2.0$ sccm.

Figure 2.4 shows the two fundamental operating modes of a Zn target in an Ar/O₂ discharge; metallic target surface and oxide target surface. Films deposited by operation in the oxide mode are characterized by high resistivity, stoichiometric composition due to the large $p_p(O_2)$, and very low deposition rates. To obtain films with slight oxygen deficiency suitable as transparent conductors, normal target operation was in the metallic mode at $f(O_2)$ very close to the transition such that $p_p(O_2)$ was maximized (about 0.03 Pa) near the substrate while maintaining a metal target surface of high deposition rate.

These partial pressures of O₂ were not large enough to enable complete oxidation of sputtered zinc at the substrate. This difficulty was overcome through the use of a reactive gas baffle at the target and an rf discharge at the substrate. As described in section 1.3, by providing a getter surface, the baffle allowed a partial pressure gradient of oxygen across the baffle and, thereby, sufficient oxygen at the substrate for complete oxidation of the Zn flux. The rf discharge was believed to promote film oxidation by excitation and ion plating of oxygen species. A nominal operating condition for the rf discharge was -100 V self-bias at a power of 20 W over a substrate holder of surface area 1070 cm².

2.3 ZnO HEAT MIRRORS

Many unsuccessful attempts were made to produce transparent ZnO from the metallic operating mode without the use of the baffle and the substrate rf discharge. Films produced were brown or black in colour with resistivities not lower than $10^{-2} \Omega\text{cm}$. Confirmation of this difficulty in production of transparent, conducting ZnO by planar magnetron sputtering was recently provided by Maniv et al. [57]. However, transparent films could be made by tripling the standard target to substrate distance of 10 cm. The deposition rate at the substrate decreased by a factor of about 10, allowing ample time for each deposited Zn atom to oxidize in the small partial pressure of O_2 . Such a technique required three hours for deposition of a film of thickness $0.7 \mu\text{m}$ and obviously is not desirable for commercial or even research purposes. All further ZnO films described in this thesis were produced using both the reactive gas baffle and an rf discharge, unless explicitly stated otherwise.

Figure 2.6 shows ZnO film resistivity and infrared reflectivity at $10 \mu\text{m}$ wavelength plotted as a function of the self-bias voltage induced at the substrate by the rf discharge. These films, of nominal thickness 900 nm, were deposited on $125 \mu\text{m}$ thick polyester sheet at a cathode power of 150 W, with $f(\text{O}_2)=2.3 \text{ sccm}$ and $f(\text{Ar})=3.0 \text{ sccm}$. At low negative bias the films were characterized by high resistivities and a dark metallic appearance. As the rf power, and subsequently the dc bias, are increased, a

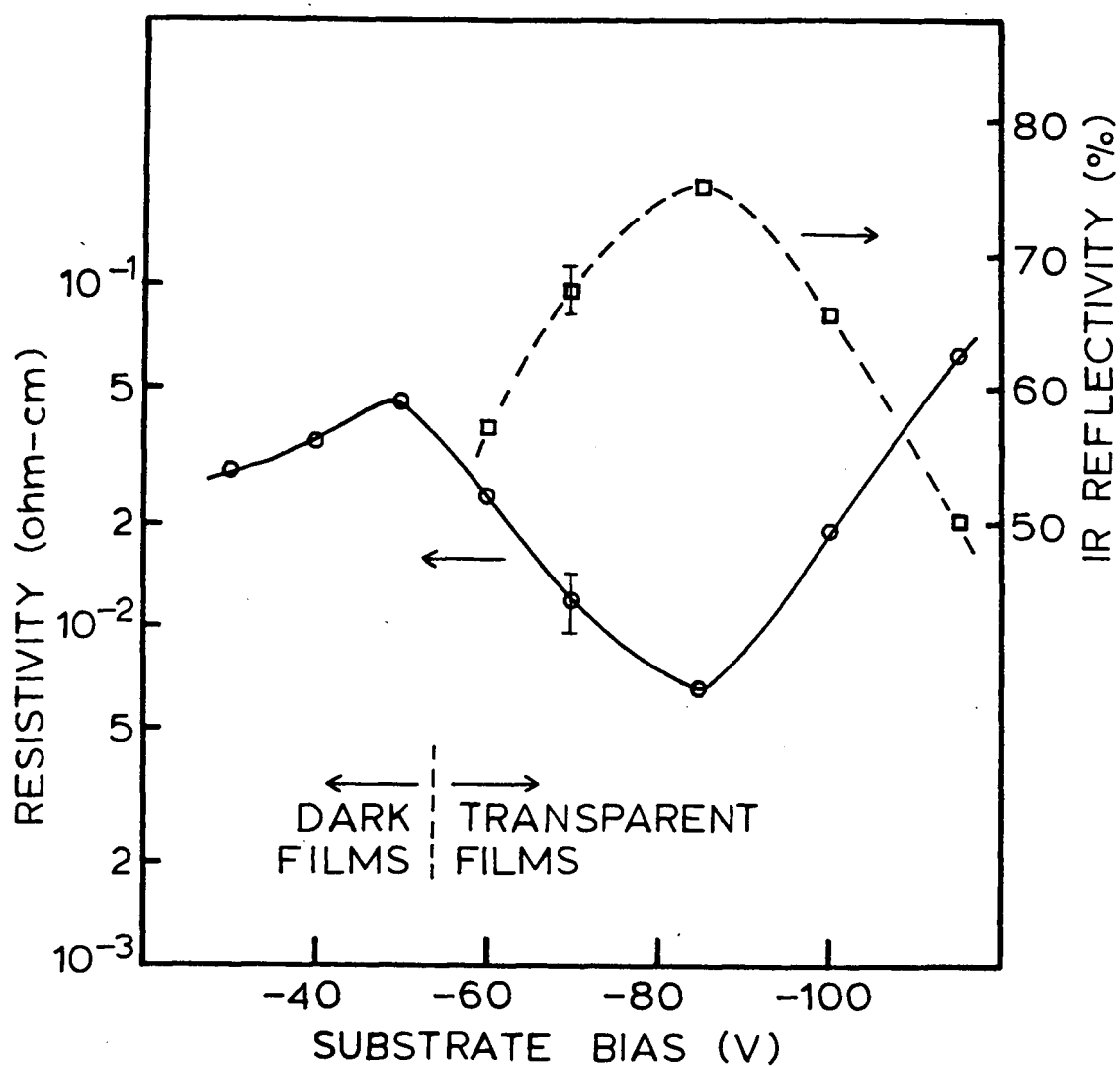


Figure 2.6

ZnO resistivity (circles) and infrared reflectivity at $10\text{ }\mu\text{m}$ wavelength (squares) as a function of substrate bias for films deposited on polyester sheet.

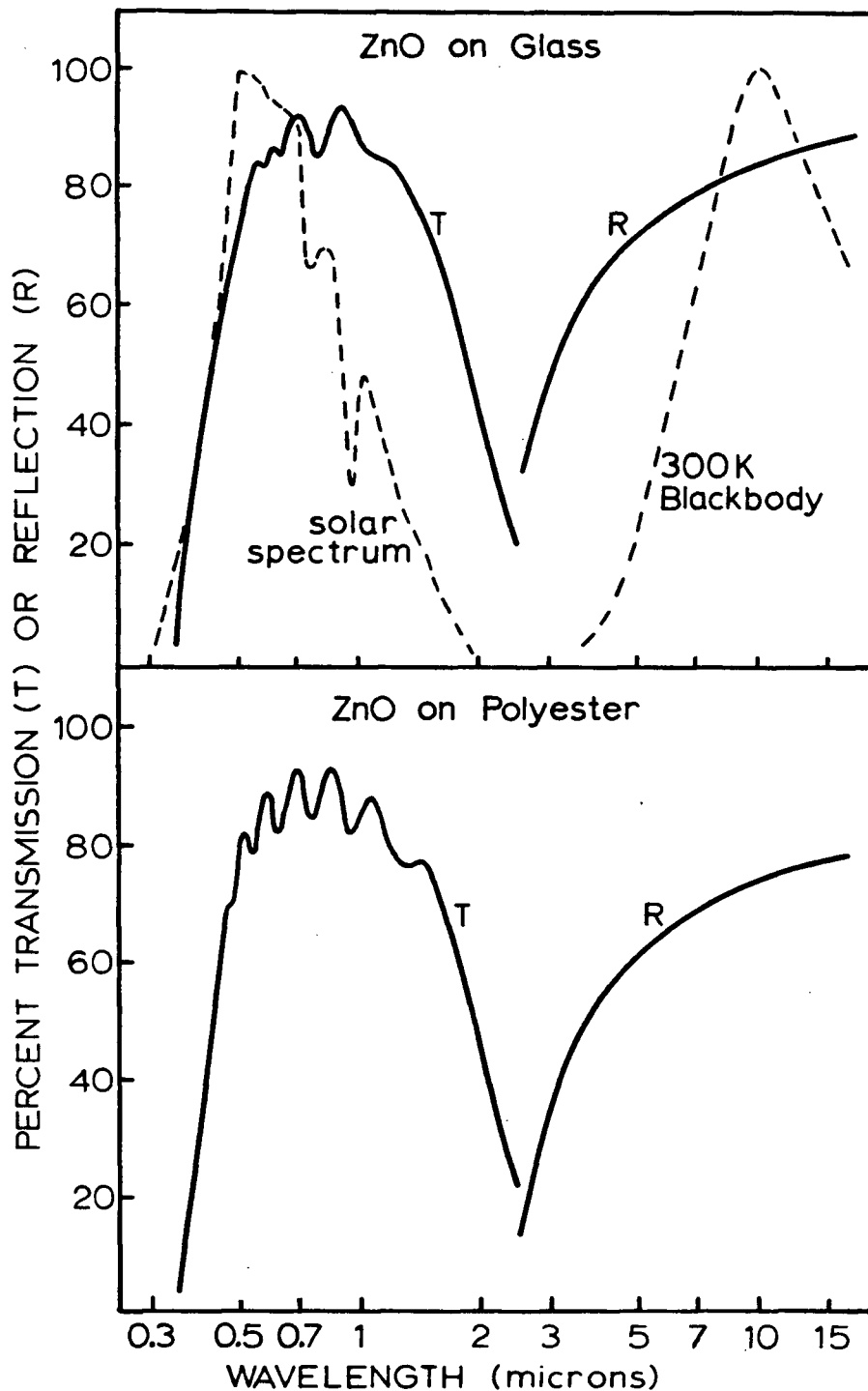


Figure 2.7

Transmission and reflection characteristics for ZnO heat mirrors deposited on both glass and polyester substrates. Normalized to 100% are the solar irradiance (AM1) and the infrared emission from a blackbody at 300 K.

transition in film characteristics is observed to low resistivity and good optical transparency. A maximum in infrared reflectivity occurred for the film of lowest resistance. This behaviour was typical for that of many hundreds of ZnO films sputtered. The film deposition rate of about 75 nm/min was larger than the rate of films sputtered on glass substrates because the glass substrate holder had a shutter in front of the films that effectively reduced the deposition rate by shadowing sputtered Zn atoms arriving at oblique angles of incidence.

Figure 2.7 shows transmission and infrared reflection characteristics of heat mirror quality ZnO produced on both 125 μm thick polyester and Corning 7059 glass substrates. For evaluation of heat mirror performance, the solar irradiance and the infrared emission from a blackbody at 300 K are shown. The film on polyester was 900 nm thick with resistivity $3 \times 10^{-3} \Omega\text{cm}$ whereas the ZnO on glass was 700 nm thick and had a resistivity of $2 \times 10^{-3} \Omega\text{cm}$. The interference structure, seen in the transparent region of these spectra, will be utilized in Chapter 5 to determine the optical constants of ZnO. It should be noted that the transmission characteristics of both films were obtained using a double beam spectrometer with an uncoated substrate in the reference beam. For the ZnO coating on glass, the average transmission to solar energy is about 75% and the percent reflection of radiation from a 300 K blackbody is estimated as 85%. In comparison, the transmission to solar energy of uncoated glass is 92% and the average infrared reflectivity is 7%.

2.4 ITO HEAT MIRRORS

To enable comparison of ZnO to a standard heat mirror material, indium tin oxide (ITO) heat mirrors were fabricated using the same deposition technique. The Zn target was substituted for an alloy target of composition 90% In and 10% Sn. Films were sputtered on glass and 13 μm thick polyester substrates at a cathode power of 150W, $f(\text{Ar})=1.50$ sccm, $f(\text{O}_2)=1.87$ sccm and a total gas pressure of 1.1 Pa. Figure 2.8 shows the solar transmission and infrared reflection characteristics of a 400 nm thick ITO film on glass with resistivity $9 \times 10^{-4} \Omega\text{cm}$. As with ZnO, the transmission spectra were obtained with an uncoated substrate in the spectrometer reference beam. Films produced on polyester had identical infrared reflection and resistivity values. At the time of publication of these results, such resistivities were believed to be the lowest reported for ITO on plastic sheet.

The ITO films had heat mirror characteristics very similar to the ZnO films; the ITO coating on glass had an average integrated solar energy transmission of 76% and an 87% reflection of 300 K blackbody radiation. One advantage of the ITO films was the lower resistivities obtained than in ZnO. Thus a thinner layer of ITO heat mirror could be used to exhibit the same infrared reflection as ZnO.

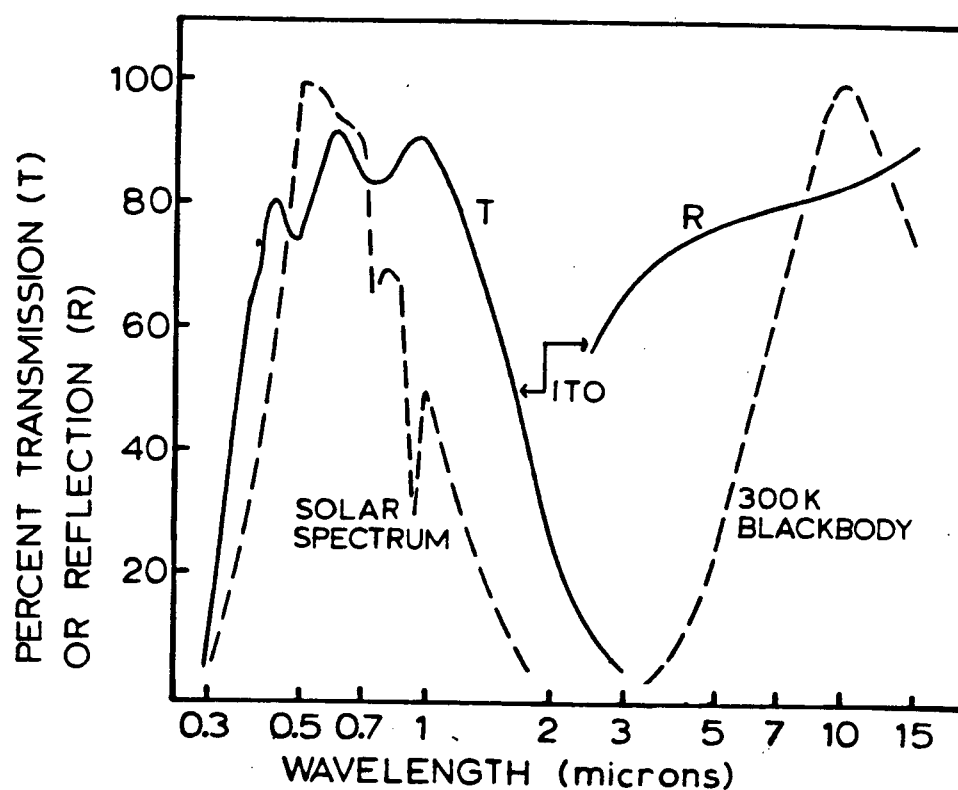


Figure 2.8

Transmission and reflection characteristics of an ITO heat mirror on a glass substrate. Normalized to 100% are the solar irradiance (AM1) and the infrared emission from a blackbody at 300 K.

2.5 SUMMARY

The properties of the first ZnO heat mirrors deposited by a sputter technique have been reported in this chapter. During high rate, reactive sputter deposition onto plastic substrates, a reactive gas baffle was used to control target oxidation and a substrate rf discharge enabled optimization of film properties. The best ZnO heat mirrors had a transparency to solar radiation of 75% and an average reflection of 85% for 300 K radiation. The only other report of heat mirror properties of ZnO is by Morgan and Brodie [14], who produced films of transparency 80% and infrared reflectivity 66% by reactive evaporation. The details of their calculation of transparency were not given.

Despite successful ZnO heat mirror deposition, the mechanisms of control of film characteristics by the rf discharge and of target oxidation by the baffle were not at all well understood. For commercial application of ZnO coatings, a greater understanding of the deposition technique would be required. Thus the emphasis of my research was shifted from heat mirror optimization and testing to performing a series of experiments to demonstrate the effectiveness of the baffle and, most important, to identify processes induced by the rf discharge that control and enhance film properties.

CHAPTER THREE: THE REACTIVE GAS BAFFLE

The technique of using a getter surface or reactive gas baffle surrounding the target in order to enhance substrate oxidation was first used by Schiller et al. [53] to produce oxides of Ti and Ta and by Maniv et al. [23] for Cd_2SnO_4 films. However, these authors did not provide any data concerning the characteristics or operative mechanisms of the baffle, but reported only film properties produced with/without baffling. The baffle was presumed to decrease oxygen flux to the target by providing a getter surface and also decrease metal flux to the substrate, thus increasing the ratio of O_2 /metal atoms striking the substrate surface. The following investigations were undertaken to clearly demonstrate the effectiveness of a reactive gas baffle.

The partial pressure of oxygen, $pp(\text{O}_2)$, near the substrate was measured as a function of the flow of oxygen admitted to the chamber for cases of sputtering with and without a baffle surrounding the target. The results are shown in Figure 3.1 for a cathode power of 150 W and an Ar partial pressure of 0.75 Pa in both cases. The cathode was operating in the metallic mode of target coverage. The deposition rate for Zn sputtered in a pure Ar discharge with a baffle was found to vary between 25 and 40% of the deposition rate without a baffle. The variation was due to accumulation of sputtered deposits and clogging of holes in the baffle over the course of many experiments.

Clearly, the use of a baffle creates a substantial

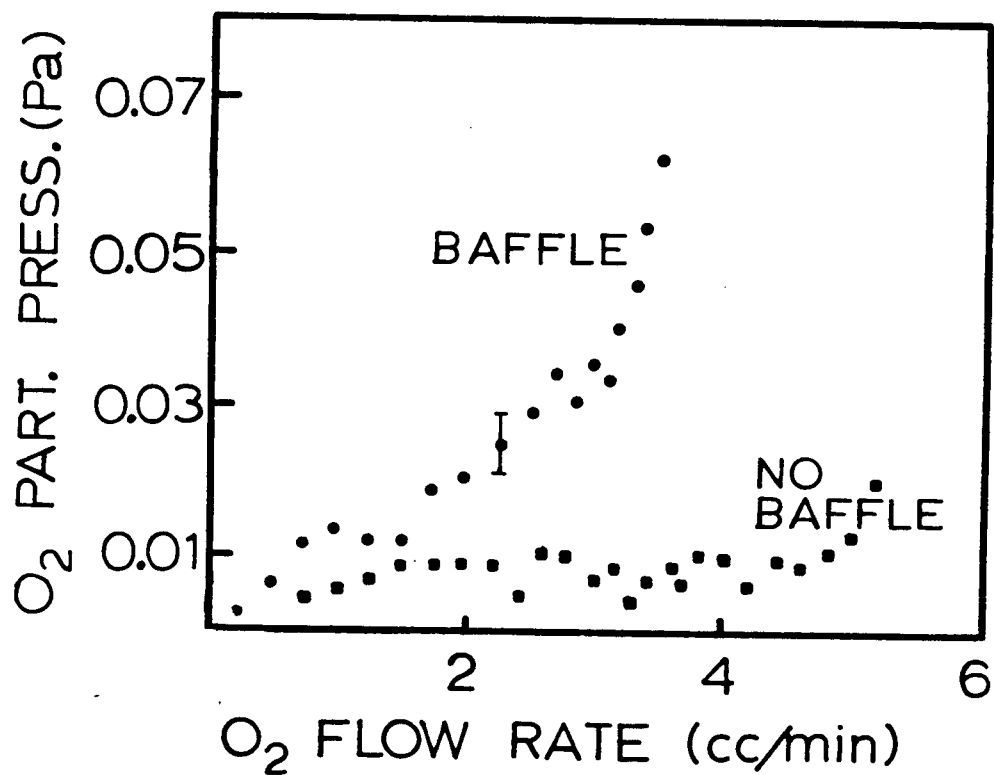


Figure 3.1

Enhancement of oxygen partial pressure near the substrate through the use of a reactive gas baffle. The target power was 150 W for both cases.

increase in oxygen partial pressure at the substrate, and decreases the deposition rate of sputtered metal. The combination of these effects provides a four or five-fold increase in O_2/Zn arrival rates at the substrate, enhancing the oxidation of growing films. The baffle is able to utilize about 65% of the sputtered metal flux to getter oxygen in the target vicinity. Even for low flow rates of O_2 (2 sccm), the remaining metal flux passing through the baffle is not enough to completely getter all oxygen in the much greater chamber volume, resulting in an increased oxygen partial pressure near the substrate. In addition, the long molecular mean free path (about 1cm at 1Pa) and decreased molecular conductance presented by the baffle help maintain an O_2 pressure differential between the substrate region and the target region.

A further advantage of the baffle was discovered in conjunction with use of an rf discharge at the substrate. Kominiak [58] has observed minor interactions between an rf powered discharge at the target and a dc biased substrate. Similar interactions between a dc target discharge and an rf substrate discharge might hamper the precise control required for bias sputtering of films of specific stoichiometry. In Figure 3.2 the dc target current is shown as a function of substrate bias for cases with and without a reactive gas baffle. In both cases the target power is kept constant at 150 W. A small increase in target current with increasing substrate bias is seen for the case of no baffle. This dc

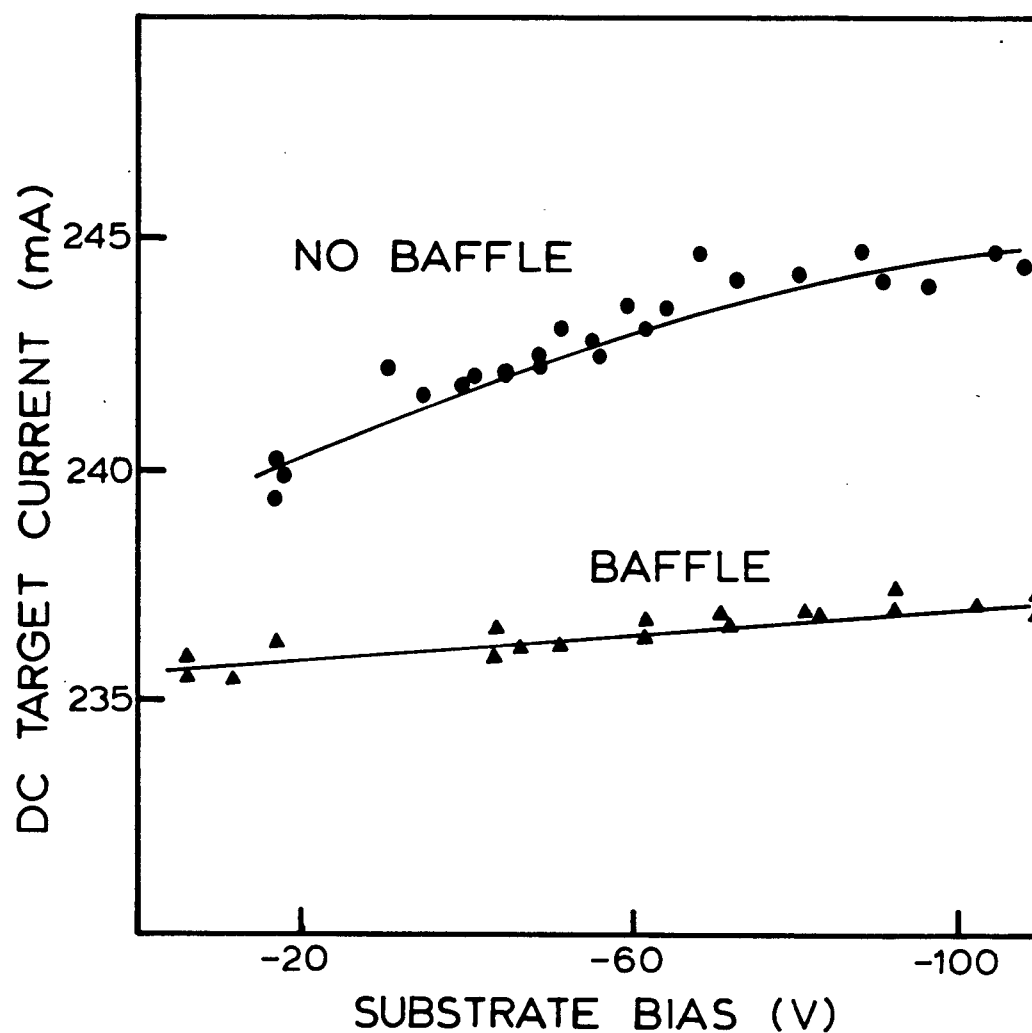


Figure 3.2

Effect of the rf substrate discharge on the dc target operating characteristics. The target power was held constant at 150 W for cases with and without a reactive gas baffle.

current increase is attributed to a feeding of ions from the rf discharge to the dc discharge, due to the large spatial extent of the rf glow region. Clearly the rf discharge has a negligible effect on the I-V characteristics of the target when the baffle is included. Thus an added benefit of a reactive gas baffle is to reduce the rf-dc plasma interaction and subsequent ion-feeding by separating the two plasmas with a partially open grounded plane.

CHAPTER FOUR: THE SUBSTRATE RF DISCHARGE

4.1 PROPERTIES OF AN RF GLOW DISCHARGE

Several authors have recently provided excellent reviews of the properties of an rf glow discharge, specifically for applications to sputtering [59,60,61]. In my sputtering system, rf power is applied to the substrate through a standard L-C matching network that includes a blocking capacitor in series. In this configuration, the substrate is called a 'capacitively coupled' electrode with the series capacitor preventing a dc short to ground.

Electrons have a much higher mobility in a glow discharge plasma than massive argon ions. Thus, a large electron current can flow during the positive half of an rf voltage applied at an electrode. However, during the negative cycle, only a relatively small ion current can flow. To conserve charge the substrate must self-bias to a negative dc voltage until the net current averaged over each cycle is zero. The negative dc potential creates a darkspace or sheath above the surface of the substrate electrode, in the same manner as the dc powered cathode. The voltage established at the substrate may be written;

$$V(t) = V_0 + V_1 \sin \omega t \quad (4.1)$$

where the absolute value of the dc voltage, V_0 , is not greater than V_1 . For my system, $f = \omega/2\pi = 13.56$ MHz. A simple model of the rf discharge assumes that the low mobility ions only see the dc voltage, whereas electrons may oscillate in the rf

field. These oscillating electrons can acquire sufficient energy to ionize argon atoms, thus maintenance of the glow discharge does not rely solely on secondary electrons emitted from the substrate.

The voltage across the sheath at the substrate, V_s , is determined by the difference between the plasma voltage V_p and the bias voltage, V_0 ; $V_s = V_p - V_0$. It is known that the plasma floats at a potential higher than the potential of any surrounding surfaces. Coburn and Kay [63] have shown that V_p is dependent on the ratio of target area to the area of all other surfaces in contact with the glow. The sputter system of Figure 2.1 has a substrate to chamber ground ratio of $1070\text{cm}^2/6000\text{cm}^2$ or 0.17. This large asymmetry of electrodes leads to small plasma voltages, $V_p = 10\text{ V}$, at a bias of -100 V [63]. Thus to a first approximation, the voltage across the substrate sheath may be equated to the bias voltage, $V_s = V_0$.

It is evident that for $V_p > 0$, a sheath will also be formed at the ground electrode (chamber wall). The ratio of electrode sheath voltages has been predicted by Koenig and Maissel [66] to vary with the fourth power of the inverse area ratio;

$$V_{s1}/V_{s2} = (A_2)^4/(A_1)^4 \quad (4.2)$$

Experimental results confirm this general behaviour but have shown the exponents in (4.2) to be closer to 1 [59]. Of interest in this work, it is seen that for strongly asymmetric electrodes, the smaller electrode (substrate) will receive high energy bombardment whereas the large electrode (chamber

wall) receives a particle flux of much lower energy.

To assist in interpretation of the effects of an rf discharge, it is useful to estimate the energy distribution and flux of ions arriving at an rf powered substrate. Due to the separate current contributions of electrons and ions, the ion current may not be calculated from the power-voltage characteristic of the discharge, but from characteristics of the substrate sheath. Thornton and Penfold [62] have modified the Child-Langmuir law of space charge limited current to enable calculation of the ion current density to the substrate for rf discharges;

$$JD^2 = 46(40/M)^{1/2} (V_s/1000)^{3/2} \quad (4.3)$$

where D is the maximum sheath thickness in mm, J is the ion current density in mA/cm², M is the ion mass in atomic units and V_s is the voltage across the sheath. To obtain an estimate of the ion current to the substrate, an observed darkspace D=6 mm and M=40 (Ar) were substituted. For a dc bias V₀=-100 V the ion plating current is J=3x10¹⁴ ions/cm²s, if it is assumed that V_s=100 V.

Ions accelerated across the substrate sheath lose energy through two processes; symmetric charge transfer collisions and through rf modulation of the sheath voltage. The latter mechanism shall be discussed first. If the transit time for an ion to cross the sheath is less than the period of the rf oscillation (74ns), then upon reaching the substrate the ion will have an energy related to the rf phase at that instant. The spread of the ion energy distribution, dE, due to rf

modulation was given by Okamoto and Tamagawa as [64];

$$\Delta E = (63V_1/3\pi fD)(2eV_0/M)^{1/2} \quad (4.4)$$

where V_0 is the dc bias, V_1 is the amplitude of rf modulation of the sheath voltage (approximately equal to V_0 for an asymmetric configuration), $f=13.56$ MHz, and M is the ion mass. Substituting values of $V_0=V_1=100$ V yields an energy spread of only 11 eV and a corresponding ion transit time of 870 ns. These results are compatible with the previous comments concerning the slow response of heavy Ar^+ ions. The energy spread is small enough to be neglected in further calculations.

The ion energy distribution created by symmetric charge transfer collisions in the sheath ($\text{Ar}^+ + \text{Ar} \rightarrow \text{Ar} + \text{Ar}^+$) was shown by Davis and Vanderslice [65] to depend on the sheath thickness to ion mean free path ratio, D/L . Although this model was developed for dc discharges, it is used here to estimate the response of Ar^+ ions to the dc component of the substrate voltage. Using the assumptions that the electric field decreases linearly from the cathode to the edge of the glow and that newly created ions start from rest, they derived the following expression for the distribution of ion energies at the cathode;

$$\frac{dN}{dV} = \frac{N_0 D}{V_s L} \frac{1}{2(1-V/V_s)^{1/2}} \exp[-D/L(1-(1-V/V_s)^{1/2})] \quad (4.5)$$

where N is the number of ions of energy eV , and V_s is the voltage across the sheath. Using a charge transfer cross section for Ar of $3 \times 10^{-15} \text{ cm}^2$ at 100 eV [65] gives a mean free path of 3 mm at 1 Pa pressure. Figure 4.1 shows the energy

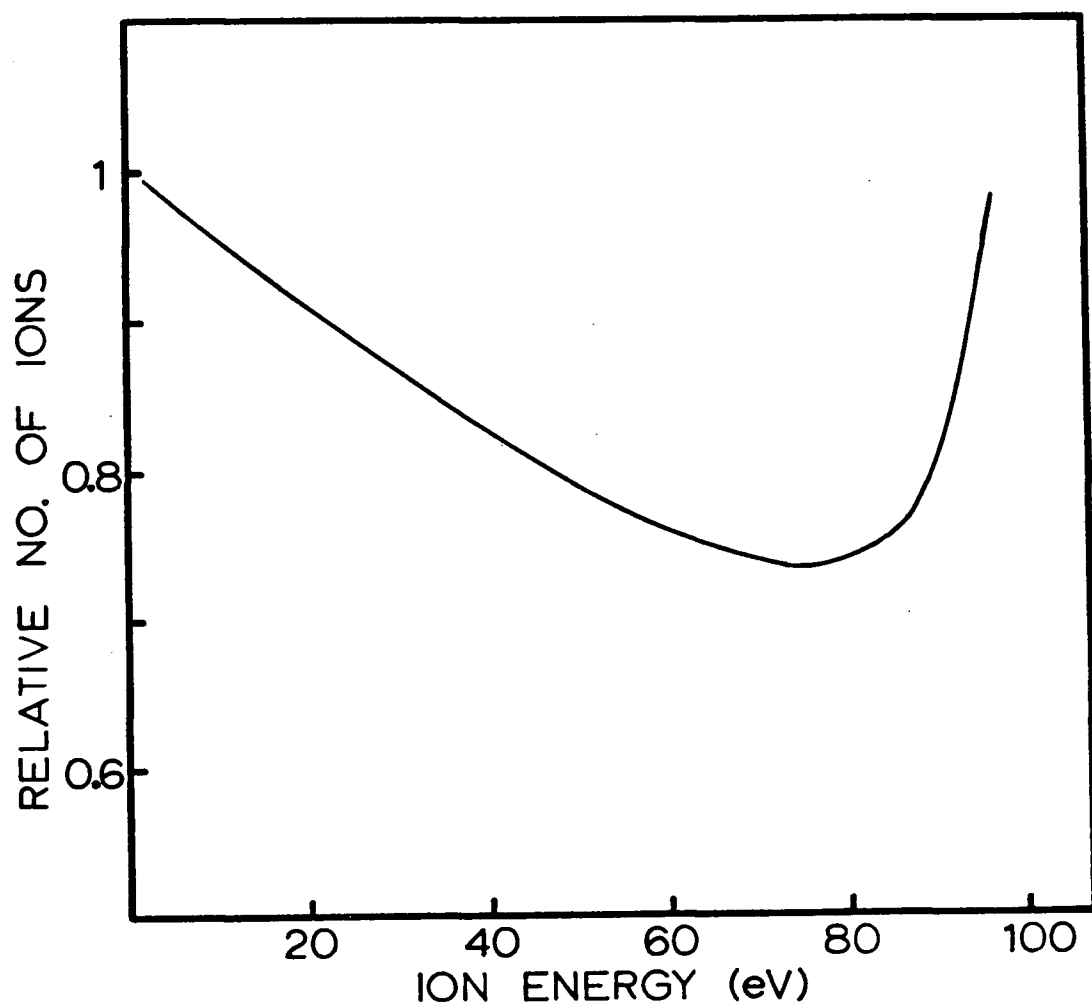


Figure 4.1

Energy distribution of ions arriving at the substrate, calculated from the theory of Davis and Vanderslice using a sheath thickness to ion mean free path ratio of 2 and a substrate bias of -100 V. Not indicated on this graph, 13% of the ions suffer no collisions and arrive at the substrate with energy 100 eV.

distribution for $D/L = 6\text{mm}/3\text{mm}$. The distribution of ion energies is found to be nearly constant from zero volts to the full sheath voltage, and 13% of the ions suffer no collisions. A further experimental confirmation of the model of Davis and Vanderslice was recently made by Machet et al. [67].

In summary, the significant properties of an rf-induced bias of -100 V at the substrate are the bombardment by a flux of 3×10^{14} ions/cm²s with a distribution of energies widely spread about an average of 65 eV , but not exceeding 100 eV . This characterization is pertinent to an understanding of the effects of substrate bias described in the following section.

4.2 EFFECTS OF AN RF DISCHARGE

The substrate ion plating or bias sputter method used in this work is a specific technique of a wide variety of existing ion assisted deposition processes. The first recent use of film deposition using accelerated ions was by Mattox in 1964 [68] to enhance the film adhesion of metallic alloys. Subsequently ion assisted processes have been rapidly adopted in research and industry and include ion plating, plasma activated reactive evaporation, plasma assisted chemical vapour deposition and plasma nitriding. Recent reviews of the properties and effects of these processes are given by Mattox [69,70], Greene and Barnett [71], Thornton [72] and Coad and Dugdale [73].

Ion bombardment of a growing film can affect essentially all film properties. Effects include resputtering, defect

production, inert gas incorporation, heating, stress and crystallographic changes, disruption of surface morphology and changes in film composition. Although a large fraction of research effort has been expended on studies of bombardment effects, especially on metal or metal alloy films, these effects are not as yet completely understood.

Ion bombardment effects may be generally classified by the energy of bombardment [72,69]. At low ion energies <50 eV, loosely bonded impurity or surface atoms may be desorbed by sputtering. For instance, incorporation of impurity Ar atoms in the film may be minimized. For incident ion energies 50 to 150 eV, sputtering and heating of the growing film will increase, coincident with possible crystallographic disruption and/or composition change. At high ion energies $>>150$ eV implantation of bombarding species will occur and subsequently greatly disrupt or amorphize film crystallinity. Such defect production may be counteracted by significant film heating and sputtering.

Ion assisted deposition of metals is known to densify coatings and improve adhesion to the substrate. Densification is characterized by an elimination of columnar or dendritic morphology through the mechanisms of enhanced adatom mobility and material redistribution by resputtering. The composition dependence on substrate bias for metal alloy films has been modelled by several workers [74,75,76], who have shown that metal constituents with higher elemental sputter yields are preferentially resputtered from the growing film surface.

Ion plating has been used to optimize the properties of many reactively sputter deposited metal oxides and nitrides including ITO [51], TiO_2 [77], CTO [23] and TiN [78,79] but surprisingly little investigation of the mechanisms of such 'reactive ion plating' has been performed, as most researchers have been concerned with characterization of film properties. An exception is the work of Barnett and Greene [89], who have successfully used a resputter model similar to the models used for metal alloys, to predict the composition of GaAs films sputtered from a GaAs target. Also, Winters and Kay [80] have bias sputtered W, Au and Ni in Ar/N_2 gas atmospheres. They found an increase in N content with bias for Au, presumably due to implantation of N_2^+ . W and Ni had a decreasing N content with bias, believed to be due to the large sputter yield of chemisorbed nitrogen gas for these metals.

For reactive ion plating of oxide films it has been assumed but not yet proven that film oxidation is enhanced through bombardment of O_2^+ ions and that surface energy created by energetic ions enhances nucleation and crystal growth [51,23]. The following sections undertake an in-depth study of the reactive ion plating process for ZnO and demonstrate that ion plating does indeed increase the oxygen content of the deposited film, as assumed by other workers. The stoichiometry of bias sputtered films was measured and a series of experiments were performed to identify three processes that enhance film oxidation; preferential resputtering of Zn, preferential evaporation of Zn and

activation or ion plating of oxygen species.

4.3 FILM STOICHIOMETRY

Three sets of ZnO films of thicknesses 0.29 to 0.37 μm intended for Rutherford Backscattering (RBS) analysis of stoichiometry were deposited in the metallic mode of Figure 2.4 at various values of applied substrate bias. The first set of films were sputtered onto glass substrates and sent to C. Evans and Associates in San Mateo, California for RBS analysis. Due to oxygen and other elements in the glass substrates, O/Zn stoichiometry ratios could not be deduced. However, a carbon impurity concentration of less than 1% was detected in the films. Furthermore, the film deposited at -100 V bias was found to have less carbon impurity than the film deposited without a substrate discharge.

The two other sets of films were deposited on spectrographic grade graphite stubs and then analyzed at McMaster University in Hamilton by D. Stevanovic. Figure 4.2 shows the backscattered yield versus energy for a typical RBS spectrum obtained from the films on graphite substrates. Backscattered He^+ ions from a 2.03 MeV He^+ beam at normal incidence were detected at a scattering angle of 160° . Zn nuclei present a larger cross section and scatter He^+ at higher energies than oxygen due, respectively, to a larger nuclear charge and mass. Helium ions scattered from the back side of the film are detected at lower energy than those scattered from the surface due to a gradual energy loss by

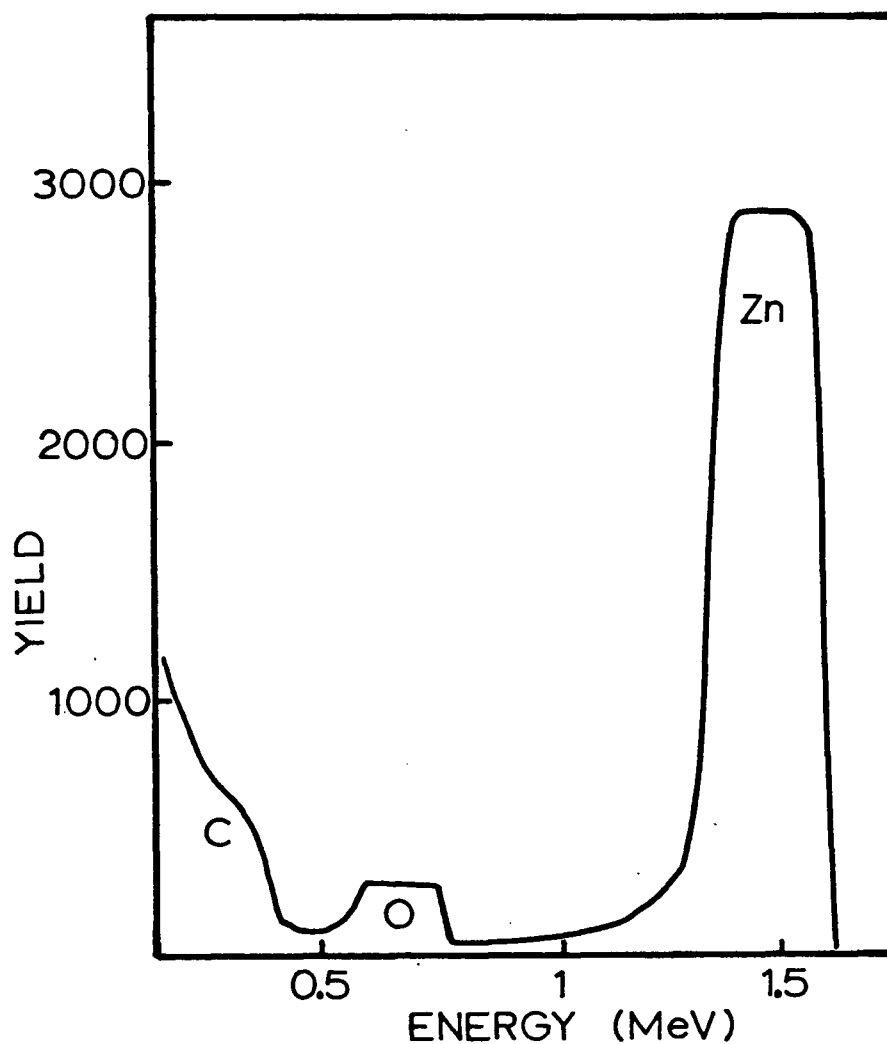


Figure 4.2

A Rutherford Backscatter spectrum obtained from a ZnO film deposited on a graphite substrate. The backscattered yields of He^+ ions from zinc and oxygen atoms in the film and from carbon atoms in the substrate are indicated.

electronic interactions as the ion traverses the film. This energy loss creates rectangular shaped yield spectra. Since the scattering cross sections are small and multiple scattering effects are negligible, the horizontal plateaus of the yield spectra indicate a composition that is uniform with depth. The ratio of oxygen to zinc in the film is simply obtained from the ratio of areas under the spectra multiplied by a cross section correction factor [81]. The detection limit for impurities is generally of the order of 1% or less. No impurities were detected within these limits, however, implanted Ar would be particularly difficult to detect as its yield spectrum partly overlaps that of zinc.

Figure 4.3 gives the oxygen to zinc ratio for each film and the corresponding resistivity for each film. The data points indicated by squares are from one of the sets of films on graphite substrates. They have smaller composition error estimates than the other data indicated by circles due to less tailing in the experimental spectra and a lower background yield. The films at -7 V bias (no rf power) are visually dark brown, the film at -40 V bias is a lighter brown and the remaining films show increasing clarity with increasing bias. This confirms previous assumptions that the colour change was due to an increase in the O/Zn ratio [11]. Notice that the best conducting films are transparent and nearly stoichiometric with a slight zinc excess, compatible with the suggested mechanisms of ZnO conduction by oxygen vacancies or zinc interstitials. In summary, the substrate bias is shown

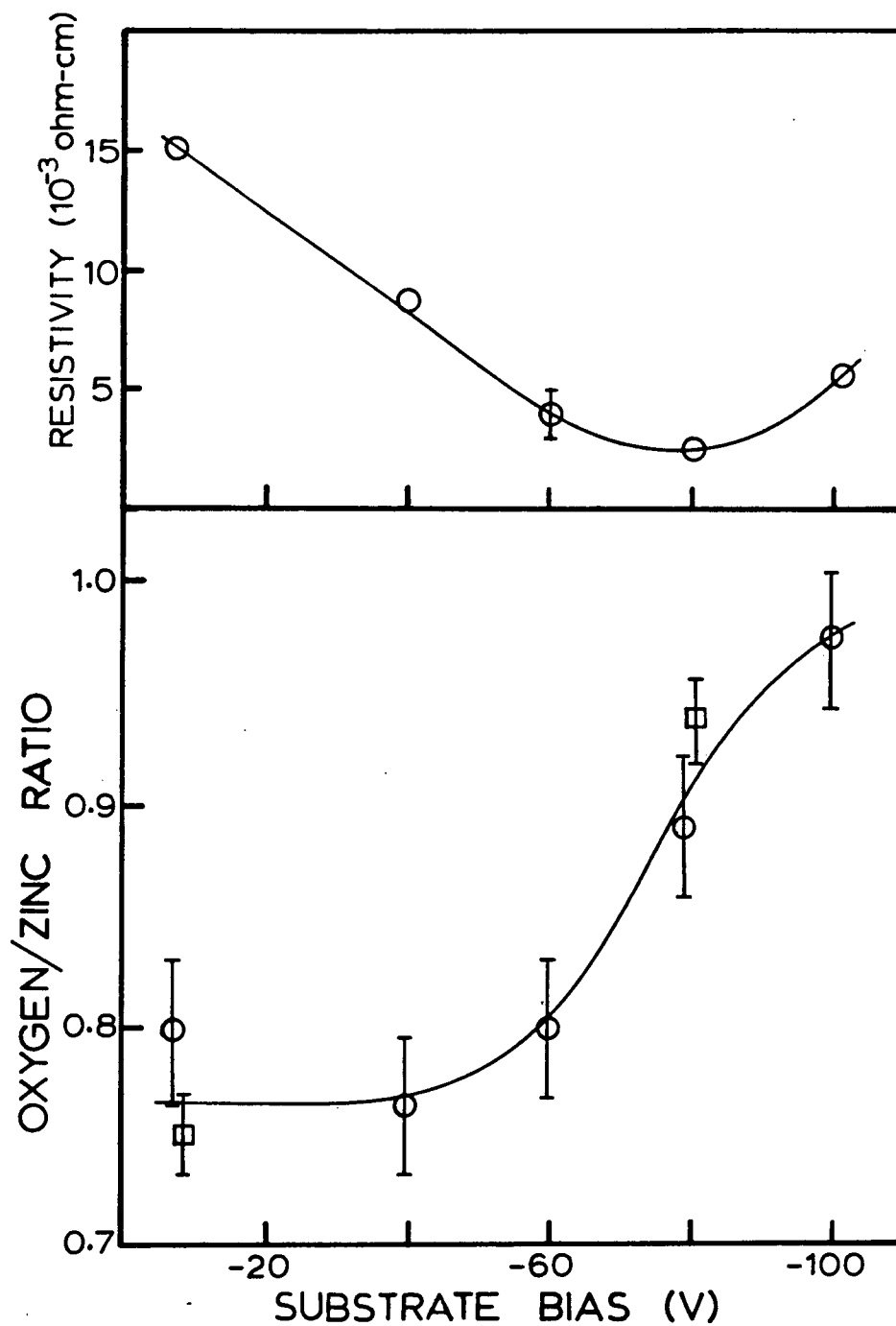


Figure 4.3

The composition of bias sputtered zinc oxide as determined by Rutherford Backscatter analysis. The resistivity measurements correspond to those films whose compositions are indicated by circles.

to have a significant effect on the composition of reactively ion plated ZnO films, increasing the oxygen content from $\text{ZnO}_{0.76}$ to nearly stoichiometric ZnO.

4.4 MATERIAL RE-EMISSION

The effect of substrate bias on deposition rate has been studied for several different oxygen flow rates as shown in Figure 4.4. All films were deposited for 20 minutes in the metallic operating mode at a target power of 150 W and a total sputtering gas pressure of 1.0 Pa. The partial pressure of oxygen in the vicinity of the substrate, $pp(\text{O}_2)$, is shown for each flow rate. The films deposited at $f(\text{O}_2)=0$ sccm are, of course, pure metallic zinc. It was previously mentioned that the Zn deposition rate at constant target power slowly decreases over the course of several experiments due to the clogging of holes in the baffle. These experiments were done in order of increasing $f(\text{O}_2)$ and the decrease in deposition rate of Zn is estimated not to exceed 15% during sputtering of the 24 films reported here.

A substantial decrease in thickness of the Zn metal films was observed as the substrate bias (and consequently total rf power) was increased. At high bias, the deposition rate is apparently near zero. Also with increasing bias, films at $f(\text{O}_2)=0.75$ sccm change in appearance from metallic black to almost clear, films at $f(\text{O}_2)=1.80$ sccm change from black to clear, and films at $f(\text{O}_2)=2.80$ sccm change from brown to clear. At -7 V bias, this is indicative of Zn excess in the

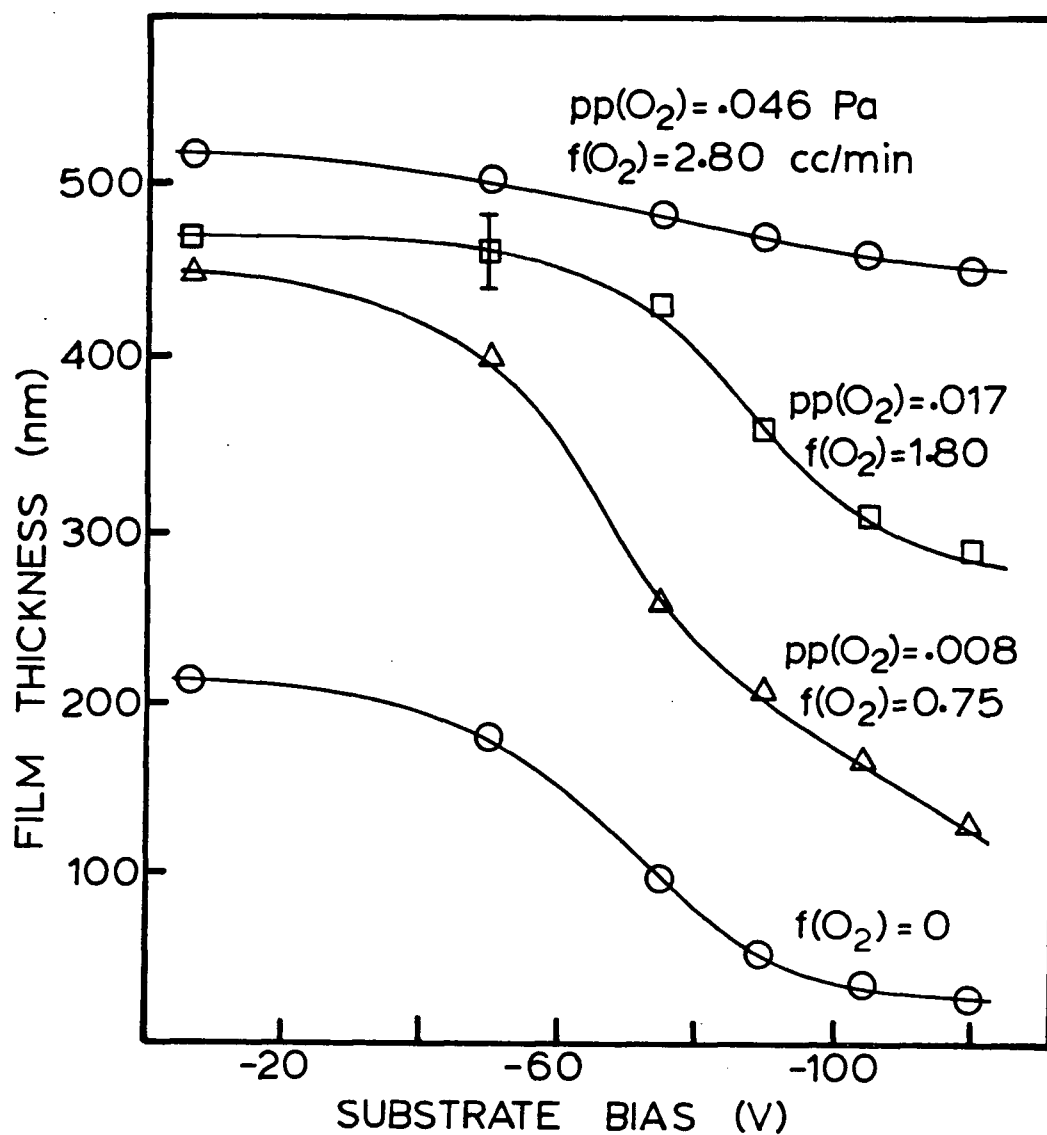


Figure 4.4

Evidence of preferential re-emission of excess zinc from growing films. All films were deposited at 150 W total power in the metallic operating mode for the various substrate bias and oxygen flow rates indicated.

films decreasing with increasing $f(O_2)$, whereas at high substrate bias all films (except Zn films) approach stoichiometric ZnO.

The observed material loss is confirmed by the report of Maniv [57] of an unexplained decrease in Zn deposition rate with increasing substrate discharge power during reactive planar magnetron sputtering of ZnO. Figure 3.2 showed that the reactive gas baffle prevented interactions between the rf and the dc plasmas, so that a change in conditions at the target due to the rf discharge is not the cause of the deposition rate decrease. Igasaki and Mitsuhashi [78] reported a small deposition rate decrease with bias during reactive ion plating of TiN films. They were able to attribute this decrease to the densification of films deposited at high bias. Such an explanation seems unlikely for the films of Figure 4.4 due to the doubling or tripling of film density that would be required. However, an experiment, described below, was conducted to test for densification effects in bias sputtered Zn films.

Zn films were sputtered onto glass substrates at various values of substrate bias. The glass substrates were carefully weighed with a Mettler H41 balance of resolution 10 μ gm before deposition, after deposition, and after etching off the Zn coating in HCl. Also after deposition, the film thicknesses were measured with a profilometer. Table 4.1 shows that the film thickness has a strong correlation with the film mass. The densities of all films, assuming homogeneity over 1x2 inch

Table 4.1 Mass measurement of bias sputtered Zn films.

Bias (V)	Thickness (μm)	Mass (mg)	Density (gm/cm^3)
-6	0.47 ± 0.02	3.21 ± 0.06	5.3 ± 0.3
-50	0.39	2.60	5.2
-60	0.29	1.93	5.2
-70	0.16	1.46	7.0 ± 1.2

substrates, compare reasonably well with the tabulated bulk figure of $7.1 \text{ gm}/\text{cm}^3$. The slight densification of the film at -70 V bias may in fact be due to less efficient material removal near the edges of the substrate.

The deposition rate decrease with bias is attributed not to a change of target discharge conditions or film density but to re-emission of material from the growing film. Zn rich films (low $f(\text{O}_2)$ or low bias) show a large material loss with increasing bias whereas stoichiometric ZnO (high $f(\text{O}_2)$ or high bias) is resistant to material loss. This phenomenon is interpreted as preferential emission of excess zinc.

4.5 ZINC RE-EMISSION BY EVAPORATION

Re-emission of zinc from a growing film could occur by two processes; resputtering or evaporation. In this section experiments are described in which the heating action of the substrate bias is measured, and then duplicated by a radiant heater in order to observe any evaporation effects independent of resputtering processes.

Substrate temperature measurements were made as close to

the surface of the growing film as possible. A thin Zn film (50 nm) of resistance $10\ \Omega$ was deposited in a four point probe pattern on a glass substrate. Contacts to 0.03 mm diameter wires were made with silver paint. The Zn film and contacts were coated with 100 nm of electrically insulating Al_2O_3 and then calibrated for temperature coefficient of resistance in an oven. Four point probe measurements of Zn resistivity during ZnO film deposition on top of the Zn/ Al_2O_3 structure enabled determination of the substrate surface temperature.

Figure 4.5 shows both the total rf power applied to the substrate and the film surface temperature as a function of the substrate self bias. A maximum film temperature near 400 K is observed at the high bias value of -120 V. These low temperatures are in general agreement with the results of Sundgren et al. [82] who reported a temperature of 420 K for uncooled substrates during reactive bias sputtering of TiC. Maniv et al. [57] report uncooled substrate temperatures not exceeding 373 K during reactive bias sputtering of ZnO. The self bias voltage developed on Maniv's substrate holder (-10 V) was less than the bias voltages used in my experiments.

The four point probe temperature results agreed to within 15 K with subsequent measurements made by attaching a 0.03 mm chromel-alumel thermocouple wire to the surface with silver paint. Successful deposition of ZnO coatings onto polyethylene plastic film, which softens significantly at 370 K, provided further proof of the low substrate

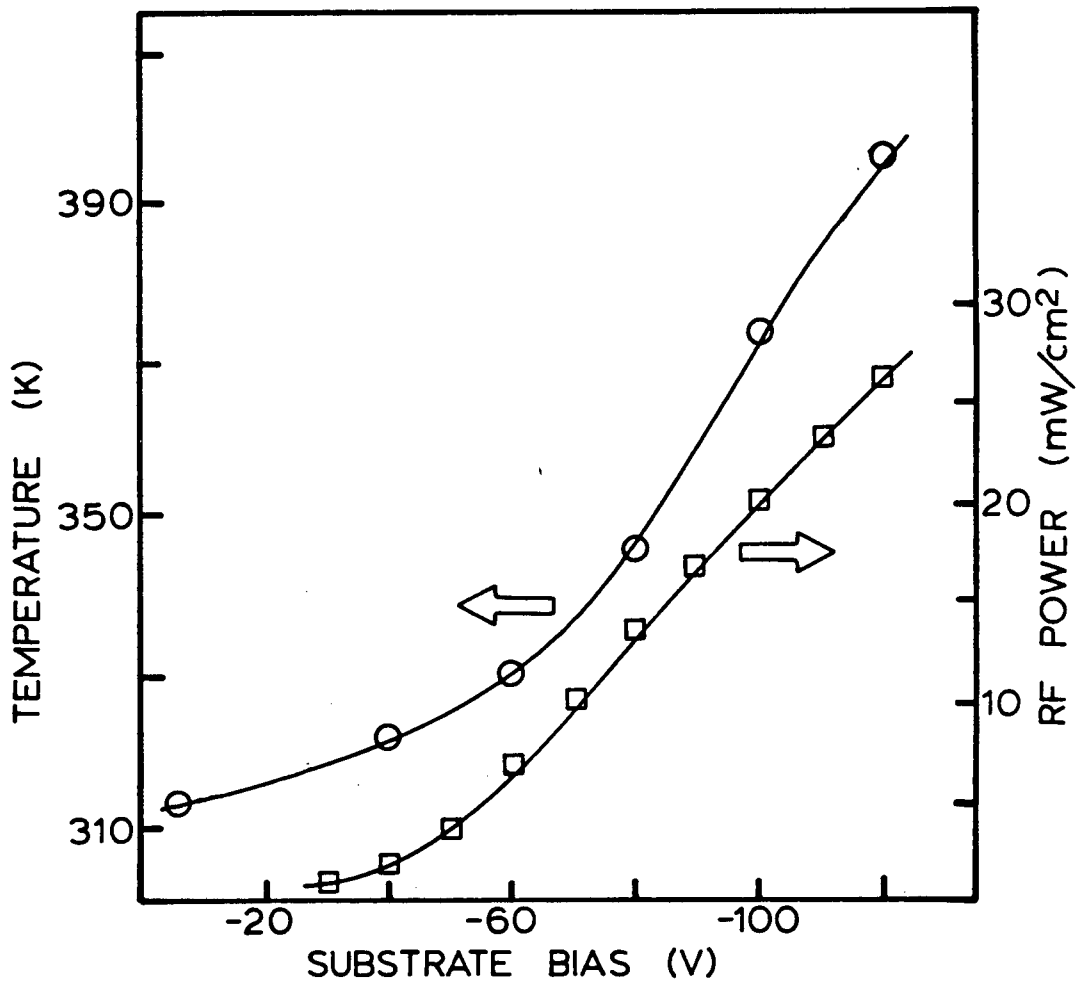


Figure 4.5

The substrate temperature and average rf power density at the substrate shown as a function of the applied substrate bias.

temperatures attained.

An estimate of substrate heating was found by summing heat flux contributions to the film and then assuming that cooling occurs only by a radiative process. There exist three major contributions to heating:

1. Atoms of sputtered Zn condensing on the substrate are expected to provide approximately 15eV/atom [83]. This corresponds to a power density of 100 W/m².
2. A typical rf power density, as seen in Figure 4.5, is 200 W/m².
3. The temperature of the Zn target surface was estimated at 403 K, using data from indium targets where the In surface melted (429 K) at slightly higher cathode powers than used for Zn. The radiative heat flux from the hot Zn target provides about 60 W/m² at the substrate.

Thus a generous estimate of total power density at the substrate for a -100 V bias is $J=360 \text{ W/m}^2$. For radiative cooling, the film surface will equilibrate at a temperature T given by;

$$J = \epsilon \sigma (T^4 - T_0^4) \quad (4.6)$$

where ϵ is the average film emissivity, σ is the Stefan-Boltzmann constant, and T_0 is the temperature of the chamber walls. The chamber walls are cooled and heat only slightly to about $T_0=315 \text{ K}$. For an emissivity $\epsilon=0.5$, a film temperature $T=387 \text{ K}$ is reached. This rough estimate of film surface temperature compares well with the experimental data.

At first consideration, these temperatures seem unlikely

to cause evaporation loss from the deposited film. A radiant heater behind the substrate was calibrated using the thermocouple and four point probe thermometers, and used to test for evaporation effects. ZnO films were deposited in the metallic mode ($f(O_2)=2.5$ sccm) with no substrate rf discharge but at temperatures corresponding to those induced by the bias. Figure 4.6 shows these results; film thicknesses plotted against temperature and the effective bias that would be required to produce such temperatures. Films deposited at low temperatures were brown in colour and became clear at high temperatures, indicating a transition from a Zn excess material to stoichiometric ZnO and a preferential loss of Zn similar to that of Figure 4.4. Also shown in Figure 4.6 are data points from films made in the target oxide coverage mode with subsequent high partial pressure of oxygen near the substrate. These films are transparent and showed negligible material loss.

Table 4.2 Comparison of re-emission rate from ZnO films with bulk Zn evaporation rate.

Temperature (K)	ZnO Re-emission (nm/min)	Bulk Zn Evaporation (nm/min)
340	5	
360	12	
380	18	0.0037
400		0.027
440		0.80
480		14

Consulting known evaporation rates for bulk zinc [84],

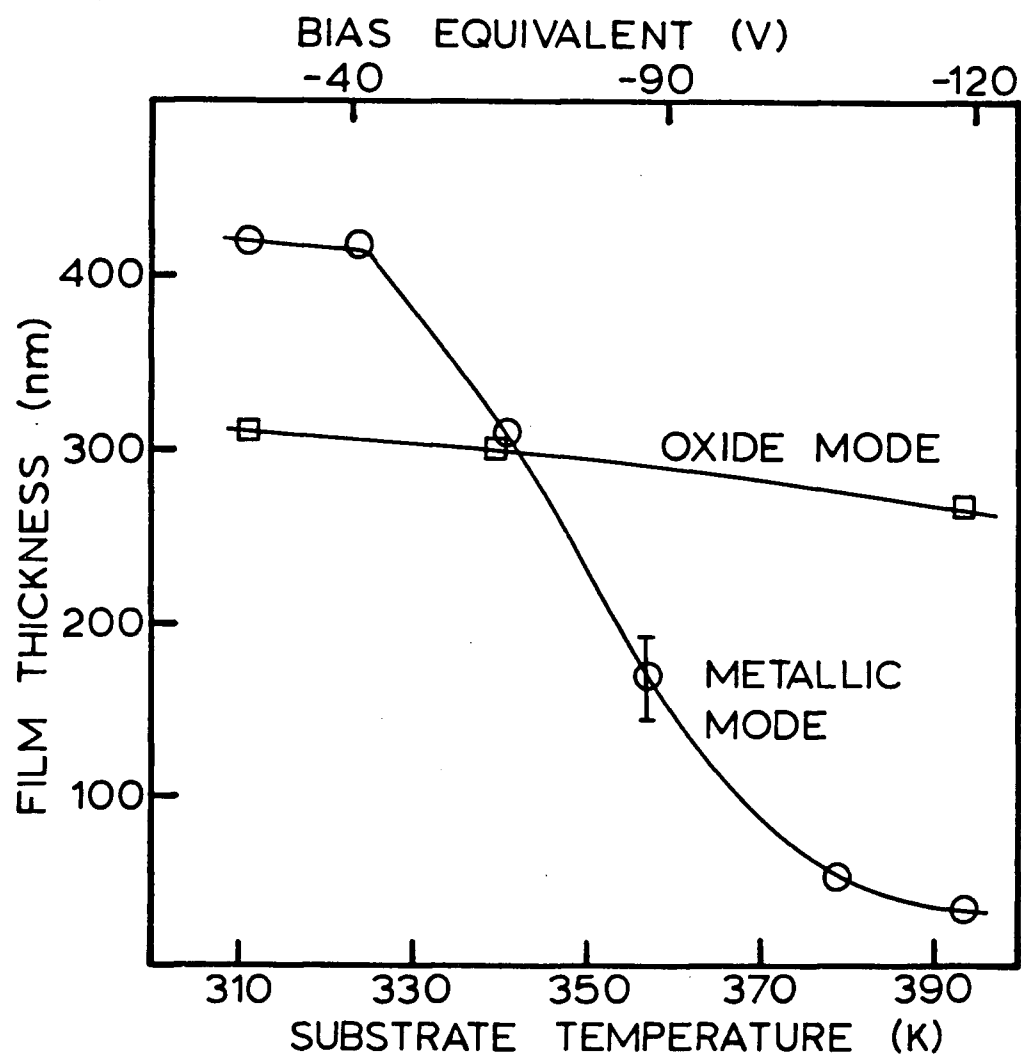


Figure 4.6

Evidence of material re-emission from zinc oxide films deposited in the metallic and oxide target modes. No substrate bias was applied, however the substrate was heated to temperatures equivalent to those induced by a substrate discharge.

Table 4.2 was constructed to compare the predicted bulk Zn evaporation loss with the experimental loss of material from ZnO films. The predicted bulk evaporation rate is seen to be more than 2 orders of magnitude less than that observed experimentally. These data are explained by proposing that adatoms of Zn are evaporated from the growing film before oxidation, and at an enhanced rate due to the weak bonding nature of such surface adatoms. Zinc atoms that are oxidized and become part of the bulk film will be stable and much less prone to evaporation. Consequently, a Zn excess material will show more Zn evaporation than stoichiometric ZnO. Similarly, under film growth conditions where zinc oxidation is rapid (high $p_p(O_2)$, oxide mode in Figure 4.6) there will be much less Zn loss than under growth conditions where oxidation of Zn adatoms occurs much more slowly (low $p_p(O_2)$, metallic mode of Figure 4.6). Notice that the loss of material of the heated ZnO film (Figure 4.6, metallic mode) is somewhat larger than that of the bias equivalent ZnO at about $f(O_2)=2.5$ sccm in Figure 4.4. This difference in material re-emission rate is associated with an oxygen ion plating and activation effect that will be discussed in section 4.7.

4.6 ZINC RE-EMISSION BY SPUTTERING

To independently identify any effects of resputtering, substrates were cooled to eliminate evaporation processes. Cooling was accomplished by bonding the glass substrate with silver epoxy to a water cooled copper plate. Subsequent temperature measurements in the cooled mode showed that the substrate surface did not exceed 313 K at the rf power levels used.

Figure 4.7 shows the thickness dependence on substrate bias for pure Zn films sputtered on both cooled and uncooled substrates at a target power of 150 W for deposition times of 30 minutes. Substrate cooling is seen to reduce the Zn re-emission loss, providing further evidence of the evaporation process. Figure 4.8 shows the results of an identical experiment on ZnO films produced in the metallic mode at target power 150 W with $f(\text{O}_2)=2.35$ sccm. ZnO films at low substrate bias voltages were black whereas those at high bias were clear, indicative of a relative increase in the oxygen content with bias. I ascribe the material loss on the cooled films to preferential resputtering of zinc and the added material loss on the uncooled films to evaporation.

A further experiment was performed to compare these observed resputter rates with sputter rates expected from bulk zinc and bulk ZnO. A series of four black ZnO films were sputtered under identical conditions with no substrate bias applied. After deposition of all films, one film (#3) was exposed to a substrate discharge of -175 V bias for 120

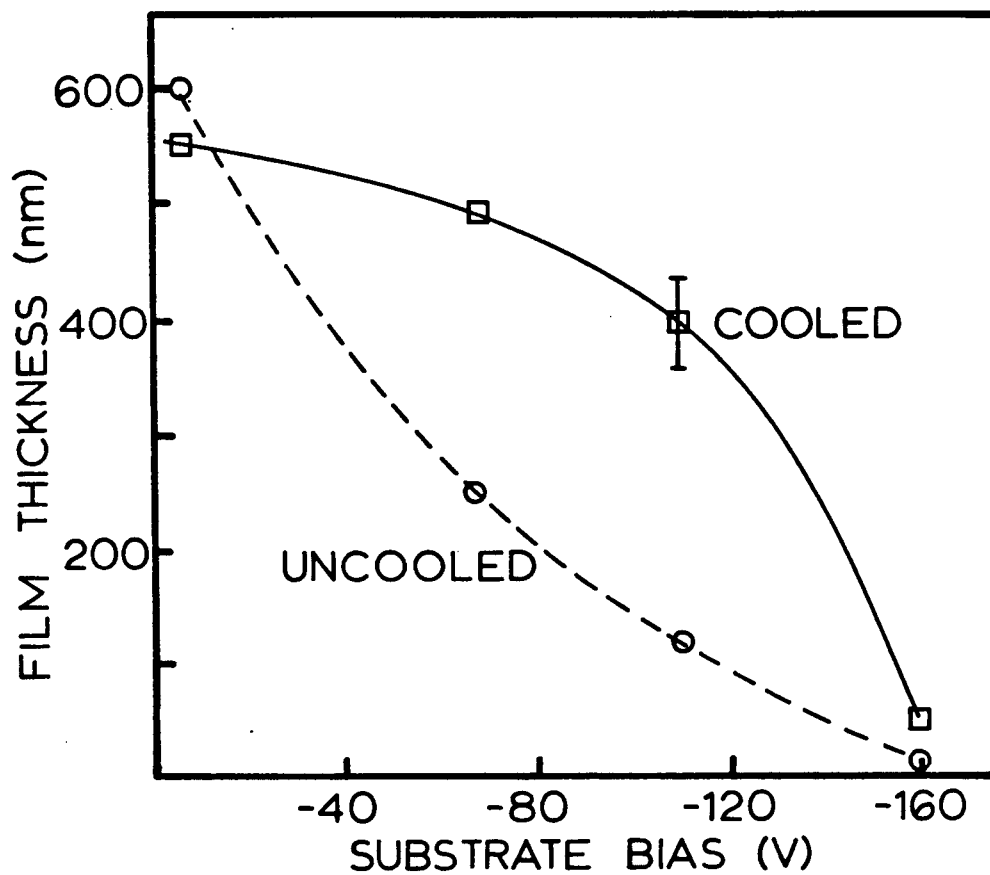


Figure 4.7

Evidence of re-emission from bias sputtered Zn films. Film thicknesses are shown for films deposited on both cooled and uncooled substrates.

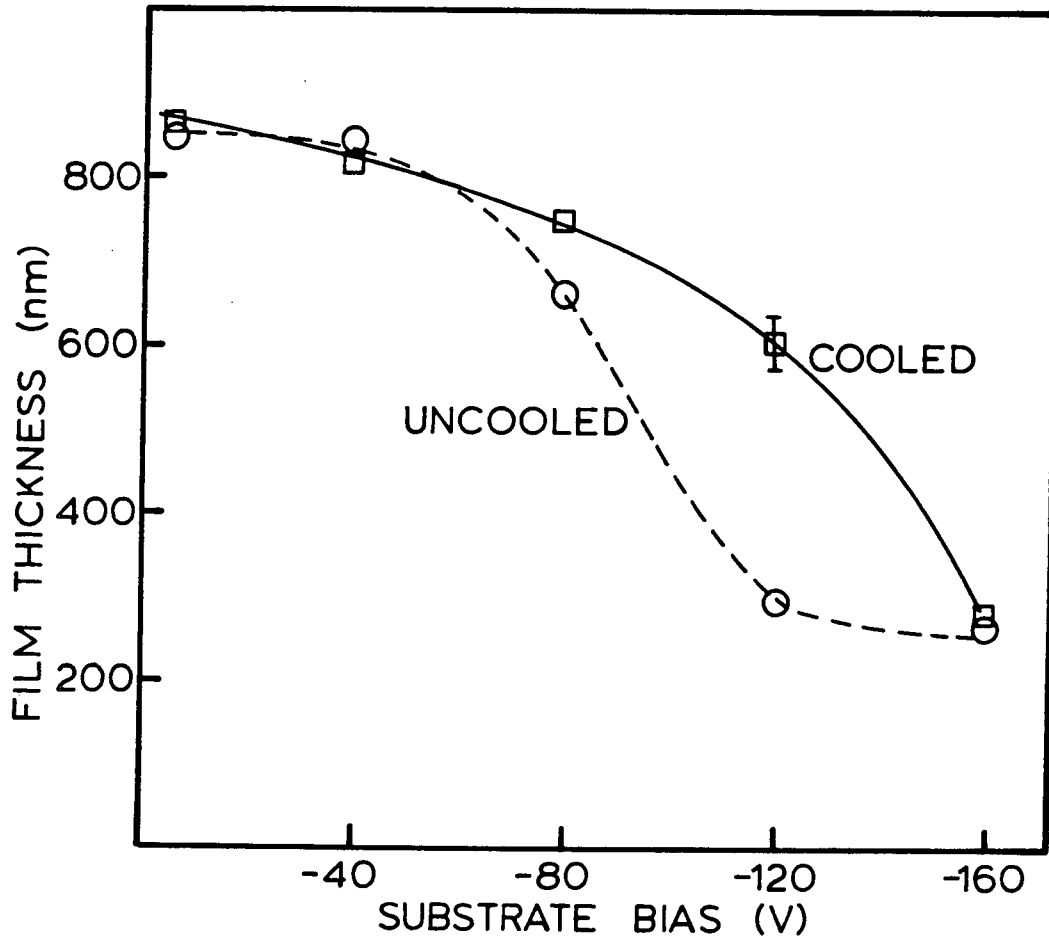


Figure 4.8

Evidence of re-emission from ZnO films bias sputtered in the metallic target mode. Film thicknesses are shown for films deposited on both cooled and uncooled substrates.

Table 4.3 Resputter of ZnO films after deposition.

ZnO Film	Resputter After Deposition	Thickness (μm)
1	no	0.27 ± 0.02
2	no	0.26
3	-175 V	0.17
4	no	0.27

minutes. Table 4.3 shows the resulting thicknesses of each film. From the material loss of film #3, a resputter rate was determined. A similar experiment was performed where a pure Zn film was resputtered at -175 V bias after deposition. From these data, an average sputter yield for bulk Zn and bulk ZnO was calculated using the rf plasma characteristics of section 4.1. Due to the distribution of bombarding ion energies and the dramatic decrease of sputter yield for energies below 50 eV, this calculated yield is a very conservative estimate of the true yield at full bias energy.

The resputter results are summarized in Table 4.4. The sputter yields for Zn and ZnO during deposition were calculated from Figures 4.7 and 4.8. I was unable to find tabulated data for the low energy sputter yield of Zn or ZnO, however a value of 0.8 at 175 V is typical for a high yield metal such as Zn [85]. The observed resputter yield during deposition is much larger than that measured for bulk ZnO or bulk Zn after deposition and also larger than the 'tabulated value'. Consistent with the explanation of the evaporation process, it is proposed that the growing film displays an

Table 4.4 Resputter yields of Zn and ZnO films.

Film	Conditions	Bias (V)	Resputter Rate (nm/min)	Yield
Zn	resputter after	-175	2	0.3
ZnO	deposition	-175	0.8	0.1
Zn	resputter during	-160	17	3.0
ZnO	deposition	-160	20	2.6

enhanced sputter yield for unoxidized zinc adatoms.

4.7 OXYGEN ACTIVATION AND PLATING

The rf discharge surrounding the substrate induces bombardment by energetic ions of Ar^+ , O_2^+ , and O^+ (ion plating) and will create excited and atomic oxygen species through collision processes (oxygen activation). Teer [86] has shown that a large amount of the energy in a glow discharge is dissipated by energetic neutrals. To determine if plating and activation are significant in stoichiometry control, I have chosen a substrate geometry that will minimize the processes of resputtering and evaporation.

An rf discharge was applied to a fine mesh screen placed 1.5 cm in front of the electrically isolated glass substrate. In this mode, energetic bombardment of the substrate was reduced and most heat dissipated at the screen. However, due to the proximity of the substrate to the screen discharge, the substrate would still be subjected to lower energy neutral and ion bombardment, low energy electron bombardment, and exposed

to a plethora of activated species. This geometry is similar to that of Morgan et al. [14], who evaporated Zn through an oxygen gas discharge in order to enhance the growth of ZnO at the substrate.

A Zn film sputtered in pure Ar at various values of screen self bias provided a sensitive test of the magnitude of resputtering and evaporation effects. Figure 4.9 shows that no measurable Zn re-emission occurred. However, reactive sputtering of ZnO in the metallic mode with the screen discharge still exhibited a change in film appearance from dark brown to very light brown and a decrease in film resistivity as the screen bias was increased (Figure 4.9). No ZnO material loss was observed. Notice that the lowest resistivity achieved is somewhat higher than that attained with the rf discharge at the substrate (Figure 4.3).

I conclude that oxygen activation and/or ion plating are significant in controlling ZnO film stoichiometry by enhancing the oxidation of sputtered zinc. At present, the relative importance of plating and activation processes is difficult to distinguish. The stoichiometry change inferred from the results of Figure 4.9 (where ion plating of the substrate is reduced) indicates that plasma activation processes such as energetic neutral bombardment assist film oxidation. The ion plating contribution to oxidation may be evaluated more precisely. The oxygen ion current to the substrate was estimated from the rf plasma characteristics discussed in section 4.1. The total ion current in the discharge at -100 V

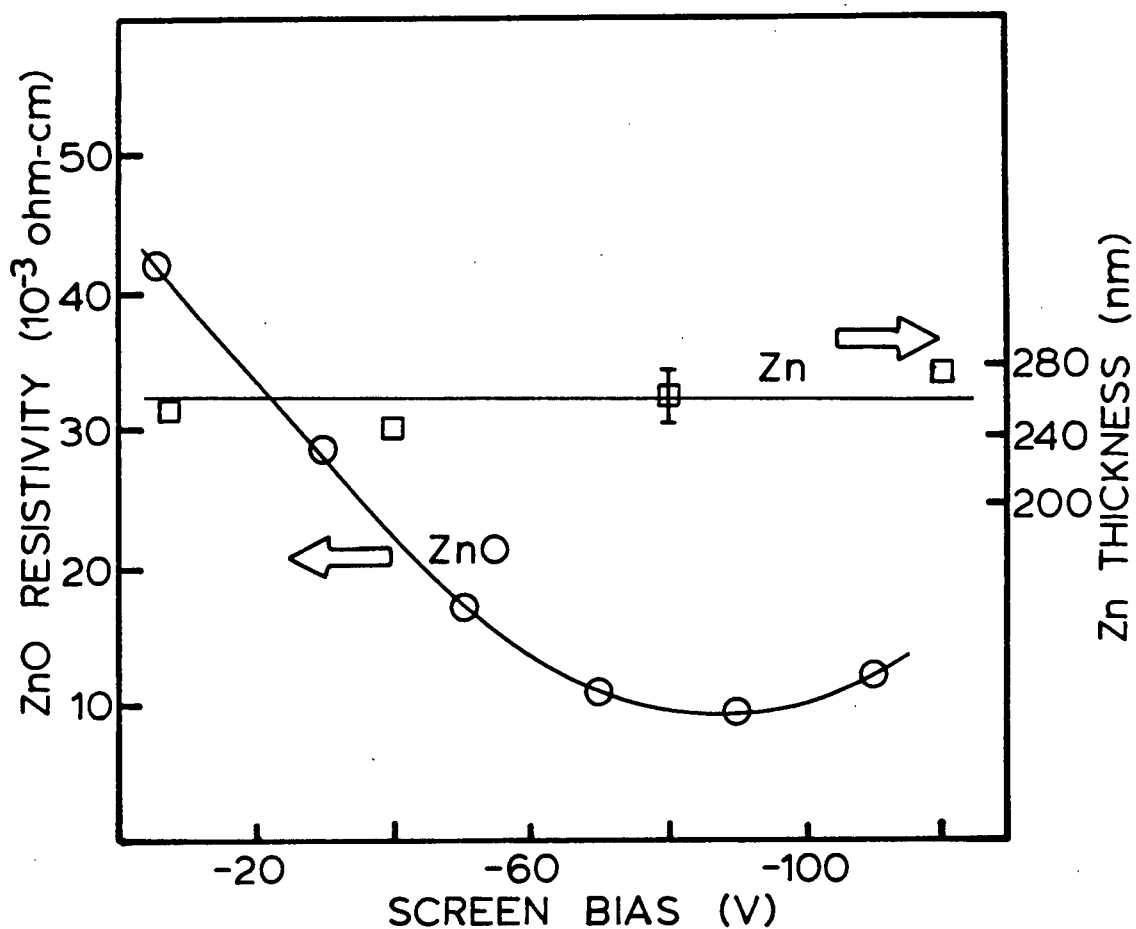


Figure 4.9

Results from application of an rf discharge to a screen in front of the substrate. Film thicknesses for Zn films and resistivity for ZnO films deposited in the metallic target mode are shown as a function of screen bias.

bias was found to be $J = 3 \times 10^{14}$ ions/cm²s. If the number of oxygen ions created is proportional to the oxygen partial pressure, then $J(\text{O}_2) = 1.5 \times 10^{13}$ ions/cm²s. Hecq. et al. [87] have shown that oxygen ionizes preferentially in high pressure Ar/O₂ discharges, but the effect is not significant at the low pressures used in this investigation. The ratio of the rate of arrival of Zn atoms to oxygen molecules (due to $p(\text{O}_2) = 0.05$ Pa) and to oxygen ions (due to the ion current) is estimated as 1:65:0.01 respectively. This ratio demonstrates two important points. First, the sticking coefficient of molecular oxygen on zinc is not large (about 0.015). Second, for the ion plating mechanism to be significant, the sticking coefficient of bombarding oxygen ions should be much larger than that of free oxygen molecules. This is likely the case, since near energies 50 eV or greater, ions will be implanted into the growing film [88]. Assuming a unity sticking coefficient for oxygen ions, the resultant increase in oxygen content of the film would be about 2%.

Additional evidence for the activation/plating mechanisms was provided in Figure 4.6, where heated ZnO showed a surprisingly large material loss compared to that expected from a substrate discharge. The heated ZnO was lacking activation/plating processes during growth that would have enhanced the formation of stable oxide and resisted further material loss.

4.8 SUMMARY AND DISCUSSION

Resputter processes at the substrate have been observed and modelled by a number of researchers, most recently by Barnett and Greene for GaAs deposition [89], and by Dove et al. for metal alloy films [76]. None of these models required enhancement factors due to unexpectedly large resputter yields and, evaporation mechanisms were not explicitly considered. In other work, resputter processes have been attributed to substrate bombardment by neutrals and negative ions produced at the target [90,91,92]. Such bombardment is unlikely in my experiments since the target to substrate separation of about 10 mean free path lengths ensured that energetic species from the target would thermalize before reaching the substrate. Also, the observed resputter variation with bias is opposite to that expected for negative ion bombardment. In reactive bias sputtering by Poitevin et al. [79] and by Igasaki and Mitsuhashi [78], no change in stoichiometry of TiN films resulted from variations in the substrate bias, and no material re-emission was observed. Reactive bias sputtering of TiC by Sundgren et al. [82] showed an increase in carbon content of the films as the bias was varied from -200 V to 0 V. This was attributed to ion plating of CH_4 molecules.

Murti has rf sputtered transparent ZnO films from a zinc oxide target [138]. With increasing substrate bias, he observed a change in film resistivity from $10^4 \Omega\text{cm}$ to $10^{-1} \Omega\text{cm}$ and attributed this effect to preferential resputtering of oxygen from the film, in apparent contradiction to my results.

However, in Murti's work, the bias voltage on the substrate holder was obtained by means of a voltage divider network from the same power supply used to supply the target voltage. Consequently, as the bias voltage was increased, the voltage at the target and the film deposition rate decreased. Such a change in film deposition rate confuses the interpretation of results by altering the arrival rate of Zn and O species at the substrate. Furthermore, extensive studies of reduction at oxide surfaces by Kim et al. [139] have shown that ZnO is not reduced by Ar⁺ ion bombardment.

The results of Jones et al. [93] are most relevant to my work on ZnO. During deposition of SiO₂ by sputtering, high material re-emission coefficients of up to 0.85 were observed. Substrate temperatures (623 K) and rf power density (4 W/m²) were significantly higher than those used here for ZnO. Re-emission coefficients were found to be an increasing function of substrate temperature and bias and were explained by a model of evaporation and resputtering of loosely bound surface atoms. I have adopted this model to explain the observed loss of Zn at low temperatures and bombardment energies. A notable similarity of Si and Zn is that both materials oxidize very slowly, as judged by formation times of oxide monolayers on clean metal [94,95]. Thus adatoms may remain unattached and mobile on a growing film for longer periods of time, leading to a greater probability of emission.

Other pertinent characteristics of Zn are its low melting point (693 K) and very high vapour pressure (10^{-8} torr at

400 K) due in part to the weak Zn-Zn bond strength of 0.3 eV. This is the lowest bond strength of any metal except Hg. For comparison, the vapour pressure of tin (melting point 505 K and bond strength 2 eV) is 12 orders of magnitude lower than Zn [96]. Weakly bonded surface monomers or dimers of Zn should exhibit even larger vapour pressures and effectively higher emission probabilities. However, when oxidized, Zn is strongly bound to oxygen (2.8 eV bond strength), has a negligible vapour pressure and a higher bulk sputtering yield.

In further work by Jones et al. [97] it was observed that re-emission was essential to obtain films of best quality, as judged by the pin-hole breakup thickness phenomenon, which is a test of resistance to erosion by acid. This increase in film quality was suggested by Jones to be due to re-emission of atoms in non-optimum positions that would otherwise be trapped by further deposits to form defected material. Analogous to this result, I note that the best ZnO films, as judged by lowest resistivity, were not made by stoichiometry control with only the oxygen plating/activation mechanism (Figure 4.9) but by a substrate discharge that also caused Zn material loss. Re-emission effects may optimize electrical properties by removing impurities such as carbon (as observed in RBS measurements) or implanted Ar. Winters and Kay [98] have observed that the concentration of implanted Ar is minimized for substrate biases near -90 V.

If the anomalous properties of Zn such as bond strength and vapour pressure are the fundamental reasons for the

observed enhanced re-emission phenomena, then a metal with large bond strengths, low vapour pressure and a known affinity for oxygen should not exhibit re-emission during reactive bias sputtering. Titanium was chosen as a representative metal of this class. Ti has a bond strength of 1.5 eV, a vapour pressure more than 14 orders of magnitude lower than Zn, and is used extensively as a getter pump for oxygen [99].

Table 4.5 Thicknesses of bias sputtered TiO₂ films.

Bias (V)	Thickness (μm)
-7	0.39 \pm .03
-66	0.42
-100	0.43
-125	0.40
-150	0.39
-175	0.39

A Ti metal target was reactively sputtered in an Ar/O₂ discharge, and films with a slight oxygen deficiency (sub-stoichiometric TiO₂) were deposited in the metallic target mode at various values of substrate bias. Table 4.5 shows the resulting thicknesses of films deposited at 400 W target power. No material loss was observed for a bias up to -175 V, which exceeds the substrate bias values normally used to produce ZnO films. The TiO₂ films were visually dark blue, indicative of a Ti excess [140]. A decrease of this visual absorption with increasing bias was attributed to a reduction of the Ti excess through ion plating of oxygen.

It has been pointed out by Koenig and Maissel [66] that

resputtering of a film during deposition is dependent on the division of applied rf voltage between the darkspaces of the substrate and the ground (chamber) electrode. As pointed out in section 4.1, this division is dependent on the relative areas of the electrodes. I have shown that substrate bias and temperature not exceeding -100 V and 370 K, respectively, allow oxidation control and cause some beneficial material removal but do not reduce deposition rates to inefficient levels. Consideration of these effects becomes critically important when designing sputter systems for reactive bias sputter deposition of ZnO. It may be necessary to tailor substrate geometry and cooling in order to obtain the desired bias, temperature and current density characteristics, subsequently optimizing resputtering, evaporation and oxygen activation effects.

In summary, I have shown that the effect of the substrate discharge is to enhance the oxygen content of the growing film. This occurs by preferential evaporation and resputtering of zinc and by oxygen ion plating and activation. The resputtering and evaporation processes were found to be significantly enhanced over that expected for bulk Zn, due to the weak bonding nature of unoxidized Zn atoms. In light of this understanding of the deposition process and a knowledge of film stoichiometry, the following chapter describes the full characterization of optical, electrical and structural properties of bias sputtered ZnO films.

CHAPTER FIVE: ZnO FILM CHARACTERIZATION

5.1 FILM DEGRADATION

A typical experiment to test for the ageing or weatherability of a heat mirror film is to expose the film to high temperatures (370 K) and humidity while irradiating the film with intense ultraviolet radiation [100]. Such tests are believed to simulate normal use degradation properties, but at an accelerated rate. To give some indication of the stability of sputtered ZnO film properties, a very simple experiment was designed as follows.

A small oven was maintained at a temperature of 365 K and approximately 90% relative humidity. Two identical ZnO samples of good conductivity were deposited on glass substrates. One film was kept as a control at room temperature and humidity, whereas the other was kept in the oven for a period of 40 days. Measurements of film resistivity and infrared reflectivity were made at periodic intervals for both samples. No measurable change in properties of the control film was observed after the 40 day interval. However, Figures 5.1 and 5.2 show significant changes in resistivity and infrared reflectivity of the heated film. The increase in film resistivity corresponded to a decrease in the infrared reflectivity. Also, the heated film was less transparent due to a cloudy or milky appearance and, in some regions of the film small flakes of ZnO had separated from the substrate and could be blown away.

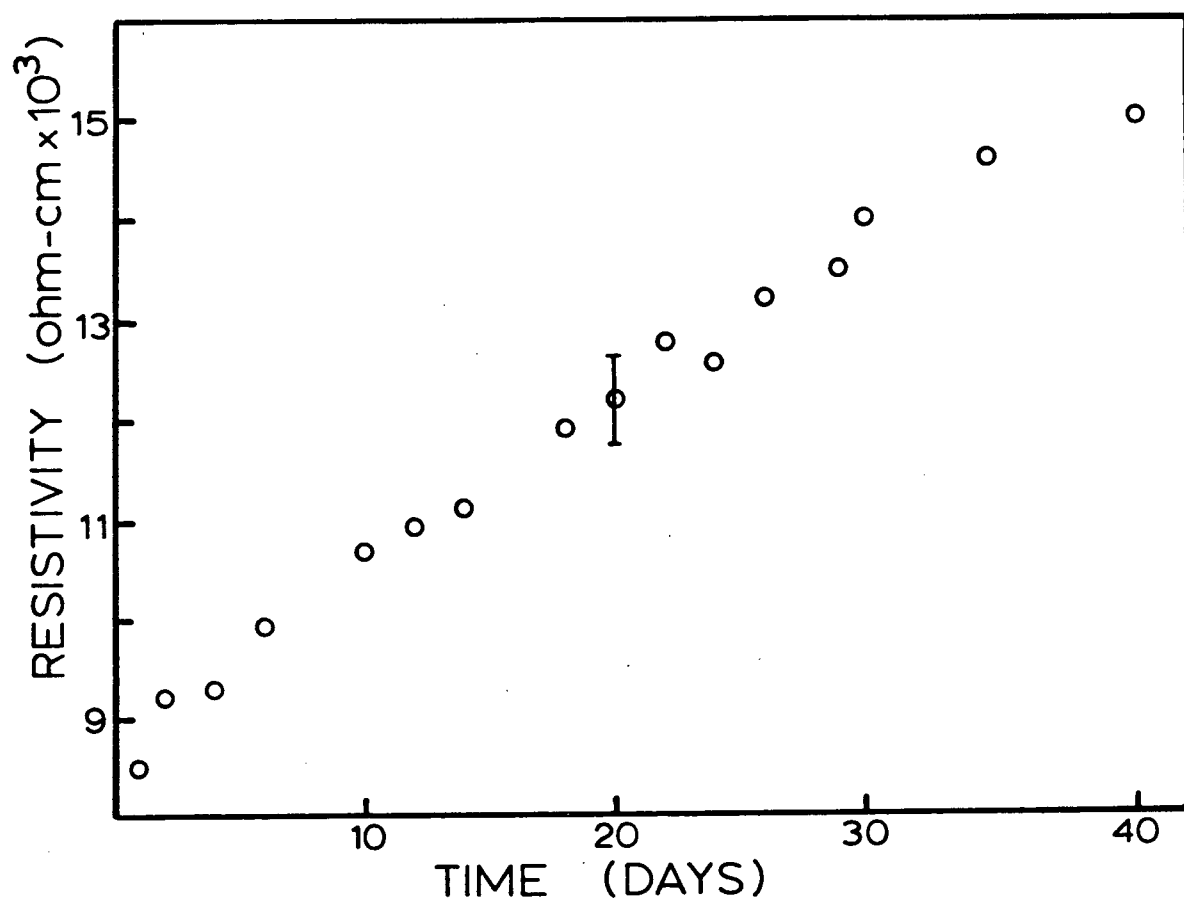


Figure 5.1

Degradation of resistivity for a ZnO film maintained at 95°C and 90% relative humidity.

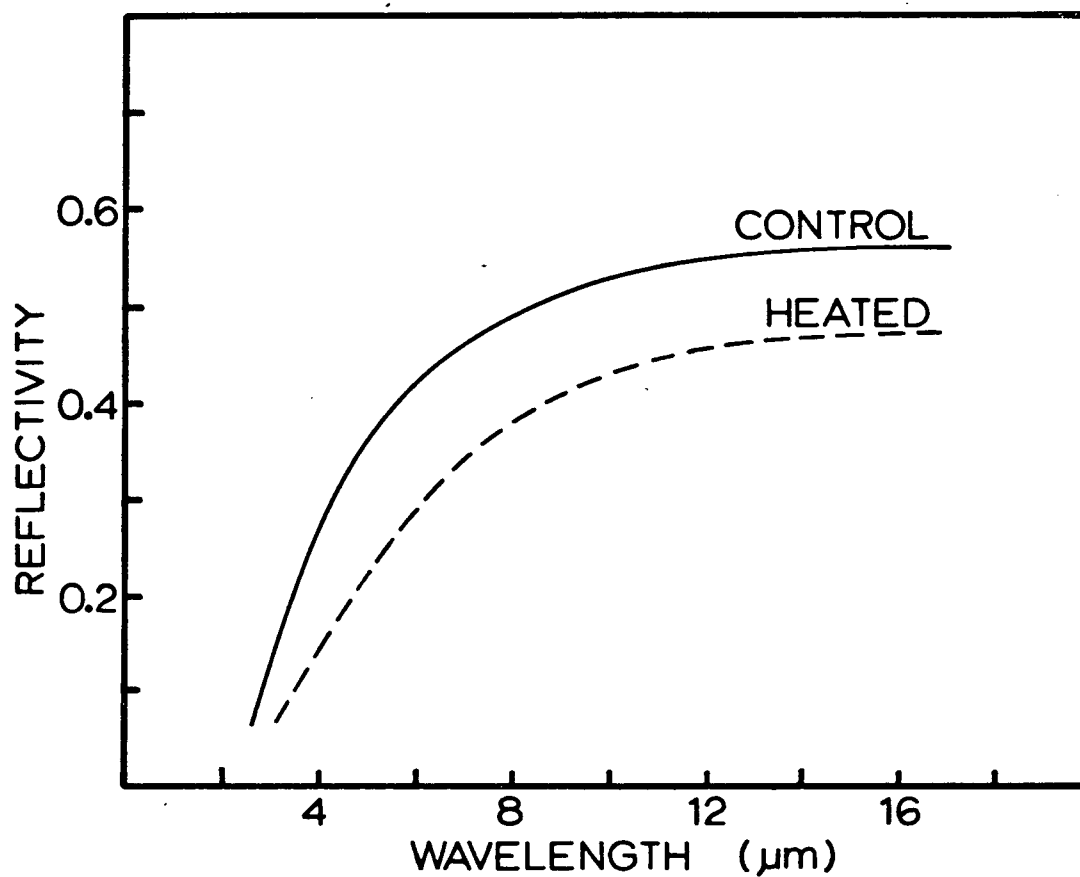


Figure 5.2

Infrared reflection characteristics of a ZnO film before and after a 40 day exposure to a temperature of 95°C and a relative humidity of 90%.

The degradation effects in the hot, humid environment may be due to further oxidation of the ZnO film (increasing the resistivity) and by the attack of water vapour (possibly slightly acidic) at the grain boundaries of the coating. Maniv et al. [57] and Hickernell [101] have reported very rapid etch rates for ZnO in weak acid. Work by Minami et al. [102] compared the changes in conductivity of ZnO and ITO transparent conductors due to high temperature exposure. ITO was resistant to change for temperatures up to 700 K, but ZnO films showed an increase in resistivity even after brief (10 minute) exposure to temperatures exceeding 470 K.

From my experiment it is certainly not possible to predict the lifetime of a ZnO heat mirror or transparent electrode in normal use. However, conducting ZnO does not appear promising as a stable coating for long term use. Film degradation may be inevitable as the conduction properties rely on non-stoichiometry through oxygen deficiency. In comparison, good quality stoichiometric ZnO films for acoustic transducer applications are known to exhibit very stable film properties [101].

5.2 FILM STRUCTURE

The microstructure of bias sputtered ZnO films is modified by the effects of both energetic ion bombardment and by stoichiometry change. To gain an independent understanding of each effect, X-ray diffraction measurements were made on bias sputtered zinc films (no stoichiometry change) and on ZnO

films sputtered at various $f(\text{O}_2)$ without substrate bias (no bombardment effects). This study has enabled a qualitative analysis of the bias induced structure modification in ZnO films.

ZnO films were sputtered in the metallic target mode on glass substrates at various values of oxygen flow $f(\text{O}_2)$. Figure 5.3 shows the hexagonal wurtzite X-ray diffraction spectrum for each film, using 0.154 nm Cu-K α radiation. Structures in the diffraction spectra were not observed outside of the given angle range, with the occasional exception of a broad peak at $2\theta=72.7^\circ$, characteristic of the ZnO 004 line. Zn excess films at low $f(\text{O}_2)$ display broad diffraction peaks of low intensities, indicative of a microcrystalline or near amorphous material. No peaks due to metallic Zn were identified, presumably due to the large disorder in the films and the greater volume fraction of ZnO. A similar lack of metal diffraction peaks in non-stoichiometric films was observed by Affinito et al. [103] for Al/AlN composites at volume fractions of Al up to 0.45.

At high $f(\text{O}_2)$, the nearly stoichiometric ZnO films have a good crystal structure with a strongly preferred orientation of the c-axis perpendicular to the substrate. A significant lattice strain of 0.8% is seen, indicated by the shift of the 002 peak to 34.20° from its unstrained value of 34.47° . Such strain and a preferred basal orientation are typically observed in sputtered ZnO coatings [104,105].

Some of the common effects noticed in sputtered elemental

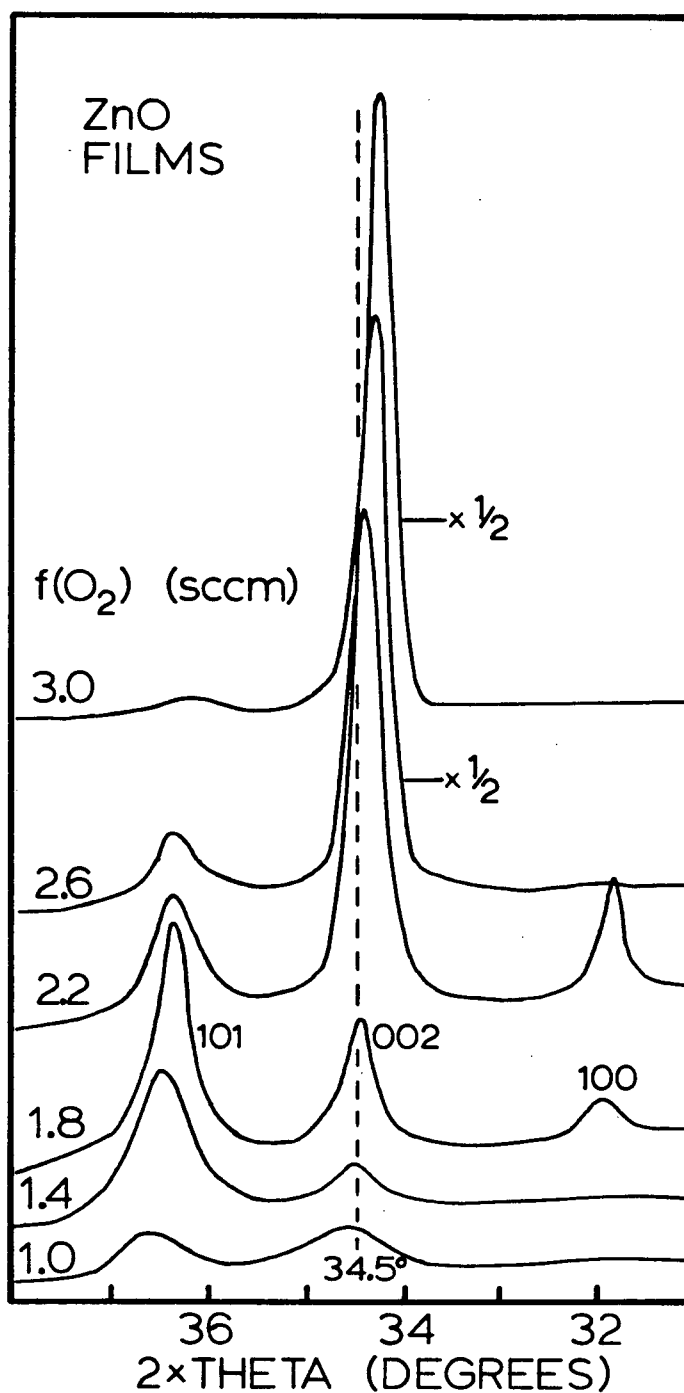


Figure 5.3

X-ray diffraction spectra of zinc oxide films deposited at various values of oxygen flow rate. With increasing $f(\text{O}_2)$, the composition of the films approach stoichiometric ZnO. A substrate discharge was not used during deposition.

films as the substrate bias is increased are film densification, a large decrease in crystallite size and a significant disruption of the morphology and crystal orientation [106,107]. These effects are believed to be due in part to a sputter redistribution of film material [108]. In Figure 5.4, X-ray diffraction spectra are shown for Zn films sputtered in an Ar discharge at 1 Pa total pressure and at various values of substrate bias. Zn crystallizes in a hexagonal closest packed form. Films at high bias were sputtered for longer time periods such that all film thicknesses agree to within 20%. Even a low bias of -50 V is seen to cause a dramatic decrease in crystallinity of the film and a change from a preferred basal orientation of crystallites to a more random orientation.

Two important effects of substrate bias on film microstructure have been observed in the previous two experiments. First, a reduction of Zn excess in the films leads to oriented polycrystalline films showing large strain whereas energetic ion bombardment reduces and randomizes film crystallinity. Both effects must be included to explain the microstructure of bias sputtered ZnO shown in Figure 5.5. These films were sputtered from the standard metallic target mode at total pressure 1 Pa and at $f(O_2)=2.5$ sccm. The optical and electrical characteristics are similar to those reported in Figure 2.6. Films at -6 V and -40 V bias are visually dark with a Zn excess. Films at higher bias are transparent and good conductors. The film at -6 V bias (no rf

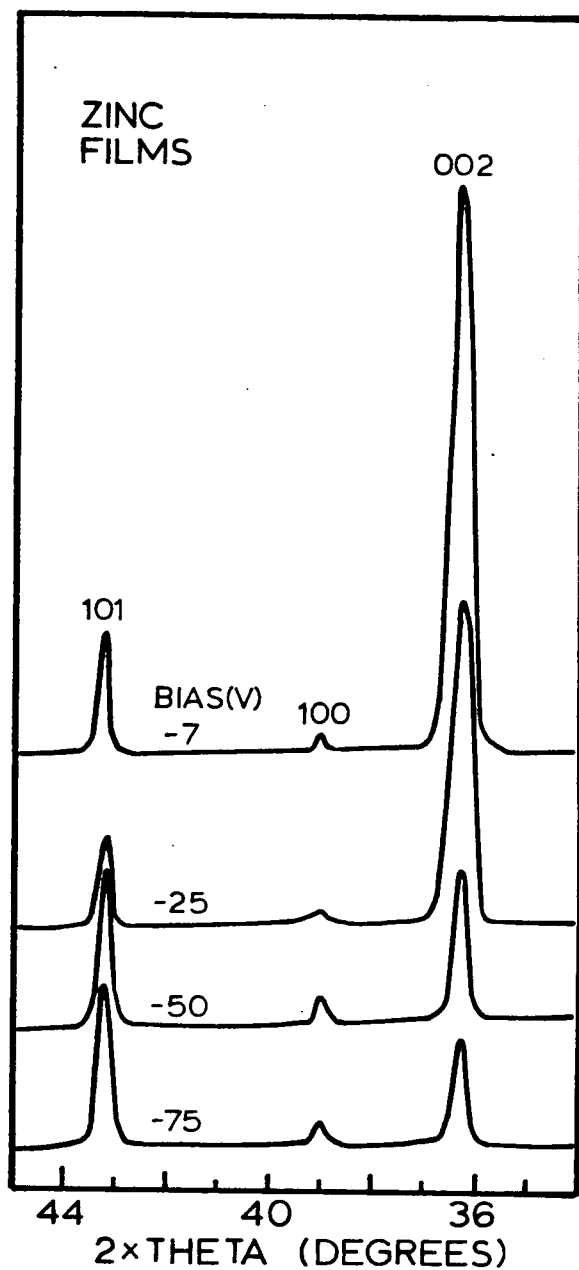


Figure 5.4

X-ray diffraction spectra of bias sputtered Zn films. Deposition times were chosen such that all films were of thickness $0.65 \mu\text{m}$.

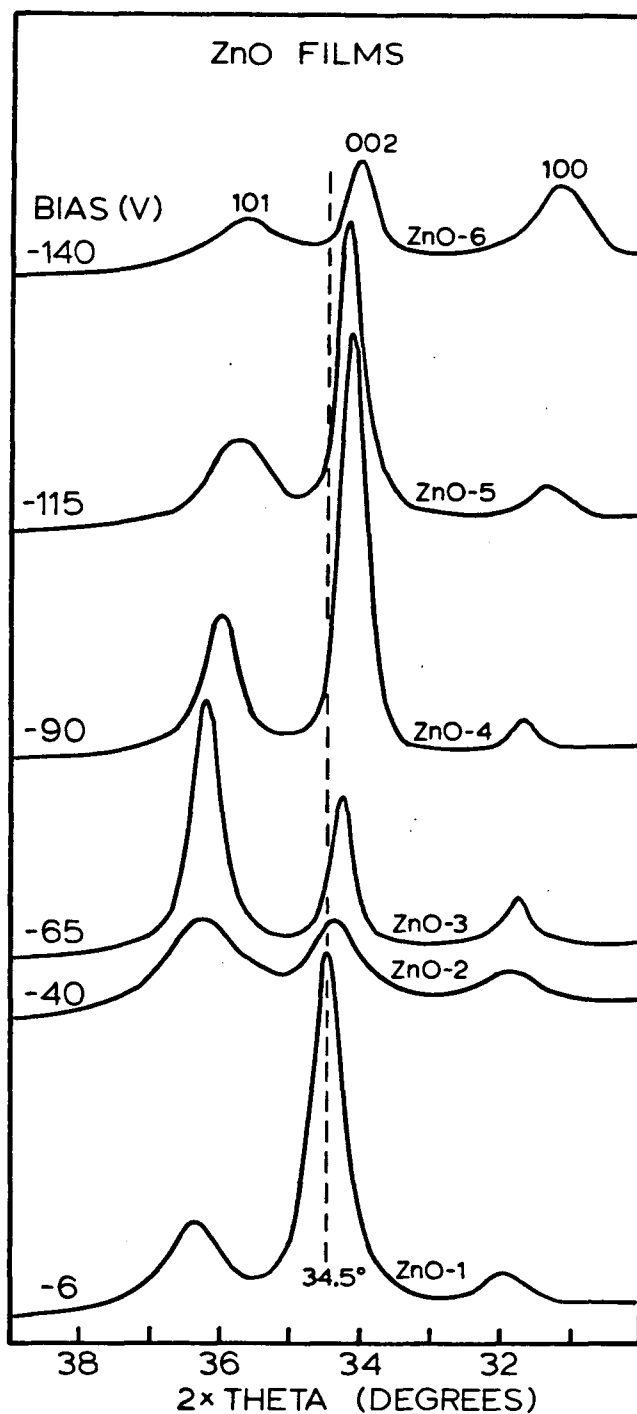


Figure 5.5

X-ray diffraction spectra of bias sputtered zinc oxide films. Electrical and optical characterization of these films are detailed in Table 5.2 and Figure 5.11 respectively.

power) is an unstrained Zn excess material similar to those seen in Figure 5.3. At -40 V bias, little stoichiometry change has occurred, and bombardment induced randomization has degraded the orientation and crystallinity of the film. For films at -65 V and -90 V, rapid improvements in stoichiometry (see RBS results of Figure 4.3) overwhelm bombardment induced disorder and a diffraction pattern indicative of a well oriented, highly strained, near stoichiometric film is seen. For even higher bias, the stoichiometry cannot improve further, and the effects of ion bombardment are prevalent again, producing a reduction in crystallinity.

Table 5.1 Grain size of bias sputtered ZnO films.

Sample	Bias (V)	Grain Size (nm)
ZnO-1	-6	36
ZnO-2	-40	23
ZnO-3	-65	52
ZnO-4	-90	42
ZnO-5	-115	43
ZnO-6	-140	39

This qualitative explanation of ZnO diffraction spectra assumes that inhomogeneous strain broadening of peaks is not a major effect. Some proof for this assumption is presented later. With this assumption, an estimate of grain size can be made from the Scherrer relation for grain size broadening of diffraction peaks [109];

$$d = 0.9\lambda/B\cos\theta \quad (5.1)$$

where $\lambda=0.154$ nm is the wavelength of Cu-K α radiation, d is

the grain diameter, B is the full width at half maximum and θ is the Bragg angle. The results of such a calculation using the 002 peak are shown in Table 5.1. The grain size does not change dramatically as a function of substrate bias. The best conducting films (-90V, -115V) have a grain size of about 40 nm.

An annealing experiment was able to provide some insight concerning the extent of inhomogeneous strain broadening. A good quality ZnO conductor was annealed in air at 720 K for 3 hours. Figure 5.6 shows the 002 diffraction peak and film resistivity before and after annealing. The large increase in resistivity is believed to be due to the elimination of oxygen vacancy or Zn interstitial donor levels as stoichiometric composition is attained through oxygen diffusion. Significant strain relief has occurred in the annealed film, indicated by a shift in peak position closer to 34.47° . Gawlak and Aita [105] have observed similar strain relief in ZnO annealed at 600 K. Surprisingly, in spite of strain relief, my films show very little change in intensity or peak half-width at full maximum. It is unlikely that homogeneous strain relief would occur without some inhomogeneous strain relief (indicated by a reduction of peak width), therefore I conclude that the ZnO films do not possess significant inhomogeneous strain. Also, from a symmetry argument, it seems unlikely that a film composed of well aligned parallel crystallites should exhibit strain of different magnitudes in different crystallites.

Films for scanning electron microscope (SEM)

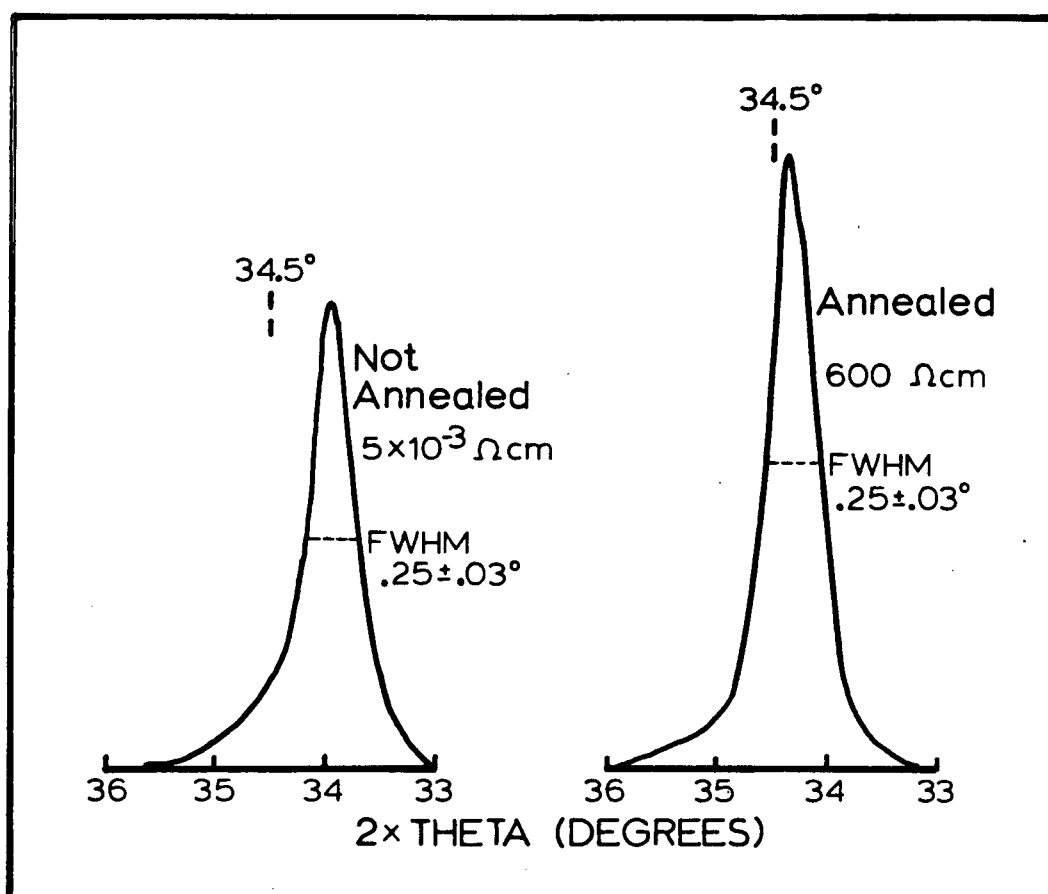


Figure 5.6

The 002 X-ray diffraction peak of a ZnO film before and after annealing at 720 K for 3 hours.

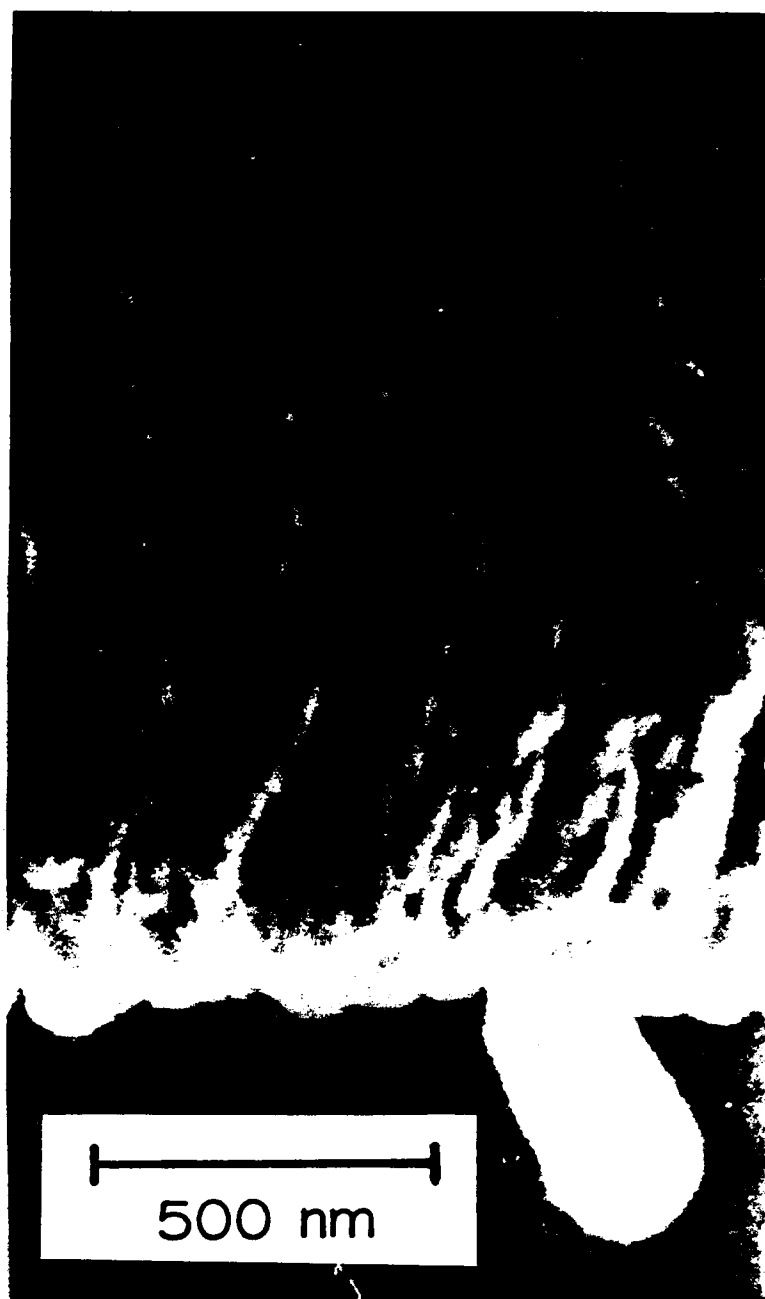


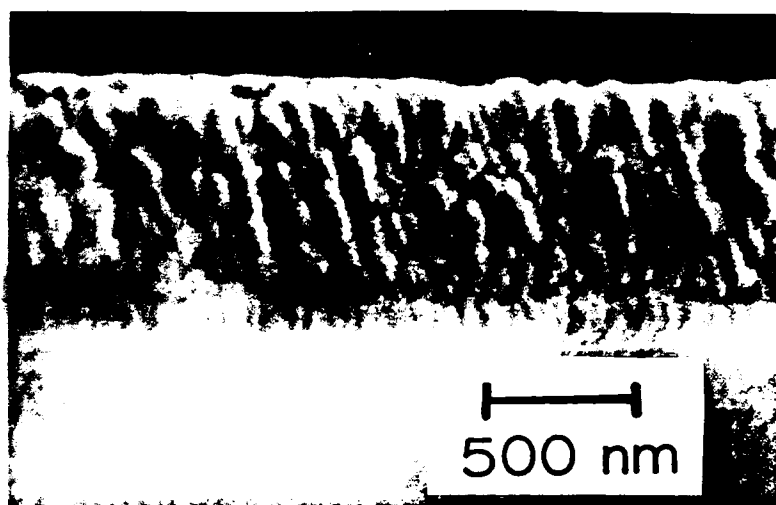
Figure 5.7

An SEM photomicrograph of a transparent, conducting, bias sputtered ZnO film. The film is viewed in cross section at an angle of 45° from the substrate normal.



Bias

-7 V



-100 V

500 nm

Figure 5.8

SEM photomicrographs comparing the surface roughness of ZnO films deposited with and without a substrate discharge.

investigation were sputtered on glass substrates. In order to view the films in cross section the substrates were cleaved. Etching techniques were not used to define grain boundaries. Figure 5.7 shows an SEM photograph of a ZnO film deposited at -100 V bias, viewed at an angle of about 45° from the substrate normal. As is common for vacuum deposited coatings at low temperatures, a roughly columnar microstructure is visible. One of the columns has been displaced by the cleaving process to a position parallel to the substrate surface. The column diameter of about 200 nm is compatible with (not smaller than) the grain size of 40 nm estimated from X-ray diffraction studies.

Figure 5.8 compares cross-sectional SEM photographs of ZnO films deposited with and without a substrate bias. The bias sputtered film exhibits a smoother surface. Such bias induced smoothing is believed to be due to a redistribution of sputtered material from evaporation and resputtering effects, as observed by Thornton for sputter deposited metal films [108].

5.3 ELECTRICAL PROPERTIES

To enable electrical transport studies, films were deposited in a Hall probe geometry by masking as shown in Figure 5.9. Films on quartz substrates were deposited simultaneously for the study of optical properties, allowing a correlation of transport and optical properties that will be addressed in section 5.4. After production of ZnO films in

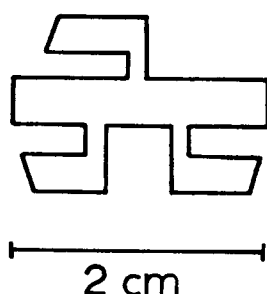


Figure 5.9

ZnO samples for characterization by Hall probe techniques were deposited in this geometry by utilizing a mask during deposition.

Table 5.2 Electrical properties of bias sputtered ZnO films.

Sample	Substrate Bias (V)	Resistivity ($10^{-3}\Omega\text{cm}$)	Hall Constant (cm^3/C)	Mobility (cm^2/Vs)	Carrier Density (10^{20}cm^{-3})
ZnO-1	-6	20	-.019	1.0	3.3
ZnO-2	-40	24	-.031	1.3	2.0
ZnO-3	-65	4.5	-.055	12	1.1
ZnO-4	-90	1.9	-.034	18	1.8
ZnO-5	-115	2.1	-.040	19	1.6
ZnO-6	-140	2.4	-.037	15	1.7

Table 5.3 Electrical properties of ZnO films produced by other groups.

Deposition Technique	Resistivity ($10^{-3}\Omega\text{cm}$)	Hall Constant (cm^3/C)	Mobility (cm^2/Vs)	Carrier Density (10^{20}cm^{-3})	Reference
rf sputter	7		13	0.7	112
reactive evap	2	-.07	45	0.8	14
rf sputter	7		8	1.1	15
rf sputter	1		20	3.0	16

the metallic target mode at various values of substrate bias, the Hall coefficient was measured at room temperature with the use of a 13 kG electromagnet. From the Hall coefficient, R , the carrier mobility μ and carrier density N were calculated using the relations;

$$\mu = R/\rho \quad (5.2)$$

$$N = 1/Re$$

where ρ is the film resistivity and e is the electronic charge. Table 5.2 summarizes the electrical characterization for bias sputtered ZnO films. Experimental errors in the measurements are about $\pm 20\%$.

All films were found to have large carrier densities near $2 \times 10^{20} \text{ cm}^{-3}$ and a calculation of degeneracy [110,111] gave a Fermi level E_F approximately 0.35 eV above the conduction band edge. Samples ZnO-1 and ZnO-2 are visually dark and have a Zn excess of 10 to 20 atomic percent. All other samples are transparent and expected to have a nearly stoichiometric composition. The distinguishing feature between dark and clear films is the low mobility of $1 \text{ cm}^2/\text{Vs}$ for the dark films.

Selected results of electrical transport properties at room temperature for high conductivity transparent ZnO deposited by other workers are shown in Table 5.3. It is seen that the carrier densities and mobilities in my films are similar to those produced by rf sputter deposition from a oxide target. However, only Caporaletti [112] has discussed scatter mechanisms for conduction electrons and no

investigators have studied black Zn excess oxide films.

Caporaletti has proposed a grain boundary limited mobility for ZnO films, but unfortunately had no data on film structure to indicate very small grain sizes. From the transport data of Table 5.2, I estimated the mean free path of conduction electrons in transparent films to be about 2 nm, using a relaxation time given by $\tau = m^* \mu / e$ for electron effective mass $m^* = 0.24m_0$. Since the grain boundary separation (determined from X-ray and SEM work of section 5.2) is at least 40 nm and thus much larger than the mean free path, I conclude that grain boundary scattering is not the dominant scattering process. Also, the order of magnitude change in the mobility of my films with increasing bias does not correlate with the nearly constant grain size shown in Table 5.1. It should be stressed that the electrical properties (Table 5.2) and X-ray diffraction spectra (Figure 5.4) are data taken from the same set of films.

Mansfield [113] has extended the standard work of Conwell and Weisskopf on ionized impurity scattering [114] to degenerate semiconductors and has derived the following expression for conductivity;

$$\sigma = \frac{3h^3 \epsilon^2 n}{16\pi^2 e^2 m^{*2} f(x)} \quad (5.3)$$

with $f(x) = \ln(1+x) - \frac{x}{1+x}$

and $x = (h^2 \epsilon / e^2 m^*) (3n/8\pi)^{1/3}$

where ϵ is the static dielectric constant (8.2 for ZnO), n is the density of ionized impurity centres, and all other symbols

have their normal meanings. If the electron density (from donor centres) in transparent conducting ZnO is equated to the ionized impurity concentration, this leads to a mobility $\mu=70 \text{ cm}^2/\text{Vs}$. Additional scattering contributions may come from defect or neutral impurity centres such as Ar or C impurities or from a small excess of unionized Zn. Using expressions for neutral impurity scattering developed by Erginsoy [114], a neutral Zn impurity density of 10^{19} cm^{-3} could limit carrier mobility to about $30 \text{ cm}^2/\text{Vs}$. Such a combination of ionized and neutral impurity scattering has been used to explain the transport properties of transparent, conducting ITO [116].

Until the precise structural nature of the large Zn excess in dark, low mobility ZnO is known, it is only possible to speculate on the identity of scatter centres. Similar metal excess in sputtered In_2O_3 and AlN films [127,131] was found to occur in the form of small inclusions or precipitates of metal. It is possible that the lower mobilities of ZnO-1 and ZnO-2 are due to Zn inclusion scatter centres and also to the higher impurity concentrations of Ar and C that occur in films deposited at low bias values.

5.4 OPTICAL PROPERTIES

Recently Greene [117] has pointed out the scarcity of detailed characterization of ZnO films, despite the large amount of literature available on ZnO. This section reports the results of the first detailed study of the optical

properties of transparent conducting ZnO films and black Zn excess films. Other workers have characterized optical properties by just the transmission spectrum in the visible and by the behaviour of the band edge with doping [16,112,118,119,120]. In addition, Morgan and Brodie [14] have reported an average film reflectivity for radiation from a 373 K blackbody. For both dark and transparent conducting ZnO films prepared at various values of the substrate bias, I have measured the refractive index and extinction coefficient for the wavelength range 0.35 to 2.5 μm , and the reflectivity at wavelengths 2.5 to 20 μm .

The same set of films, on quartz substrates, that were studied by X-ray diffraction (Figure 5.5) and Hall probe (Table 5.2) techniques were measured for transmission and reflection using the ultraviolet, visible and infrared spectrophotometers described in section 2.1. In addition, a highly resistive ($>10^4 \Omega\text{cm}$) stoichiometric ZnO film (labelled ZnO-7) was deposited in the oxide mode of target coverage with no substrate bias, and analyzed optically. Determination of optical constants was possible in the wavelength range 0.35 to 2.5 μm , where both transmission and reflection measurements were taken. Transmission measurements in the middle infrared (2.5 to 20 μm) were not possible due to the strong absorption of the quartz substrates.

In the weakly absorbing wavelength regions, the optical constants n and k were determined using a technique slightly modified from that of Manifacier et al. [121]. This technique

is illustrated in the transmission and reflection characteristics of sample ZnO-5 (deposited at -115 V bias) in Figure 5.10. Continuous curves were drawn connecting consecutive interference maxima and consecutive interference minima that enabled explicit calculation of n and k using the independently determined film thickness. In wavelength regions where films were strongly absorbing, standard equations for the transmission and reflection of a single thin film layer on quartz structure were solved for n and k using an iterative technique. Both of these types of calculation are described in detail in the Appendix, sections 7.1 and 7.2. Conducting film thicknesses were chosen to be about 800 nm, thick enough to exhibit a few orders of interference structure, yet thin enough to measure transmission in absorbing regions. The resistive film ZnO-7 was much thicker, 2.7 μm , so that interference structure would extend into the near infrared region (1 to 2.5 μm) where stoichiometric ZnO remains transparent.

Figure 5.11 shows the optical constants n and k that were calculated for samples ZnO-1 (-7V bias), ZnO-2 (-40V bias), ZnO-5 (-115V bias) and for the resistive sample ZnO-7. The electrical properties of the conducting samples were summarized previously in Table 5.2. The visual observation of a transition from dark to clear ZnO with increasing bias is confirmed by the decrease of k values in the visible wavelength region.

The absorption in sample ZnO-7 was too small to be

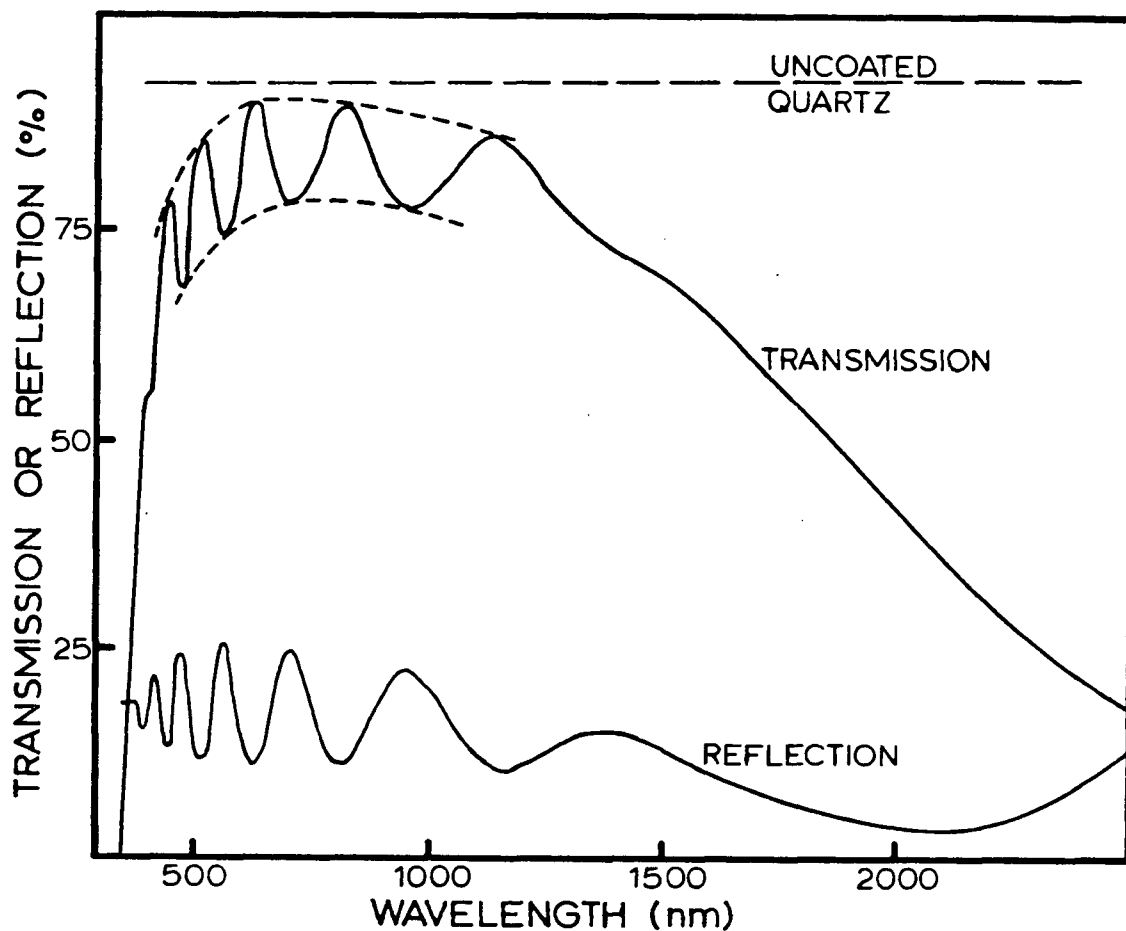


Figure 5.10

Transmission and reflection characteristics of sample ZnO-5 on a quartz substrate. Continuous curves (indicated by the dashed lines) were constructed connecting interference extrema to enable determination of the optical constants of the film.

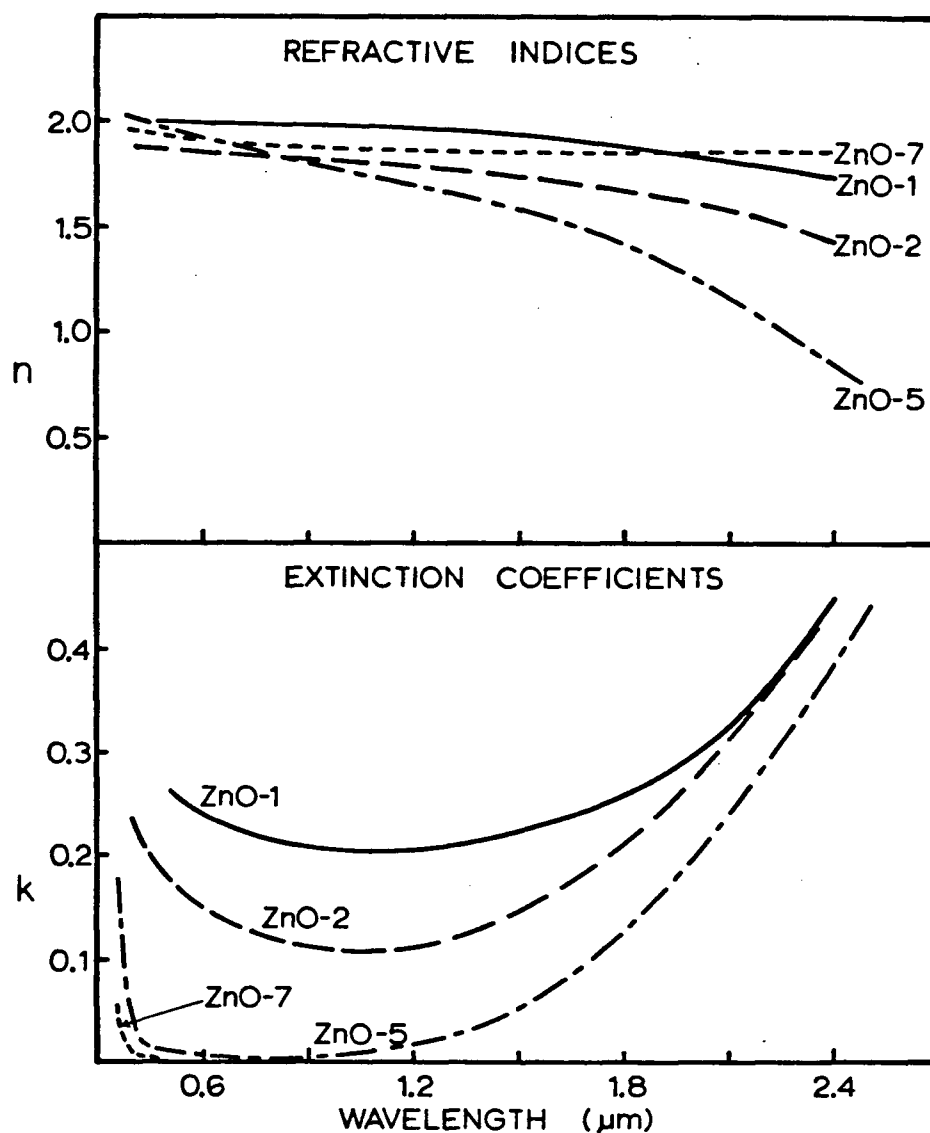


Figure 5.11

Optical constants of ZnO films. Samples ZnO-1, ZnO-2 and ZnO-5 were deposited at substrate bias values of -6, -40, and -115 V respectively. Sample ZnO-7 was deposited in the oxide target mode and is highly resistive. Experimental errors are 4% in n and 25% in k .

measured using my techniques, except for the few data points near the band edge. This sample had a constant refractive index in the visible of 1.86 ± 0.08 . Refractive index values for a ZnO single crystal are shown by Mollwo [122] to vary between 1.98 and 2.14 in the wavelength region 670 to 430 nm. It is often found that vacuum deposited films have lower refractive indices than their corresponding bulk materials, due in part to the lower density of defected or polycrystalline films [123].

Detailed studies of the band edge region (360 to 390 nm) were not made. Measurement of the strong absorption near the band edge would require very thin films (100 nm) to ensure measureable transmission. Inspection of the transmission spectra of clear films shows an optical bandgap of approximately 3.3 ± 0.1 eV. Precise measurements of the optical bandgap in conducting ZnO by other workers have given values between 3.2 and 3.5 eV [112,118]. These workers observed an increase of the optical bandgap with increasing carrier concentration, attributed to the Burstein-Moss band filling effect.

Figure 5.12 compares the infrared reflection spectra and resistivity for samples ZnO-1, ZnO-3 and ZnO-5. As expected, the best conducting film, ZnO-5, displays the highest reflectivity. The reflectivity structure seen in sample ZnO-1 is due to the properties of the quartz substrate.

As discussed in section 5.3, bias sputtered ZnO films can be classified into two general groups. Films at low bias

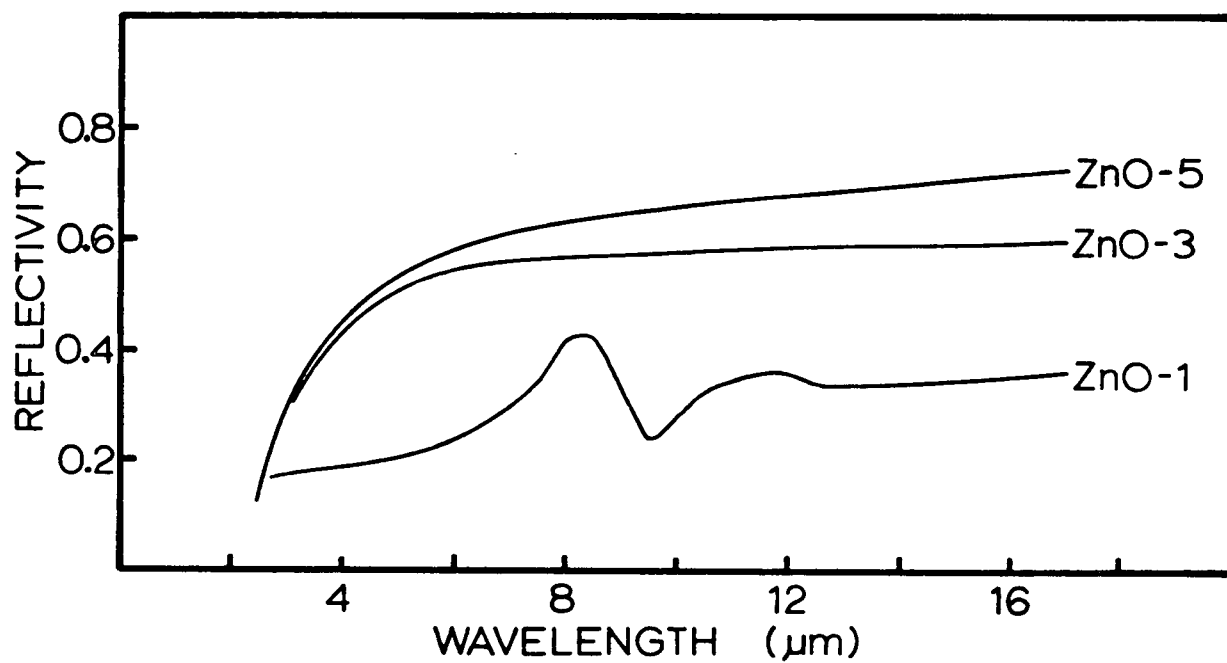


Figure 5.12

Infrared reflectivity characteristics of films ZnO-1, ZnO-3 and ZnO-5, deposited at substrate bias values of -6, -65 and -115 V respectively.

(ZnO-1 and ZnO-2) have a large Zn excess resulting in low electron mobilities, high resistivity and poor infrared reflectivity, and are strongly absorbing in the visible. The ZnO films deposited at high substrate bias (ZnO-3 to ZnO-6) are nearly stoichiometric, optically transparent, have high electron mobilities resulting in low resistivity and good infrared reflectivity. The transparent conducting ZnO films are of most interest in this thesis work. Their optical and electrical properties may be related using the free electron approximation.

The Drude theory of free electrons, introduced in section 1.3, has been used successfully to model the infrared reflection properties of the transparent conductors ITO [124], CTO [29], and SnO_2 [20]. This theory has not previously been applied to conducting ZnO. The measured electrical parameters of mobility μ and carrier density N in Table 5.2 have been used in equations 1.4 and 1.5 to generate the Drude prediction for optical constants and reflectivity. Figure 5.13 shows the experimental and predicted infrared reflectivity of sample ZnO-5, using the independently measured electrical parameters $\mu=19 \text{ cm}^2/\text{Vs}$ and $N=1.6 \times 10^{20} \text{ cm}^{-3}$. Instead of using the tabulated value of $\epsilon_\infty=3.73$ for bulk ZnO, I used $\epsilon_\infty=3.46$ calculated from measurement of the optical constants of the stoichiometric, resistive sample ZnO-7. The plasma wavelength was calculated as $\lambda_p=2.8 \text{ }\mu\text{m}$. The good fit to the experimental data shows that the free electron theory of Drude provides a model for conducting ZnO.

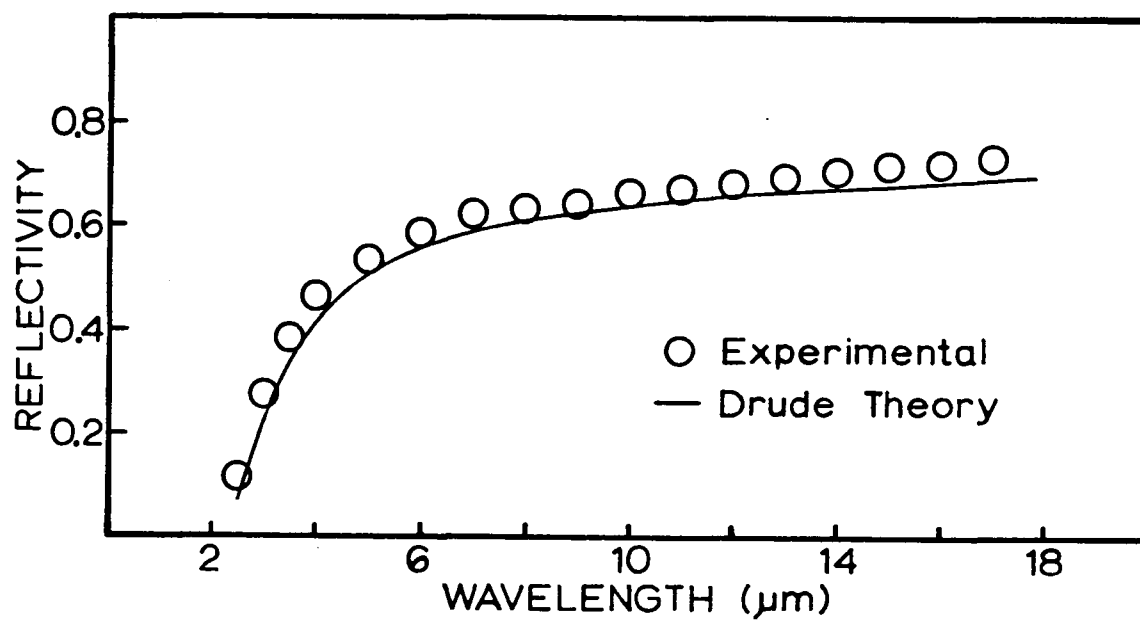


Figure 5.13

Comparison of the measured infrared reflectivity of sample ZnO-5 with the reflectivity predicted by the Drude free electron model. The measured electrical transport parameters $N=1.6 \times 10^{20} \text{ cm}^{-3}$ and $\mu=19 \text{ cm}^2/\text{Vs}$ were used in the Drude model.

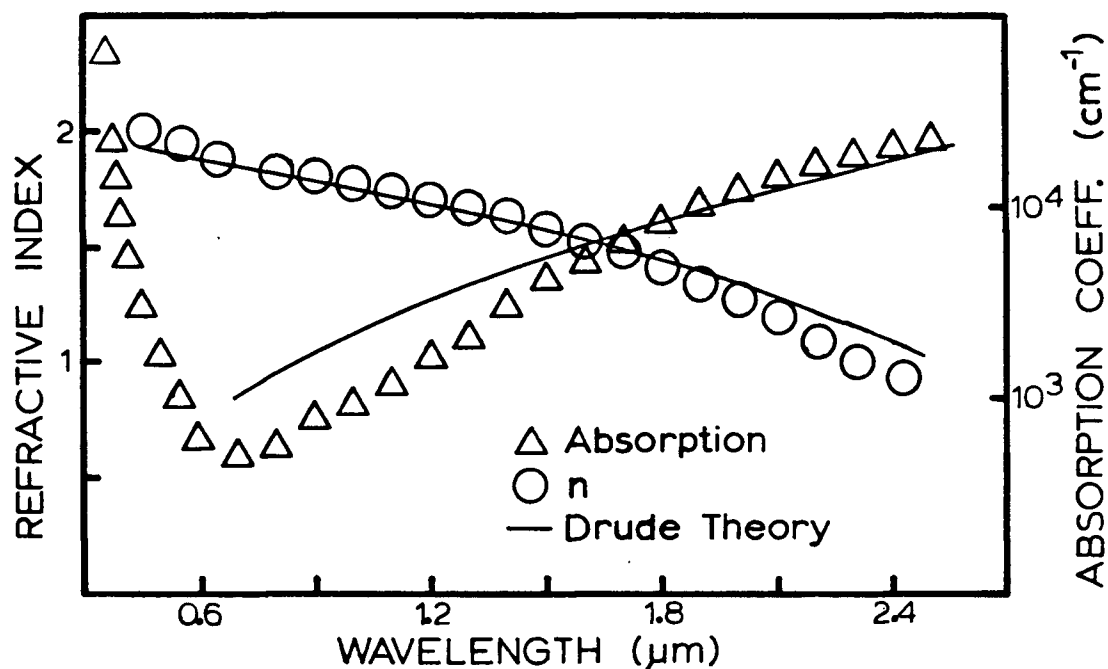


Figure 5.14

Comparison of the measured refractive index n and absorption coefficient α of sample ZnO-5 with the predictions of the Drude free electron model. The measured electrical transport parameters $N=1.6 \times 10^{20} \text{ cm}^{-3}$ and $\mu=19 \text{ cm}^2/\text{Vs}$ were used in the Drude model.

The Drude prediction was also extended into the visible wavelength region. Figure 5.14 shows the refractive index n and the absorption coefficient $\alpha=4\pi k/\lambda$ of sample ZnO-5. The values predicted from Drude theory display a rough fit to the data, the major discrepancy being a larger predicted absorption at small wavelengths ($600\text{nm}<\lambda<1500\text{nm}$). However, at these wavelengths, where $\lambda<\lambda_p$, the classical Drude theory fails. For high energy photons, the scattering process involved in absorption must be considered, and the value of the absorption coefficient becomes dependent on the type of scattering mechanism involved. For neutral impurity scattering, Dumke [125] has estimated that free electron theory should not be in error by more than 20% at photon energies up to $h\nu=8E_F$, or $\lambda=460\text{ nm}$. For ionized impurity scattering, Dumke predicts that the Drude theory will significantly overestimate the absorption at small wavelengths. Thus, for conducting ZnO films it is found that Drude theory approximates the behaviour of optical constants at wavelengths $\lambda>\lambda_p$, with discrepancies that are qualitatively predicted for scatter centres of neutral and ionized impurities.

The validity of the Drude model was tested for absorbing Zn excess films (ZnO-1 and ZnO-2), in spite of the greater uncertainty in film microstructure and conduction mechanisms. Figure 5.15 shows the free electron plasma properties predicted using $\mu=1.0\text{ cm}^2/\text{Vs}$ and $N=3.3\times 10^{20}\text{ cm}^{-3}$ for ZnO-1, compared with experimental optical constants and infrared

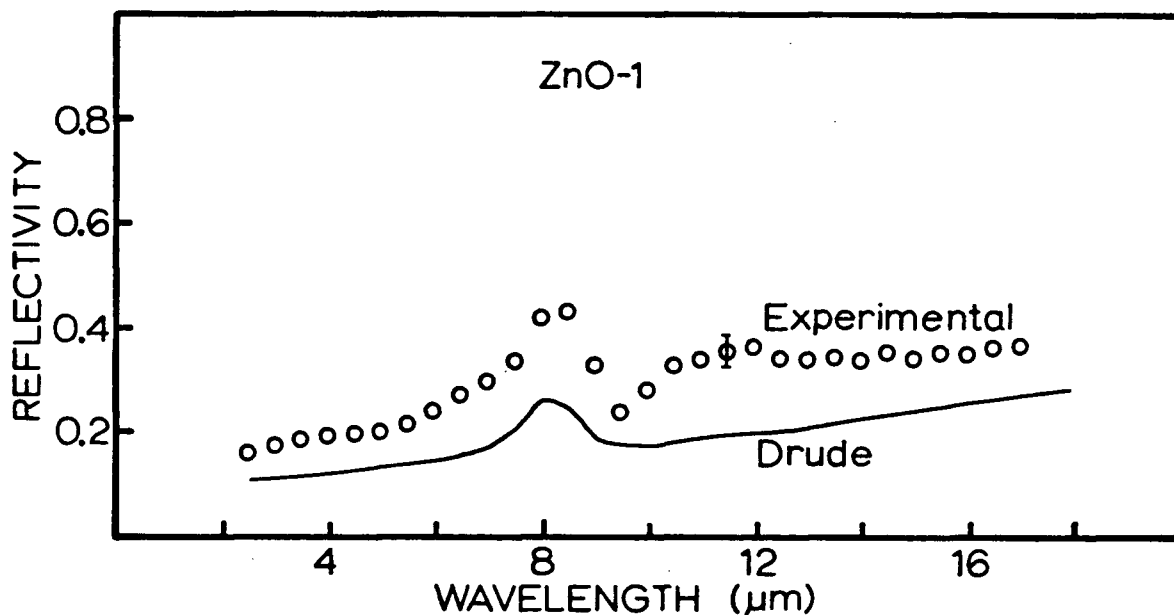
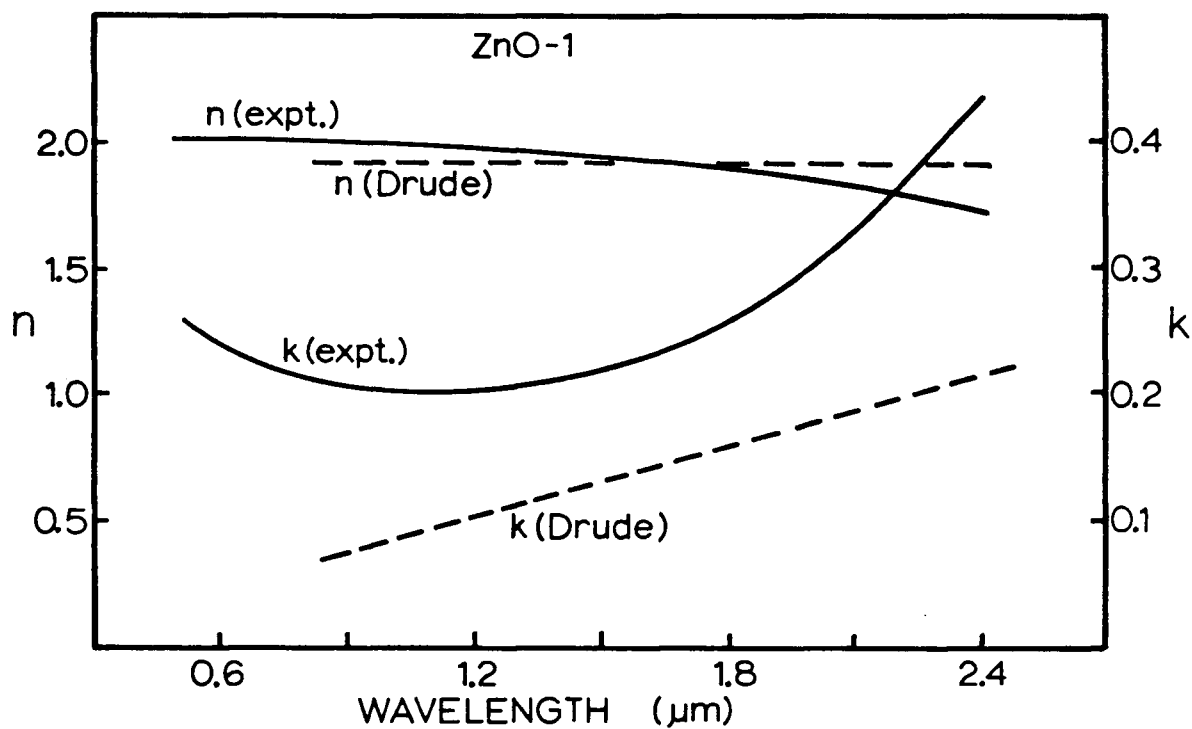


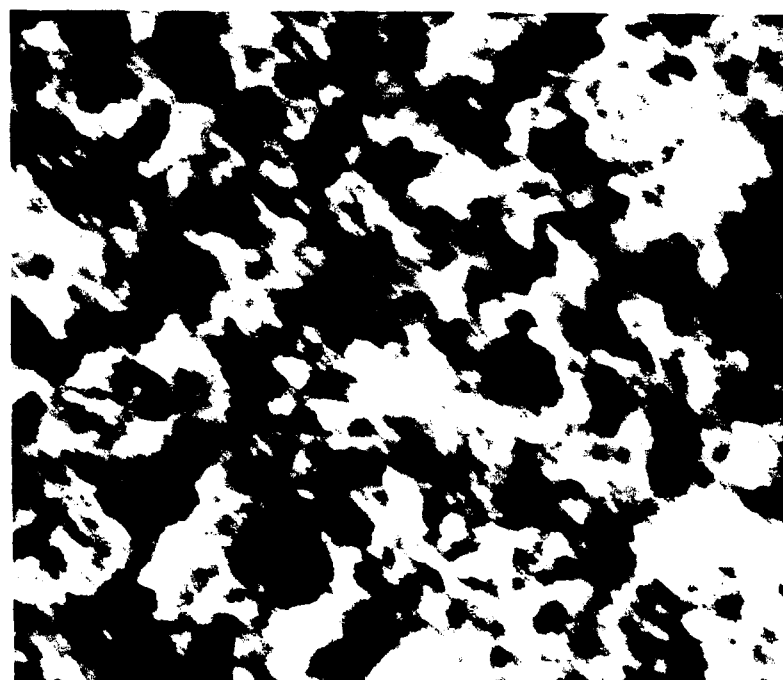
Figure 5.15

Comparison of the measured optical constants and infrared reflectivity of sample ZnO-1 with those calculated using the Drude free electron model. The measured electrical parameters $N=3.3 \times 10^{20} \text{ cm}^{-3}$ and $\mu=1.0 \text{ cm}^2/\text{Vs}$ were used in the Drude model.

reflectivity. Due to the lower infrared absorption of dark ZnO films, the reflectivity calculation had to account for the substrate reflectivity. This calculation is detailed in the Appendix, section 7.2. The Drude model is found to provide an estimate of the absorption coefficient within a factor of 2, and follows the infrared reflectivity trend, but at values lower than the experimental spectrum. It is not surprising that the Drude model fails since only the free electron contribution to the dielectric constant has been considered, and the contributions from possible precipitations or inclusions of excess zinc have been ignored.

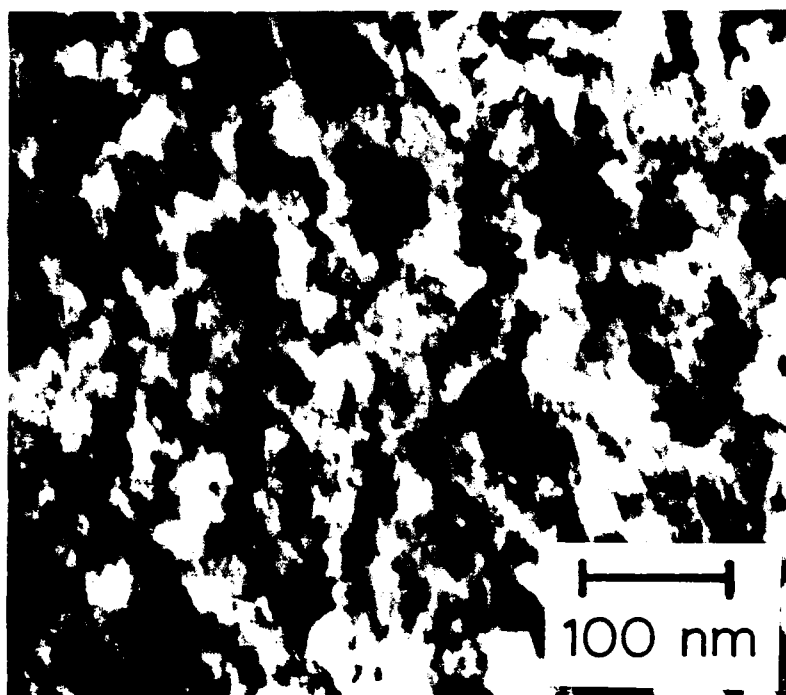
Attempts to define the nature of the Zn excess were made by bias sputtering 100 nm thick ZnO samples onto copper microgrids for transmission electron microscope (TEM) studies. Figure 5.16 compares TEM photographs of transparent conducting ZnO (bias -100V) and black ZnO (no substrate discharge). Within the TEM resolution of about 3 nm, no obvious difference is seen in the similar granular appearance of each film. The expected grain size of about 40 nm is comparable with the structures seen in these photographs. Other workers have reported TEM photographs of sub-stoichiometric In_2O_3 [127] and AlN [126] that are remarkably similar in appearance to ZnO. Also, it was observed that a large change in AlN composition was required before TEM photographs resolved a structure difference [126,130]. No conclusions concerning the existence of Zn precipitates may be reliably drawn from my TEM data.

In spite of the uncertainty in the black ZnO film



Bias

-7 V



-100 V

100 nm

Figure 5.16

TEM photomicrographs comparing ZnO films deposited with and without a substrate discharge.

microstructure, an illustrative calculation is performed to show how the dielectric constants may be modified by Zn inclusions. For this calculation, I assume that islands of pure Zn are randomly embedded in a matrix of ZnO. The simplest approach to the description of the dielectric properties of such a mixture was given by Maxwell-Garnett [128]. For spherical particles of dielectric constant ϵ_m , dispersed in a medium of dielectric constant ϵ , the Clausius-Mossotti relation [134] for the polarizability of small spheres is used to find an average or effective dielectric constant $\bar{\epsilon}$;

$$\bar{\epsilon} = \epsilon + \frac{3f\epsilon(\epsilon_m - \epsilon)}{\epsilon_m + 2\epsilon - f(\epsilon_m - \epsilon)} \quad (5.4)$$

where f is the volume fraction of embedded particles. An expression for $\bar{\epsilon}$ detailing real and imaginary components of the various dielectric constants has been given by Affinito [131]. This calculation assumes that the metallic islands are small with respect to the wavelength of light. Although there are many other similar formalisms used to predict the optical properties of heterogeneous materials, the Maxwell-Garnett theory has proved to be more successful in treating the optical properties of thin agglomerated metal films and of noble metal particles imbedded in glasses [128,129,130].

The dielectric constant of the ZnO matrix, ϵ , was calculated for ZnO-1 from the Drude theory using $\mu=1.0 \text{ cm}^2/\text{Vs}$ and $N=3.3 \times 10^{20} \text{ cm}^{-3}$. Tabulated values of the dielectric constant for bulk Zn [132,133] were used to describe the properties of Zn islands, ϵ_m . The volume fraction, $f=0.20$ for

ZnO-1, was estimated from the RBS measurement of film stoichiometry and the known densities of Zn and ZnO. The Maxwell-Garnett calculation was performed for sample ZnO-1 in the infrared, since it is only in this wavelength region that the Drude theory for the optical properties of the matrix is expected to be valid. Figure 5.17 compares the measured infrared reflectivity of sample ZnO-1 with the Drude approximation and with the Maxwell-Garnett prediction.

Including the effects of excess Zn through the use of a simple effective medium theory is shown to improve the fit to the experimental results. This exercise has certainly not proven that black ZnO is composed of spherical particles embedded in a ZnO matrix, but indicates the need for the consideration of the effects of film microstructure (presently unknown) in tandem with the effects of conduction electrons in order to adequately describe optical constants.

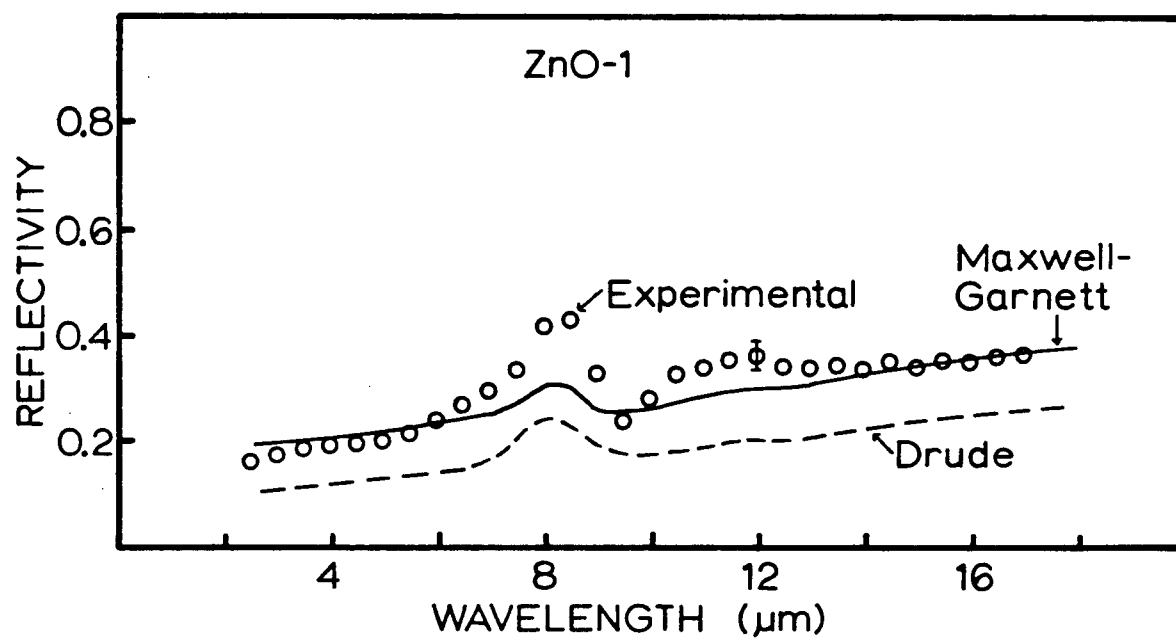


Figure 5.17

Comparison of the measured infrared reflectivity of sample ZnO-1 with reflectivities calculated using 1) the Drude free electron model and 2) the Maxwell-Garnett theory for a 0.20 volume fraction of Zn inclusions.

CHAPTER SIX: SUMMARY

This concluding chapter serves to summarize the new contributions of my work obtained from the first detailed study of reactively bias sputtered conducting ZnO films.

The reactive gas baffle at the target was shown to enhance the oxidation of Zn sputtered from a metal target surface by increasing the partial pressure of oxygen near the substrate and by decreasing the Zn flux to the substrate. When used in conjunction with an rf discharge at the substrate, the baffle provided the further benefit of eliminating interaction between the dc target and rf substrate discharges.

As suggested by other workers but not previously proven, the rf discharge at the substrate was shown to increase the relative oxygen content of the film. One mechanism of oxidation was found to be activation and ion plating of oxygen species in the discharge. Other mechanisms active in promoting complete oxidation were preferential resputtering and preferential evaporation of excess zinc. These re-emission processes were unexpected due to the low temperature substrates (380 K) and the low power substrate discharge (-100 V, 20 mW/cm²). However, resputter and evaporation rates were greatly enhanced above that expected for bulk Zn or bulk ZnO, attributed to the weak bonding of surface adatoms during film growth.

Nearly stoichiometric ZnO deposited at high oxygen partial pressures was resistant to re-emission due to rapid oxidation and the strength of the Zn-O bond. Zn excess films

deposited at low oxygen partial pressures showed significant material re-emission (70%) due to slow oxidation and the high vapour pressure and weak bonding of Zn adatom aggregates.

The enhanced re-emission phenomena found for ZnO might only be observed for a few other compounds, for instance Cd_2SnO_4 , where the metallic constituents exhibit high vapour pressures and weak bonding. In contrast, Ti was chosen as a representative low vapour pressure metal. Reactively sputtered titanium oxide films showed no material re-emission for substrate biases up to -175 V. However, the oxygen ion plating mechanism was still presumed to be active, reducing the optical absorption attributed to Ti metal excess.

ZnO was established as a new candidate material for heat mirror manufacture. Films sputtered onto polyester sheet at a deposition rate of 75 nm/min were found to have a transmission to solar energy of 75% and an 85% reflection of 300 K blackbody radiation. $\text{In}_2\text{O}_3:\text{Sn}$ films of resistivity $9 \times 10^{-4} \Omega\text{cm}$ were also deposited onto polyester sheet, and at the time of publication this was the lowest recorded resistivity for ITO on plastic substrates.

Optical, electrical and structural properties were characterized for ZnO films as a function of substrate bias from -7 V to -120 V. These properties are itemized below.

1. The relative oxygen content of the films increased with bias from approximately ZnO_8 to ZnO. This increase is due to the oxidation mechanisms just discussed.
2. Films deposited at high bias had a much smoother surface

than the low bias films, attributed to a redistribution of deposited material by resputtering and evaporation processes.

3. The variation with bias of polycrystal orientation, size and stress was attributed to the competing effects of crystal disruption by ion bombardment and crystal improvement due to a more stoichiometric composition. The best conducting films had a grain size of about 40 nm and a lattice strain of 0.8%.

4. Films deposited at high bias had electron mobilities near $20 \text{ cm}^2/\text{Vs}$. It was proposed that this mobility is limited by ionized and neutral impurity scattering. Low bias films had lower mobilities near $1 \text{ cm}^2/\text{Vs}$, attributed to scatter centres created by the Zn excess.

5. Since the electron density was approximately constant with bias ($2 \times 10^{20} \text{ cm}^{-3}$), the film resistivity was minimized to $2 \times 10^{-3} \text{ } \Omega\text{cm}$ at high bias.

6. Optical constants of the films were deduced for the wavelength range 0.4 to $2.5 \text{ } \mu\text{m}$ and reflectivity from 2.5 to $20 \text{ } \mu\text{m}$ wavelength. The best conducting films were visually transparent and had a measured infrared reflectivity in good agreement with that calculated using the Drude theory of free electrons. The low mobility films were visually dark. Free electron absorption only partly accounted for this dark appearance.

CHAPTER SEVEN: APPENDIX

7.1 OPTICAL CONSTANTS OF TRANSPARENT FILMS

To deduce the optical constants of transparent ZnO films on quartz substrates, I used a modification of the technique proposed by Manifacier et al. [121]. Figure 7.1 shows a ZnO film of complex refractive index $n-ik$ on a thick quartz substrate of refractive index n_1 surrounded by air of refractive index $n_0=1$. Nominal thicknesses for the quartz and ZnO layers are given. For regions of negligible absorption, this thin film structure exhibits interference effects in both reflection and transmission spectra as seen previously in Figure 5.10. The exact expressions for transmitted and reflected light intensity from a 3 interface structure are cumbersome and, in general, difficult to solve.

The method of Manifacier assumes a perfectly transparent substrate and weak absorption in the film such that $k^2 < (n-n_0)^2$ and $k^2 < (n-n_1)^2$. Continuous functions $T_1(\lambda)$ and $T_2(\lambda)$ were constructed which are the envelopes of the transmission interference maxima and the transmission interference minima, respectively (Figure 5.10). The expressions for the optical constants of the film then reduce to;

$$n^2 = N + (N^2 - n_0^2 n_1^2)^{1/2} \quad (7.1)$$

where $N = (1/2)(n_0^2 + n_1^2) + 2n_0 n_1 (T_1 - T_2) / T_1 T_2$

$$\text{and} \quad \exp(-4\pi kt/\lambda) = \frac{C_1 [1 - (T_1/T_2)^{1/2}]}{C_2 [1 + (T_1/T_2)^{1/2}]} \quad (7.2)$$

where $C_1 = (n+n_0)(n_1+n)$, $C_2 = (n-n_0)(n_1-n)$ and t is the film thickness. Unfortunately the transmission, $T(\lambda)$, used by

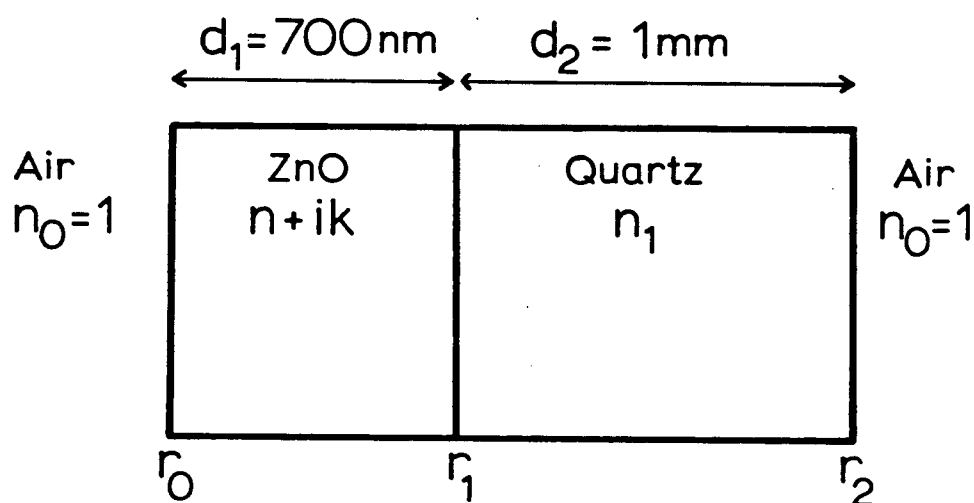


Figure 7.1

A schematic of a ZnO film on a quartz substrate labelling the thickness d , refractive indices n and interface reflectivities r .

Manifacier in this calibration was the light transmission into the substrate, not into the air as would be measured experimentally. To generate the transmission values $T(\lambda)$ required for these formulae from the experimental values $T_{\text{exp}}(\lambda)$, I used a first order correction accounting for reflection at the quartz-air interface;

$$T(\lambda) = T_{\text{exp}}(\lambda)/[1-r(\lambda)] \quad (7.3)$$

where $r(\lambda)$ is the reflection of a single quartz-air interface, and has a nominal value of 0.035.

This modified technique was used to calculate n and k for the transparent, conducting samples ZnO-3, ZnO-4, ZnO-5, and ZnO-6 in the wavelength range 400 to 1400 nm and for the stoichiometric sample ZnO-7 in the range 400 to 2500 nm. Extinction coefficients were not greater than $k=0.25$, consistent with the assumption of weak absorption, $k^2 < 0.25$. The refractive indices n were determined to an accuracy of about 4% and k values to an accuracy of about 25%, due to experimental errors of 1.5% in transmission spectra and 7% in film thickness.

7.2 OPTICAL CONSTANTS OF ABSORBING FILMS

To determine the optical constants of absorbing films showing no interference effects, I developed an iterative procedure based on the standard formulae for total transmission and reflection of light intensity in the ZnO/quartz structure. Using the notation of Figure 7.1, these formulae are written as;

$$T = \exp(-4\pi kd_1/\lambda)(1-r_0)(1-r_1)(1-r_2) \quad (7.4)$$

$$R = r_0 + \exp(-8\pi kd_1/\lambda)[(1-r_0)^2 r_1 + (1-r_0)^2 (1-r_1)^2 r_2] \quad (7.5)$$

where higher order terms involving multiple reflections have been neglected. This approximation introduces a maximum absolute error of 0.003 in T or R . The interface reflectivities r are obtained from the appropriate refractive indices. For example;

$$r_1 = \frac{(n-n_1)^2 + k^2}{(n+n_1)^2 + k^2} \quad (7.6)$$

The values used for the refractive index of quartz, n_1 , were those tabulated by Malitson [135]. The iterative procedure used to find n and k is as follows:

1. R , T , and d were measured.
2. λ and r_2 were known.
3. Initialize $r_0=R$ and $r_1=0$.
4. Evaluate k using equation (7.4).
5. Evaluate r_0 using equation (7.5).
6. Evaluate n from r_0 .
7. Calculate r_1 using the new n and k values.
8. Repeat steps 4 through 7.

Convergence to three figure agreement of successive n and k values was obtained after about 5 iterations.

This technique was used to deduce n and k for samples ZnO-1 and ZnO-2 at all wavelength values, and for samples ZnO-3, ZnO-4, ZnO-5 and ZnO-6 at wavelengths $\lambda < 400$ nm and $\lambda > 1400$ nm. Uncertainties in the final values of n and k due to experimental errors are similar to those of the previous calculation; $\Delta n/n=4\%$ and $\Delta k/k=30\%$. The optical constants calculated in both the absorbing and transparent approximations at the boundary between the 'absorbing' and 'transparent' regions were found to agree within the

calculational uncertainty for all films.

Equation (7.5) was also used to calculate the theoretical infrared reflectivity of the low mobility (ZnO-1 and ZnO-2) ZnO films on quartz. Values of n and k for ZnO were determined from the Drude theory and values of the optical constants of quartz in the infrared are tabulated by Phillip [136]. Thus the infrared reflectivity calculated from these films shows anomalous structure (Figure 5.17) due to strong absorption bands in the quartz substrate. High mobility ZnO films are strongly absorbing in the infrared and did not require consideration of substrate reflectivity.

REFERENCES

1. R. McMahon, Solnote 3, Solar Energy Society of Canada Inc., (1980).
2. J. Fan and F. Bachner, Appl. Opt. 15, 1012 (1976).
3. L. Holland and S. Siddall, Br. J. Appl. Phys. 9, 359 (1958).
4. H. Glaser, Glass Tech. 21, 254 (1980).
5. C.M. Lampert, Sol. Energy Mat. 6, 1 (1981).
6. J.L. Vossen, Physics of Thin Films 9, 1 (1977).
7. K. Chopra, S. Major and D. Pandya, Thin Solid Films 102, 1 (1983).
8. Z.M. Jarzebski, Phys. Stat. Sol. (a) 71, 13 (1982).
9. F. Seitz, Modern Theory of Solids, (McGraw-Hill, New York, 1940) p.638.
10. The Southwall Corporation, Palo Alto, California, U.S.A.
11. M. Brett, R. McMahon, J. Affinito and R. Parsons, J. Vac. Sci. Technol. A1, 352 (1983).
12. M.J. Brett and R.R. Parsons, Sol. State Comm. 54, 603 (1985).
13. M.J. Brett and R.R. Parsons, Can. J. Phys., in press.
14. J. Morgan and D. Brodie, Can. J. Phys. 60, 1387 (1982).
15. J.B. Webb and D.F. Williams, Appl. Phys. Lett. 39, 640 (1981).
16. T. Minami, H. Nanto and S. Takata, Appl. Phys. Lett. 41, 958 (1982).
17. L. Ryabova, V. Salun and I. Serbinov, Thin Solid Films 92, 327 (1982).
18. R. Groth and E. Kauer, Phill. Tech. Rev. 26, 105 (1965).
19. Price quoted by Canada Metal Inc., Vancouver, Canada.
20. F. Simonis, M. van der Leij and C. Hoogendoorn, Sol. Energy Mat. 1, 221 (1979).
21. F. Smith and S. Lyu, J. Electrochem. Soc. 128, 1083

- (1981).
22. N. Miyata, K. Miyake and S. Nao, Thin Solid Films 58, 385 (1979).
 23. S. Maniv, C. Miner and W.D. Westwood, J. Vac. Sci. Technol. 18, 195 (1981).
 24. D. Hall, J. Electrochem. Soc. 124, 804 (1977).
 25. G. Haacke, Appl. Phys. Lett. 28, 622 (1976).
 26. I. Hamberg, A. Hjortsberg and C. Granqvist, Appl. Phys. Lett. 40, 362 (1982).
 27. J. Machet, J. Guille, P. Saulnier and S. Robert, Thin Solid Films 80, 149 (1981).
 28. H. Kostlin, R. Jost and W. Lems, Phys. Stat. Sol. (a) 29, 87 (1975).
 29. R.P. Howson, M. Ridge and C. Bishop, Thin Solid Films 80, 137 (1981).
 30. D. Fraser and H. Cook, J. Electrochem. Soc. 119, 1368 (1972).
 31. M. Buchanan, J.B. Webb and D.F. Williams, Thin Solid Films 80, 373 (1981).
 32. Y. Hsu and S. Ghandhi, J. Electrochem. Soc. 127, 1592 (1980).
 33. J. Manificier, J. Fillard and J. Bind, Thin Solid Films 77, 67 (1981).
 34. P. Petrou, R. Singh and D.E. Brodie, Appl. Phys. Lett. 35, 930 (1979).
 35. J. Aranovich, A. Ortiz and R. Bube, J. Vac. Sci. Technol. 16, 994 (1979).
 36. G. Heiland, E. Mollwo and F. Stockmann, Solid State Physics 8, 191 (1959).
 37. F. Kroger, The Chemistry of Imperfect Crystals, (Interscience, New York, 1973) p.744.
 38. T. Wada, S. Kikuta, M. Kiba, K. Kiyozumi, T. Shimojo and M. Kakehi, J. Crystal Growth 59, 363 (1982).
 39. D. Block, A. Herve and R. Cox, Phys. Rev. B25, 6049 (1982).

40. C. Gonzalez, D. Block, R.T. Cox and A. Herve, J. Crystal Growth 59, 357 (1982).
41. W.S. Baer, Phys. Rev. 154, 785 (1967).
42. E. Paradis and A. Shuskus, Thin Solid Films 38, 131 (1976).
43. S.B. Krupanidhi and M. Sayer, J. Appl. Phys. 56, 3308 (1984).
44. M. Royer, J. Holmen, W. Wurm, O. Aadland and M. Glenn, Sensors and Actuators 4, 357 (1983).
45. A.P. Roth and D.F. Williams, J. Electrochem. Soc. 128, 2684 (1981).
46. J.C. Manificier, Thin Solid Films 90, 297 (1982).
47. J.L. Vossen and W. Kern, Thin Film Processes, (Academic Press, New York, 1978).
48. R.F. Bunshah, Deposition Technologies for Films and Coatings, (Noyes Publications, Park Ridge, 1982).
49. J. Rostworowski and R. Parsons, J. Vac. Sci. Technol., in press.
50. R. Howson, J. Avaritsiotis, M. Ridge and C. Bishop, Thin Solid Films 58, 379 (1979).
51. R. Howson and M. Ridge, Thin Solid Films 77, 119 (1981).
52. R. Brown, in Handbook of Thin Film Technology, edited by L. Maissel and R. Glang, (McGraw-Hill, New York, 1970) p.6-39.
53. S. Schiller, U. Heisig, K. Steinfelder, J. Strumpfel and W. Sieber, Vak. Tech. 30, 3 (1981).
54. A.J. Stirling and W.D. Westwood, Thin Solid Films 7, 1 (1971).
55. J. Heller, Thin Solid Films 17, 163 (1973).
56. J. Affinito and R.R. Parsons, J. Vac. Sci. Technol. A2, 1275 (1984).
57. S. Maniv, C.J. Miner and W.D. Westwood, J. Vac. Sci. Technol. A1, 1370 (1983).
58. G. Kominiak, J. Vac. Sci. Technol. 12, 689 (1975).
59. Brian Chapman, Glow Discharge Processes, (John Wiley, New

York, 1980) chapter 5.

60. C. Horwitz, J. Vac. Sci. Technol. A1, 60 (1983).
61. K. Kohler, J.W. Coburn, D.E. Horne, E. Kay and J.H. Heller, J. Appl. Phys. 57, 59 (1984).
62. J. Thornton and A. Penfold, in Thin Film Processes, edited by J. Vossen and W. Kern (Academic Press, New York, 1978) p.99.
63. J.W. Coburn and E. Kay, J. Appl. Phys. 43, 4965 (1972).
64. Y. Okamoto and H. Tamagawa, J. Phys. Soc. Japan 29, 187 (1970).
65. W. Davis and T. Vanderslice, Phys. Rev. 131, 219 (1963).
66. H.R. Koenig and L.I. Maissel, IBM J. Res. Dev. 14, 168 (1970).
67. J. Machet, P. Saulnier, J. Ezquera and J. Guille, Vacuum 33, 279 (1983).
68. D.M. Mattox, Electrochem. Tech. 2, 295 (1964).
69. D.M. Mattox, in Proc. Conf. Ion Plating and Allied Techniques, p.1 (1979).
70. D.M. Mattox, in Deposition Technologies for Films and Coatings, edited by R.F. Bunshah (Noyes Publications, Park Ridge, 1982) p.244.
71. J.E. Greene and S.A. Barnett, J. Vac. Sci. Technol. 21, 285 (1982).
72. J.A. Thornton, paper presented at the International Conference on Metallurgical Coatings, San Diego, California, 1983.
73. J.P. Coad and R.A. Dugdale, in Proc. Conf. Ion Plating and Allied Techniques, p.186 (1979).
74. H. Winters, D. Raimondi and D. Horne, J. Appl. Phys. 40, 2996 (1969).
75. J. Cuomo and R. Gambino, J. Vac. Sci. Technol. 12, 79 (1975).
76. D. Dove, R. Gambino, J. Cuomo and R. Kobliska, J. Vac. Sci. Technol. 13, 965 (1976).
77. R. Howson, K. Suzuki, C. Bishop and M. Ridge, Vacuum 34, 291 (1984).

78. Y. Igasaki and H. Mitsuhashi, *Thin Solid Films* 70, 17 (1980).
79. J. Poitevin, G. Lemperiere and J. Tardy, *Thin Solid Films* 97, 69 (1982).
80. H.F. Winters and E. Kay, *J. Appl. Phys.* 43, 794 (1972).
81. P. Mazzoldi and G. Della Mea, *Thin Solid Films* 77, 181 (1981).
82. J. Sundgren, B. Johansson and S. Karlsson, *Thin Solid Films* 80, 77 (1981).
83. J.A. Thornton and J.L. Lamb, *Thin Solid Films* 119, 87 (1984).
84. S. Dushman, Scientific Foundations of Vacuum Technique, (John Wiley, New York, 1982) p.693.
85. B. Chapman, Glow Discharge Processes, (John Wiley, New York, 1980) appendix 5.
86. D.G. Teer, *J. Phys.* D9, L187 (1976).
87. M. Hecq, A. Hecq and M. Fontignies, *Thin Solid Films* 115, L45 (1984).
88. G. Carter and J. Colligon, Ion Bombardment of Solids, (Heinemann, London, 1968) chapter 6.
89. S. Barnett and J. Greene, *Surf. Sci.* 128, 401 (1983).
90. Y. Shintani, K. Nakanishi, T. Takawaki and O. Tada, *Jap. J. Appl. Phys.* 14, 1875 (1975).
91. J. Hanak and J. Pellicane, *J. Vac. Sci. Technol.* 13, 406 (1976).
92. J. Cuomo, R. Gambino, J. Harper and J. Kuptsis, *J. Vac. Sci. Technol.* 15, 281 (1978).
93. R. Jones, C. Standley and L. Maissel, *J. Appl. Phys.* 38, 4656 (1967).
94. V. Nwoko and H. Uhlig, *J. Electrochem. Soc.* 112, 1181 (1965).
95. S. Kelemen, Y. Goldstein and B. Abeles, *Surf. Sci.* 116, 488 (1982).
96. J.F. O'Hanlon, A User's Guide to Vacuum Technology, (John Wiley, New York, 1980) p.371.

97. L. Maissel, R. Jones and C. Standley, IBM J. Res. Dev. 14, 176 (1970).
98. H. Winters and E. Kay, J. Appl. Phys. 38, 3928 (1967).
99. J.F. O'Hanlon, A User's Guide to Vacuum Technology, (John Wiley, New York, 1980) p.207.
100. American Society for Testing and Materials, Document ASTM-E838, 1981.
101. F.S. Hickernell, Proceedings of the 1979 Ultrasonics Symposium, (IEEE, New York, 1979) p. 932.
102. T. Minami, H. Nanto, S. Shooji and S. Takata, Thin Solid Films 111, 167 (1984).
103. J. Affinito, N. Fortier and R.R. Parsons, J. Vac. Sci. Technol. A2, 316 (1984).
104. S. Maniv, W. Westwood and E. Columbini, J. Vac. Sci. Technol. 20, 162 (1982).
105. C. Gawlak and C. Aita, J. Vac. Sci. Technol. A1, 415 (1983).
106. F. Sarott, Z. Iqbal and S. Veprek, Sol. State Comm. 42, 465 (1982).
107. D.M. Mattox and G. Kominiak, J. Vac. Sci. Technol. 9, 528 (1972).
108. J.A. Thornton, Thin Solid Films 40, 335 (1977).
109. B. Cullity, Elements of X-ray Diffraction, (Addison-Wesley, London, 1959) p.99.
110. C. Kittel, Introduction to Solid State Physics, (John Wiley and Sons, New York, 1976) p.162.
111. J. Pankove and E. Annavedder, J. Appl. Phys. 36, 3948 (1965).
112. O. Caporaletti, Sol. Energy Mat. 7, 65 (1982).
113. R. Mansfield, Proc. Phys. Soc. B69, 76 (1956).
114. E. Conwell and V. Weisskopf, Phys. Rev. 77, 388 (1949).
115. C. Erginsoy, Phys. Rev. 79, 1013 (1950).
116. P. Grosse, F. Schmitte, G. Frank and H. Kostlin, Thin Solid Films 90, 309 (1982).

117. J. Greene, CRC Crit. Rev. Solid State Mater. Sci. 11, Suppl. 3, 189 (1984).
118. A. Roth, J. Webb and D. Williams, Phys. Rev. B25, 7836 (1982).
119. K. Ito and T. Nakazawa, Jap. J. Appl. Phys. 22, L245 (1983).
120. P.S. Nayar, J. Elect. Mater. 11, 967 (1982).
121. J. Manificier, J. Gasiot and J. Fillard, J. Phys. E9, 1002 (1976).
122. E. Mollwo, Z. Agnew. Physik 6, 257 (1954).
123. W. Pliskin and S. Zanin, in Handbook of Thin Film Technology, edited by L. Maissel and R. Glang, (McGraw-Hill, New York, 1970) p.11-43.
124. J. Fan and F. Bachner, J. Electrochem. Soc. 123, 1719 (1975).
125. W. Dumke, Phys. Rev. 124, 1813 (1961).
126. Normand Fortier, unpublished data (1985).
127. A.F. Hebard and S. Nakahara, Appl. Phys. Lett. 41, 1130 (1982).
128. J. Maxwell-Garnett, Phil. Trans. R. Soc. Lond. 205, 237 (1906).
129. S. Norrman, T. Andersson and C. Granqvist, Phys. Rev. B18, 674 (1978).
130. R.H. Doremus, J. Appl. Phys. 37, 2775 (1966).
131. J. Affinito, PhD Thesis, University of British Columbia, 1984.
132. A. Lenham and D. Treherne, Proc. Phys. Soc. 83, 1059 (1964).
133. A. Lenham and D. Treherne, J. Opt. Soc. Am. 56, 752 (1966).
134. J.D. Jackson, Classical Electrodynamics, (John Wiley, New York, 1975) p.155.
135. I.H. Malitson, J. Opt. Soc. Am. 55, 1205 (1965).
136. H.R. Phillip, J. Appl. Phys. 50, 1053 (1979).

137. M.P. Seah, Thin Solid Films 81, 279 (1981).
138. D.K. Murti, Appl. Surf. Sci. 11, 308 (1982).
139. K. Kim, W. Baitinger, J. Amy and N. Winograd, J. Electr. Spectr. Rel. Phenom. 5, 351 (1974).
140. F.A. Grant, Rev. Mod. Phys. 31, 646 (1959).